UC San Diego
UC San Diego Electronic Theses and Dissertations

Title
Structural Deterioration of Human Articular Cartilage and Subchondral Plate

Permalink
https://escholarship.org/uc/item/4z52s2dc

Author
Chang, Neil

Publication Date
2016

Peer reviewed|Thesis/dissertation

UNIVERSITY OF CALIFORNIA, SAN DIEGO

STRUCTURAL DETERIORATION OF HUMAN ARTICULAR CARTILAGE AND SUBCHONDRAL PLATE

A dissertation submitted in partial satisfaction of the

requirements for the degree Doctor of Philosophy

in

Bioengineering

by

Neil Chang

Committee in charge:

        Professor Robert L. Sah, Chair
        Professor William D. Bugbee
        Professor Maripat P. Corr
        Professor Koichi Masuda
        Professor Shyni Varghese

2016

The dissertation of Neil Chang is approved, and it is acceptable in quality and form for publication on microfilm and electronically:

_____

_____

_____

_____

_____

Chair

University of California, San Diego

2016

DEDICATION

In 1990, a graduate student in computer science at the University of California, Los Angeles, vying to be the first in his family to earn a doctorate, took a leave of absence so that he could spend more time to raise his two-year-old son. He never returned to complete his degree. Even though he may not express it very often, his son is deeply grateful for the personal sacrifices that his father and mother made to ensure that he had a loving childhood, great educational opportunities, and unconditional support. This year, his son is, in a sense, completing what he started.

This dissertation is dedicated to my father, Paul, and my mother, Betty.

EPIGRAPH

"If you are a poet, you will see clearly that there is a

cloud floating in this sheet of paper."

Thich Nhat Hanh

TABLE OF CONTENTS

LIST OF FIGURES AND TABLES

ACKNOWLEDGMENTS

I would like to thank everyone who made this work possible through their invaluable mentorship, advice, and guidance during my time as a doctoral student. My sincere thanks to my advisor, Dr. Robert Sah, for his guidance and motivation, for never giving up on me on the bumps on the road, and for teaching me the art of adhering to the scientific method. In the past six plus years, he transformed me from an anxious young student to an eager investigator with a meticulous eye for logical consistency. No matter what I do next in life, I have no doubt the guidance he has given me will help me excel.

I also would like to thank the members of my dissertation committee, Dr. William Bugbee, Dr. Maripat Corr, Dr. Koichi Masuda, and Dr. Shyni Varghese for their support and guidance.

Besides my dissertation advisors, there are many I need to thank for providing me, each in their own way, with the support necessary to obtain a Ph.D. My thanks to the staff of the Bioengineering Department for helping me through the administrative process. I especially would like to thank Jan Lenington for her continual efforts in making the entire process go smoothly and for having an answer for every question I gave her.

To the entire Cartilage Tissue Engineering Lab, I am especially grateful for not only the guidance and advice, but for always keeping the lab a friendly and warm environment. I can say with certainty that the "lab culture" among the co-workers here is top notch; I have found here over the years everyone from elders who never hesitate to take time from their busy day to help me with a problem or question, to close and lifelong friends.

To the staff members in the lab, I thank you for your advice, support and solid presence. Van Wong was always supportive and never reluctant to help me with any

in and out of our lab over the years and help to keep it well-stocked, and running smoothly.

Finally, thanks to family and friends outside the lab whose unwavering support has kept me going. My particular thanks to my graduate classmate, Kadir Tung, for never failing to provide me with a willing ear on any topic. Thanks to my parents, Paul and Betty Chang, and brother, Andy Chang, for providing everything that has culminated in the opportunity to pursue a Ph.D., and for the continual love and support.

VITA

2009	B.S., Bioengineering University of California, Berkeley
2010-2016	Graduate Student Researcher Cartilage Tissue Engineering Laboratory University of California, San Diego
2014	M.S., Bioengineering University of California, San Diego
2016	Ph.D., Bioengineering University of California, San Diego

Journal Articles

Mologne TS, Cory E, Hansen BC, Naso AN, Chang N, Murphy, MM, Provencher, MT, Bugbee WD, Sah RL. Osteochondral allograft transplant to the medial femoral condyle using a medial or lateral femoral condyle allograft: Is there a difference in graft sources? Am J Sports Med 42:2205-13, 2014.

Novitskaya E, Zin C, Chang N, Cory E, Chen P, D'Lima D, Sah RL, McKittrick J: Creep of trabecular bone from the human proximal tibia. Journal of the Mechanical Behavior of Biomedical Materials 40:219-27, 2013.

Kwon KY, Wang E, Chang N, Lee SW. Characterization of the Dominant Molecular Step Orientations on Hydroxyapatite (100) Surfaces. Langmuir. 25:7205-7208, 2009.

Kwon KY, Wang E, Chung A, Chang N, Lee SW. Effect of Salinity on Hydroxyapatite Dissolution Studied by Atomic Force Microscopy. Journal of Physical Chemistry C. 113:3369-3372, 2009.

Kwon KY, Wang E, Chung A, Chang N, Saiz E, Choe UJ, Koobatian M, Lee SW. Defect Induced Asymmetric Pit Formation on Hydroxyapatite. Langmuir. 24:11063-11066, 2008.

Selected Abstracts

Chang N, Wong VW, Hsu FH, Moran KL, Bugbee WD, Lotz MK, Sah RL: Altered Density and 3-D Morphology of Human Subchondral Plate Vascular Channels with Cartilage Degeneration. Trans Int Cart Repair Soc 8541, 2016.

Chang N, Wong VW, Bugbee WD, Schumacher BL, Sah RL: Chondrocyte fate inferred from 3-D bioimage informatics of cell organization in human articular cartilage. Trans Orthop Res Soc 41:477, 2016.

Mantripragada VP, Boehm C, Dikina A, Chang N, Wong VW, Alsberg E, Sah RL, Midura R, Muschler G: Epidemiology of chondrogenic progenitors in tissues around the human knee. Trans Orthop Res Soc 41:601, 2016.

Chang, N, Wong VW, Cory E, Hsu FH, Sah RL. 3-D organization of cells and matrix in human articular cartilage. Trans Orthop Res Soc 40:321, 2015.

Chang, N, Cory, E, Chen, AC, Lotz, MK, Sah, RL. Multi-scale delineation of articular cartilage deterioration in aging and osteoarthritis. Trans Orthop Res Soc 40:365, 2015.

Chang N, Murphy MM, Cory E, Chen AC, Bugbee WD, Sah RL. Loss of cartilage matrix fixed charge density in failed osteochondral allografts at localized defect and host-donor interface sites. Trans Int Cart Repair Soc 7100, 2015.

Boehm C, Dikina A, Mantripragada VP, Chang N, Wong VW, Alsberg E, Sah RL, Midura R, Muschler G: Optimizing various sources of chondrogenic connective tissue progenitors by 2D and 3D culturing for cartilage tissue regeneration. Trans Int Cart Repair Soc P200, 2015.

Chang N, Maheshwari AJ, Chen AC, Cory E, Inoue N, Masuda K, Bugbee WD, Sah RL: Multiscale structural variation of the subchondral plate with osteochondral surface deterioration. Trans Orthop Res Soc. 39:155, 2014.

Cory E, Hansen BC, Naso AN, Chang N, Murphy MM, Provencher MT, Bugbee WD, Mologne TS, Sah RL: Lateral femoral condyle allografts provide an acceptable articular contour when implanted into medial femoral condyle recipient sites. Trans Orthop Res Soc 39:85, 2014.

Chang N, Cory E, Pallante AL, Chan EF, Lotz MK, Bugbee WD, Sah RL: Distinctive features of the subchondral bone plate. Trans Orthop Res Soc 38:1424, 2013.

Chang N, Cory E, Chen AC, Raub CB, Chan EF, Urbina AM, Otsuki S, Hasegawa A, Lotz MK, Sah RL: Spatial variation in indentation properties of human femoral articular cartilage. Trans Orthop Res Soc 36:2137, 2011.

ABSTRACT OF THE DISSERTATION

STRUCTURAL DETERIORATION OF

HUMAN ARTICULAR CARTILAGE AND SUBCHONDRAL PLATE

by

Neil Chang

Doctor of Philosophy in Bioengineering

University of California, San Diego, 2016

Professor Robert L. Sah, Chair

The articular cartilage and underlying subchondral plate, comprised of calcified cartilage and a continuous plate of subchondral bone, form the osteochondral unit which bears and transmits the load as well as maintains low hydraulic conductivity and permeability. Age-related degeneration transitions to osteoarthritis (OA) a disease that results in degeneration of articular cartilage and abnormality of the

subchondral plate. The mechanism of this transition is not well known, and likely involves interplay between both the bone and the cartilage. This dissertation aims to delineate the biological and structural changes that occur in the osteochondral interface with age-related degeneration and disease, to help gain a better understanding of the pathogenesis.

3-D morphometric analyses of the subchondral plate in microCT indicated that the tidemark was disrupted and roughened in the early stage of degeneration. Investigating the subchondral plate in histology and with Digital Volumetric Imaging revealed that the disruptions were often caused by penetrating vascular channels that are involved in bone remodeling, which become larger and more abnormal in morphology in early degeneration stages. The penetration and disruption of the tidemark was found to occur in an earlier stage than large changes in the chondrocyte organization and fissuring of the articular cartilage matrix, known hallmarks of OA. Because the disrupted interface can potentially compromise the subchondral plate's ability to act as a barrier to water and solutes, there is the potential of a mechanism where remodeling of the subchondral plate leads to more catabolism and fluid depressurization in the cartilage.

These studies provide new technical developments in the ability to analyze three-dimensional datasets computationally, and reduce them to morphometric parameters, allowing a multiscale assessment of the tissue depending on the region of focus and size of targeted objects. They provide quantitative confirmation of known histological hallmarks of degeneration and OA in both the cartilage and subchondral plate. Additionally, they provide novel 3-D information about the structure of the human subchondral plate in degeneration and OA, which has been mostly limited to studies of normal tissue in the past.

CHAPTER 1:

INTRODUCTION

1.1   General Introduction to the Dissertation

The deterioration and eventual erosion of the load-bearing and lubricated cartilage of the articulating joints is a known consequence of aging and eventual progression to disease. Recent advancements in the study of osteoarthritis have made clear that this progression is not just a mechanical function of physically wearing down the tissue, but involves biological and biochemical changes, and includes the whole synovial joint, not just the cartilage. In particular, the interface of the articular cartilage with the subchondral bone is altered in distinct and discretely different ways in the run-up to and early stages of deterioration of the cartilage. It is speculated that the biological remodeling here results in abnormality and degeneration for the interfacing deep zone of the articular cartilage, just as homeostatic changes in the synovial fluid and tissue can affect the superficial zone. To investigate this remodeling and its potential implications, it is necessary to use a multiscale analysis that not only examines the structural evolution of the tissues and layers and its effect on biological and biomechanical function, but also the smaller vasculature and cells that mediate the changes.

The overall motivation of this dissertation was to further delineate the biological and structural changes that occur in the osteochondral interface with age-related

degeneration and disease, and contribute to the understanding of its role in disease pathogenesis. The objectives of the studies in this dissertation were: (1) develop 3-D data acquisition and image processing techniques to accurately and automatically assess the interface structure, (2) use these techniques to compare tissue samples at different grades of degeneration, both within a single anatomical site (Chapter 2) and across a spatiotemporally graded continuum of tissue (Chapter 3), (3) assess the correspondence of this 3-D data with biological structures using high-resolution and contrast imaging techniques (Chapter 4 (2-D) and Chapter 5 (3-D). Finally, (4) the 3-D image processing and reduction principles developed here are also used to assess the structural informatics of the articular cartilage in detail, for parallel discussion with the osteochondral interface changes (Chapter 6).

Chapter 1 begins with an introduction to the osteoarthritis disease, the current clinical understanding, and the motivation to fully understand its pathogenesis. This is followed with a discussion of the structure, composition and function of the parts of the normal osteochondral unit in detail: the articular cartilage, calcified cartilage, and subchondral bone plate, and the interfaces between each layer. Strategies for visualizing these structures in 2-D and 3-D are discussed, with the goal being the understanding the role each layer plays as the unit undergoes degeneration. Finally, a description of the changes in both articular cartilage and subchondral plate at multiple scales, from the tissue to the cell, and potential mechanisms for these changes, are presented.

Chapter 2, which is currently being prepared for submission to *Bone*, continues the introduction of the subchondral plate layer and component structures in detail, with a discussion of the known information from past literature. This is followed by a description of the methods for automated image processing and reduction of 3-D subchondral plate data obtained with microcomputed tomography, that serve as the foundation for subsequent studies. This method is used on a standard subunit of the

osteochondral unit containing the subchondral plate, from samples of grades normal to partial thickness erosion, to give a novel, 3-D structural description of the alterations in the subchondral plate in these grades.

Chapter 3, currently being prepared for submission to the *Osteoarthritis and Cartilage*, uses the method in Chapter 2 to assess tissue regions that represent a spatiotemporal continuum of erosion. Human osteoarthritic tissue samples were chosen to have a relatively normal tissue region on one end, and an eroded region immediately posterior. This was to gain a degree of understanding of the temporal changes that occur as cartilage deterioration progresses in human tissue, where obtaining tissue at different time points is usually infeasible. In this model, the more normal, less weight bearing tissue is representative of an early time point when cartilage has begun to fibrillate but is not eroded, while the other end of the same sample contains a full thickness lesion and represents late-stage osteoarthritis. This, along with biochemical data about the proteoglycan content of the cartilage from contrasted microCT, presents a view on how the structure of the osteochondral unit is compromised on a large spatiotemporal scale relatable to the whole joint.

Chapter 4, currently being prepared for submission to *Cartilage*, uses 10X magnification, Safranin-O Fast Green stained 2-D histology to investigate the biological role of the pores and interfaces that were quantified in the first two studies. Here, the pores were identified to be largely comprised of both inactive and active vascular channels, and a standard 2-D region was assessed with digital stitching to quantify the linear density of these channels. The degree to which these channels occurred in their different forms and disrupted the interface, by grade from normal to partial thickness to full thickness erosion, was assessed here.

Chapter 5, which is currently being prepared for submission to the *Journal of Bone and Joint Surgery*, uses a 3-D sectioning-and-imaging method called Digital

Volumetric Imaging to investigate the morphology of these vascular channels in great detail in 3-D. The morphological characteristics of the channels were characterized and described based around their occurrences in normal and partial thickness eroded-cartilage tissue. Here, the potential for the aberrant channels, found in this and the previous chapter, to alter the biomechanical barrier function of the subchondral plate and articular cartilage, was discussed.

Finally, Chapter 6, which is currently being prepared for submission to *PLoS One*, uses the principles developed for image processing the subchondral plate in 3-D described previously to assess the articular cartilage for bioimage informatics of cell and matrix organization. Particularly, the changes in chondrocyte and chondron clustering and local matrix hypocellularity were quantified in cartilage tissue from normal to partial thickness to cartilage taken adjacent to a region of full thickness erosion. The cartilage was assessed zonally, both in the deep zone that interfaces with the subchondral plate to tie into possible downstream consequences of the biomechanical alterations purported in previous chapters, but also in the superficial zone to assess effect of organization on cartilage erosion. Here, the greatest changes were found in the superficial zone at higher grades in clustering of the cells and regions of local hypocellularity. The potential for a deep zone link, biochemically and organizationally, between the large changes found in the superficial zone and the altered barrier function in the subchondral plate is discussed.

Chapter 7 summarizes the major findings of the studies and implications for research of age-related degeneration, osteoarthritis, and contribution to the understanding of the role of the subchondral plate.

1.2 Osteoarthritis

Osteoarthritis (OA) is the most common joint disease, afflicting an estimated 27 million people in the United States as of the end of the last decade [1]. It has an estimated economic burden in the United States of more than 80 billion per year [2]. The key sign of OA is radiographic evidence of cartilage erosion, or large regions of full thickness cartilage loss, as well as cartilage roughening, and diminished intrinsic fluorescence of the tissue when viewed by arthroscopy. The disease is usually diagnosed following radiographic or arthroscopic investigation when the patient presents the symptoms of joint pain, locking or swelling. The clinical definition of OA, as defined by the Kellgren-Lawrence system, is the presence of both radiographic joint space narrowing and osteophytes [3]. The American College of Rheumatism defines it as a joint having pain and at least three of the following: individual is greater than 50 years old, morning stiffness for longer than 30 minutes, crepitus of motion, bony tenderness, bony enlargement, or synovium that is cool to the touch [4].

When OA will onset in a particular individual is not well understood, although the main risk factors are known to be advanced age and obesity. Most effective strategies on treating the disease are centered on preventing further cartilage loss, as the cartilage cannot regenerate itself. Other treatment strategies address the symptoms, but not the loss of cartilage itself, such as analgesics for pain, or anti-inflammatory medication. Once the disease progresses to a certain point, partial or total knee arthroplasty, or replacement of the joint with a metal prostheses, is necessary to regain joint function.

Although the primary sign of OA is loss of cartilage and associated joint space narrowing, it is a disease of the entire synovial joint (**Fig. 1.1**) [5]. The synovial capsule, comprised of a fat pad and surrounding synovial tissue, becomes inflamed, and

the synovial fluid accumulates cartilage degradation products. The meniscus tears and has diminished biochemical content. The cartilage fibrillates and is biochemically compromised with diminished proteoglycan content. There are chondro-osteophytes forming through endochondral ossification at the joint margin. Finally, there is vascular invasion and later thickening of the subchondral bone plate and calcified cartilage, the mineralized layers on which the cartilage is mounted. The focus of this dissertation is on the interaction of the subchondral bone plate and calcified cartilage with the articular cartilage in the progression of age-related degeneration of the tissue, and the transition to and pathogenesis of osteoarthritis in humans.
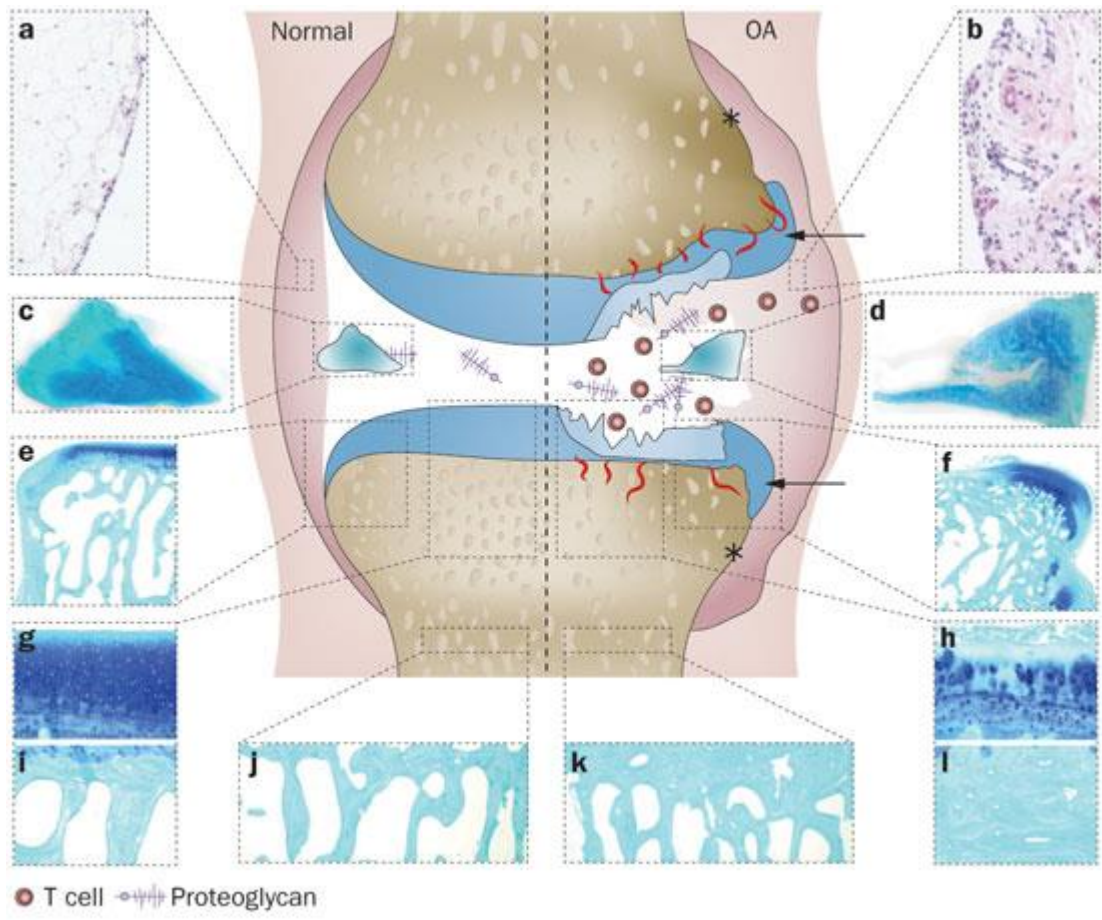
Figure 1.1: Osteoarthritis of the Knee. Osteoarthritis is a global disease of the joint, affecting the (a,b) synovium, (c,d) meniscus, (e,f) joint margin, (g,h) articular cartilage, (i,l) subchondral plate and (j,k) trabecular bone. From [5].

1.3 Structure, Composition and Function of the Normal Articular Cartilage, Subchondral Plate and Interfaces

1.3.1 Osteochondral Unit

In the normal adult synovial articulating joint, the uncalcified articular cartilage is attached to underlying TB by a subchondral plate (ScP) composed of two tissue layers, calcified cartilage (CC), ~100 μm thick, and "corticalized" subchondral bone plate (ScBP), ~300 μm thick (**Fig. 1.2**) [6]. The ScBP and CC vary between anatomical sites and individuals, in both the thickness of each structure and the morphology of their boundaries, the tidemark (AC-CC boundary), and the cement line (CC-ScBP boundary) [6-8]. The combined unit of articular cartilage and subchondral bone, from the surface to the beginning of the TB, will be defined as the osteochondral unit. Together, this unit works together to bear the load of the articulating joint, with the low friction, lubricated cartilage surface allowing articulation, the subchondral bone providing a harder physical structure to withstand compressive stresses, and the CC and ScBP transferring the load between the cartilage and bone.

1.3.2 Articular Cartilage: Chondrocytes and Matrix

The articular cartilage is a soft tissue layer comprised of two primary components: the cells or chondrocytes, and the matrix. In development and homeostasis, the chondrocytes secrete and maintain the matrix, whose composition (proteoglycans, Type II collagen) and biomechanical properties both allow it to protect the underlying subchondral bone from damage, as well as serve as a low friction surface that can glide past the apposing joint during articulation [9]. For study of the articular cartilage in this dissertation, the focus will be on the organization and density of these

chondrocytes, whose abnormalities can affect the biology of the surrounding matrix and other layers.

Chondrocytes are the mature cells of cartilage, which modulate the articular matrix via secretion of cytokines which affect its homeostatic balance. They occupy lacunae which conform to the general shape of the cell, and are a round shaped cell, occasionally bearing cilium. The cells each contain a rounded nuclei [10].

A chondron is a unit of several chondrocytes along with a pocket of matrix containing these cells that is distinct from the surrounding matrix, or the pericellular matrix [11]. In the pericellular matrix, the component collagen fibrils are thinner than in the surrounding, and are parallel to the surfaces of the chondrocytes [12]. Multiple chondrons in direct proximity are called clusters, which are rarely seen in normal tissue [13]. The chondrons are arranged in specific orientations based on the distance from the surface: horizontally or parallel to the plane of the surface in what is called the superficial zone (0-20% of full thickness from the surface), obliquely in the middle zone (20-40%), and vertically in the deep zone (60-100%).

1.3.3 Subchondral Plate

The subchondral plate is the combined layer of calcified cartilage and a continuous layer of bone called the subchondral bone plate. It has two primary functions: distribute stresses from overlying articular cartilage to subchondral bone [14], and as a low permeability barrier between articular cartilage and subchondral bone to modulate fluid and solute communication [15, 16]. The two component layers of the subchondral plate will each be described individually, followed by a discussion of the microstructural components, specifically the biological entities involved in its remodeling.

1.3.3.1 Calcified Cartilage

The zone of calcified cartilage is a mineralized layer of articular cartilage which provides attachment of the uncalcified cartilage to bone [6]. Like the uncalcified cartilage, the calcified cartilage contains chondrocytes in aligned lacunae or chondrons, with these chondrocytes being hypertrophic, and contains collagen fibrils which are usually aligned vertically and cross the tidemark. The mineralization of the calcified layer is from calcium hydroxypatite, like in the inorganic bone matrix. The calcified cartilage is about 6-8% of the full thickness of the articular cartilage layer [16-18]. In addition to providing a structural connection for the hyaline cartilage to the remainder of the mineralized tissue, the CC may also serve as a transitional layer of intermediate stiffness, based on the observation that it is an order of magnitude less stiff than subchondral bone [19].

1.3.3.2 Subchondral Bone Plate

The subchondral bone plate is a layer of corticalized bone, with varying thicknesses ranging from 0.1-3.0 mm depending on anatomical location [20-22], found distal to the zone of calcified cartilage. For this dissertation, the term subchondral *bone* plate will always refer to the corticalized bone layer only, with no inclusion of the immediately underlying cancellous bone or the calcified cartilage. Like all bone, it is comprised of a matrix that is 30-40% organic, mostly Type I collagen, and 60-70% mineral salts such as hydroxapatite. The matrix is arranged in a series of sheets, also called lamellae, which in the plate mostly run tangential to the calcified cartilage [23].

The mechanical function of the subchondral bone plate is to provide support for the overlying articular cartilage [24]. The mechanical function of the subchondral bone is to provide support for the overlying articular cartilage [24]. The subchondral bone absorbs most of the force transmitted by diarthrodial joints, while the articular cartilage

functions primarily as a bearing. The continuous surface of the subchondral bone plate transmits and distributes forces from the articulating surface to the structurally discontinuous trabecular bone [25-27].

1.3.3.3 Subchondral Plate Microstructural Components

The microstructure of the CC and ScBP reflects constant remodeling and turnover [26, 28], mediated by biological entities (**Table 1.1**, **Fig. 1.3**). Long bones are pervaded by numerous vascular foramina which penetrate the bone surface, and carry the vascular supply through to and from the bones with arteries and veins. Once within the bone, the arteries are distinct from most other vasculature in the body in that they contain a single endothelial layer surrounded by a thin layer of supportive connective tissue [29]. At the microstructural level, these arteries eventually branch off into both a mesh of marrow sinusoids and endosteal canals leading to capillaries in the ScBP [28].

The capillary and surrounding bone are also called vascular channels, which are important as substrate and supply for the bone remodeling [8, 28]. Vascular channels are 30-70 μm diameter fingerlike branches that extend from larger marrow spaces, and consist of one or more central capillaries surrounded circumferentially by lamellar bone. The channels have a bony cap, which may either be closed off to the calcified cartilage or open, in which case fenestrations in the endothelial cell lining may contact with the calcified cartilage [28]. In active remodeling, invading vascular channels support resorption pits or basic multicellular units, which are the primary unit of bone remodeling [30, 31].

Vascular channels comprise a sizeable portion of the "subchondral pores", defined by Burr and Clark as the many pores or small voids which are present in the ScP [20, 28]. Pores which are not vascular channels, such as microcracks, may still be involved in remodeling by supporting localized sites of active remodeling bone cells on

marrow surfaces [6, 32-34]. Subchondral pore density and penetration can potentially affect the permeability of both fluid and solutes to the surrounding tissues.

The subchondral plate also contains cells characteristic of all human bone which are indicators of the remodeling activity. When there is an active remodeling basic multicellular unit, or resorption pit, the front of the pit will contain osteoclasts, large multi-nucleated cells that resorb the old bone, followed by a vascular channel, and trailing osteoblasts that synthesize new osteoid matrix [30]. As the trailing osteoblasts are isolated and embedded in matrix during this process, they become inactive bone cells or osteocytes, which are the most common cell found in mature bone. Although inactive, these cells are interconnected through a series of small fluid-permeable channels called the lacunar-cannalicular network, and may still play a role in transducing mechanical stresses to biological activity.

1.3.4 Interfaces of the Osteochondral Unit

1.3.4.1 Tidemark

The tidemark is the gently undulating boundary between the uncalcified articular cartilage and calcified cartilage [6, 7]. It can be clearly distinguished as the mineralization front at the end of the deep zone of the articular cartilage, with a metachromatic line in most staining techniques of the tissue. In normal tissue, there is usually only one tidemark present for the entire osteochondral interface of an anatomical region. It is normally a continuous surface: there are collagen fibrils that cross it and run between the uncalcified and calcified cartilage, possibly helping to mount the former on the latter, but these do not interfere with the stain continuity of the line and surface [28].

The tidemark has been speculated to be a leftover artifact of the end of the endochondral ossification front during development. During this process, the hypertrophic chondrocytes in the bone precursor tissue are gradually encapsulated by mineralized extracellular matrix, and then undergo apoptosis [35, 36]. The resulting apoptotic bodies settle at the final calcification front, with the remains of larger, stainable molecules becoming the body of the tidemark, as a scar of the end of the original subchondral growth plate. Simkin speculated that the molecular remains of apoptotic deep zone chondrocytes are driven down by normal joint usage to the front of the calcified cartilage, maintaining this stained line even through adulthood [37].

1.3.4.2 Cement Line

The cement line is the boundary between the calcified cartilage and the subchondral bone plate. Unlike the tidemark, it undulates very strongly, to the point which it forms interdigitating fingers between the calcified cartilage and bone, possibly fortifying the physical bond between the two layers. The "fingers" of the interdigitating bone are often the result of the previously described vascular channels, with their closed bony caps poking up into the calcified cartilage, creating a bumpy cement line surface [14].

1.3.4.3 ScP End Boundary

The ScP end boundary separates the subchondral bone plate and the underlying trabecular bone. In contrast to the tidemark and cement line, it is not a physical line that can be seen between the layers, but an imaginary surface that separates the corticalized bone of the subchondral bone plate from the cancellous bone. It has been defined in order to measure the thicknesses of both the subchondral bone plate and the subchondral plate [21, 22]. Immediately deep to this boundary are the large spaces of

pulpous marrow of the trabecular bone, comprised of fat cells and connective tissue, and supported by surrounding trabecular bone struts.
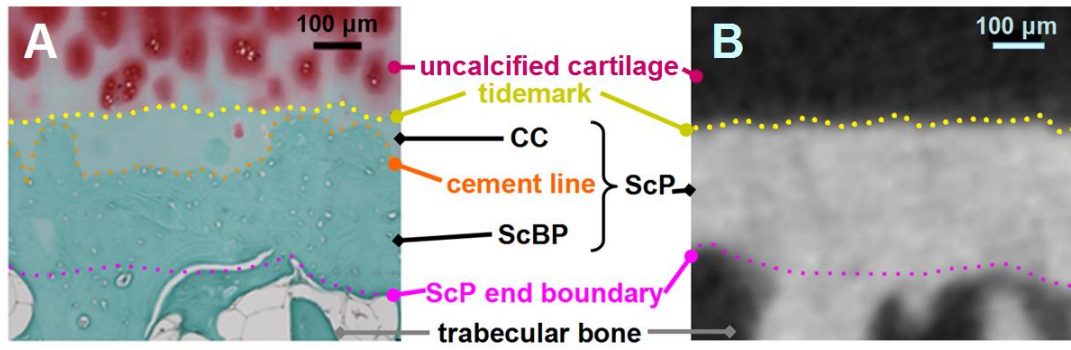
Figure 1.2: Location of Articular Cartilage and Subchondral Plate. Layer and border definitions of the osteochondral unit, including the uncalcified articular cartilage, and the subchondral plate (calcified cartilage+subchondral bone plate), shown with (A) histology and (B) microCT.

Table 1.1: Glossary of Terms and Length Scales.

Structural Feature	Definition	Length Scale (in distal MFC)
articular cartilage (AC)	hyaline cartilage covering joint surface	1-3 mm thickness
calcified cartilage (CC)	mineralized layer of cartilage, beneath hyaline cartilage and superficial to subchondral bone plate	100-200 μm thickness
chondrocyte	cells embedded in cartilage matrix	~10 μm
cartilage matrix	the matrix of articular cartilage, comprised mainly of collagen, PGs, water	same as AC 1-3 mm thickness
subchondral bone plate (ScBP)	thin layer of "corticalized" bone, beneath calcified cartilage and superficial to cancellous bone	100-200 μm thickness
subchondral plate (ScP)	combined CC and ScBP layers within an osteochondral junction	200-400 μm thickness
tidemark (TM)	interface between uncalcified and calcified cartilage	<10 μm thickness
tidemark discontinuity	break or disruption in the tidemark caused by abnormal structure, such as vascular channel, remodeling site	variable, 20-100 μm
cement line	interface between subchondral bone and cartilage	<10 μm thickness
osteoclast	bone-resorbing cell	50 - 200 μm diameter XYZ
osteoblast	bone-forming cell	10 – 20 μm diameter XYZ
osteocyte	bone cells residing within mature bone	10 – 20 μm diameter XYZ
subchondral plate pore	any non-calcified void within the ScBP	*may be any of below*
basic multicellular unit (BMU)/ resorption pit	unit of bone remodeling consisting of an active vascular channel with an osteoclastic front and trailing osteoblasts depositing osteoid	30-100 μm diameter
vascular channel	blood vessel(s) and enveloping bone tissue	30-70 μm diameter 100 μm – 1 mm length
marrow void	bone marrow pocket within the subchondral bone	50 μm – 1 mm diameter
osteoid deposits	undermineralized, immature bone regions	100 – 1 mm diameter
microcrack	fissure within the calcified cartilage or subchondral bone plate	2-7 μm diameter 25-200 μm length
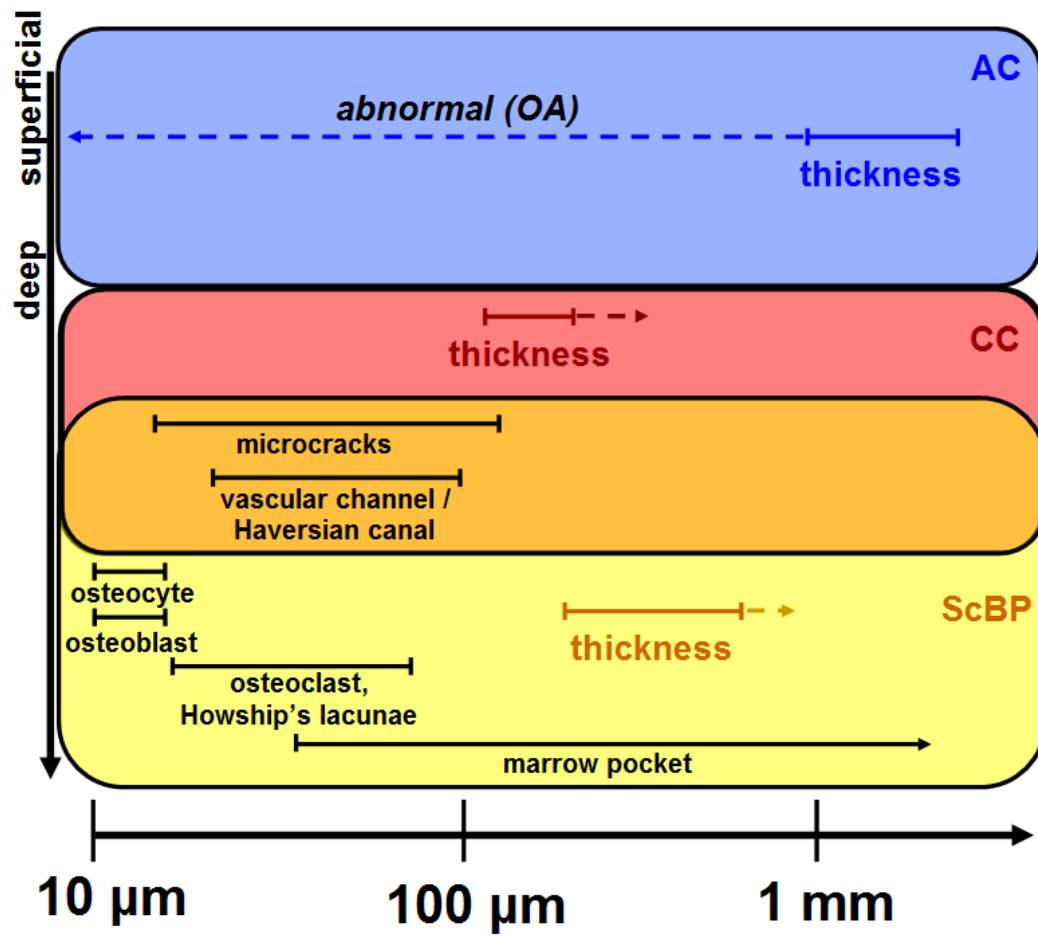
Figure 1.3: Length Scales of Subchondral Plate Components. Visual representation of the scale of biological and structural components inside the subchondral plate.

1.4 Articular Cartilage and Subchondral Plate Visualization Methods

The articular cartilage and subchondral plate each have structural properties at the tissue scale in their thickness and interface morphology, as well as microscale components within such as chondrocytes, vascular channels, and bone cells. To be able to understand how they change and interact with age-related degeneration and the onset of osteoarthritis to investigate the pathogenesis, multiscale visualization strategies need to be used. Some of these imaging techniques need to have field/volume of view capabilities capable of capturing and computing the macroscale tissue parameters, while complementary techniques also need to be used to visualize how the microscale features change in their biology, morphology and density in detail, to understand how the latter can result in the former. In this section, the known visualization features of the tissue, components, and cells of both the cartilage and bone are discussed, using two of the most conventional osteochondral tissue imaging techniques, histology and microcomputed tomography (**Fig. 1.2**).

1.4.1 Histology

1.4.1.1 Articular Cartilage

In conventional stains of the articular cartilage, Hematoxylin-Eosin and SafraninO-Fast Green, the matrix of the articular cartilage stains for the eosonophilic agent. With SafraninO, there is also a rough indicator of the proteoglycan content, as glycosaminoglycan rich regions stain for it. There is usually no further detail in the matrix, such as of the collagen fibril orientation. Within the matrix, there are the many

chondrocytes which stain at their nuclei for the basophilic agent, and are oriented based on zone, superficial, middle or deep.

1.4.1.2 Subchondral Plate

The calcified cartilage of the subchondral plate is closer in chemical composition to the subchondral bone than the articular cartilage. It has low proteoglycan content and usually will not stain for SafraninO to the degree of the uncalcified cartilage, but contains the occasional chondrocytes, which are organized as in the deep zone and are sometimes hypertrophic. Because of the lack of staining in many methods, the calcified cartilage is most readily identified by first visualizing the cement line and tidemark and identifying the layer as between the two borders. The tidemark appears as a metachromatic dark line, thought to be comprised of remnants of chondrocytes that have previously undergone apoptosis and which are pushed against the barrier of the calcification front [37]. The cement line is the interdigitating line between the cartilage and bone, which is clearly distinct due to the lack of lamellar sheet lines in the former [14].

The subchondral bone plate takes on a histological appearance similar to that of classically described compact or cortical bone. Like all human bone, it is comprised of lamellar sheets, which run relatively parallel to the cement line. In an en face view, the bone structure is usually seen to be made up of osteon subunits as in the cortical bone. That is, the lamellar sheets are divided into many concentrically oriented units in this view, containing at the center an individual vascular channel or Haversian canal as well as a neurovascular bundle. There are many osteocytes, or inactive bone cells embedded in bone matrix, lining the lamellae within each osteon [23].

1.4.1.3 Subchondral Plate Components

Vascular channels, such as the capillaries in the Haversian canals, are visible in histological sections as orifices on the order of 50 μm in diameter with a lining of endothelial cells. The aspect ratio of the orifice can vary depending on the orientation of the channel with respect to the orientation of the section. In vertical sections, the osteon structure surrounding the Haversian canal will not be clear because of the differential orientation, but in horizontal section the structure will be evident. The vascular endothelium can be clarified with dedicated markers for specific endothelial cell types, but in the context of bone histology, nuclei stains such as hematoxylin are typically sufficient [23].

The remodeling bone cells, which are associated with the active vascular channels, stain for nuclei with basophilic agents. The osteoclasts are large, 50-100 um diameter multi-nucleated cells that resorb bone, often associated with a Howship's lacunae or small regions that have been cleaned of the recently digested bone. Osteoblasts are singly nucleated cells 20-30 um in diameter with a fibroblastic appearance. These cells can be definitively identified with specialized stains [23].

1.4.2 microCT

1.4.2.1 Articular Cartilage

In microCT, the articular cartilage is the dark volume, in comparison to bone, superficial to the subchondral plate, as it is low attenuation. Without the use of contrast agents, no biological contrast of the matrix components or cells is possible. Even with the use of contrast, the resolvability of the components is not as good as histology.

1.4.2.2 Subchondral Plate

The calcified cartilage and subchondral bone plate have similar mineralization and high attenuation in microCT, and cannot be segregated to the individual layers. Together, they are the bright, continuous thin layer beneath the articular cartilage. The tidemark boundary of the calcified cartilage is clearly visible as the mineralization front, and the ScP end boundary can also be distinguished as distal to the marrow voids, which are low attenuation spots in the bone.

1.4.2.3 Subchondral Plate Components

The vascular channels of the subchondral plate can be seen as gray protrusions in the bright bone if they are large enough in diameter above the resolution limit. Cell features such as osteoclasts, osteoblasts, and osteocytes, are usually not resolvable. MicroCT also cannot distinguish vascular channels based on their activity due to its inability to see these cells.

1.4.4 Other Imaging Methods

Although microCT has inferior resolution and contrast to histology, it has a distinct advantage in that it can resolve the structures in 3-D, and is not as susceptible to sampling problems from visualizing thin sections and interpolating with stereology. As such, it is superior for quantification of subchondral plate porosity, although there is limited ability to categorize the vascular channels with such a method. A method which gives a view of the 3-D surfaces and cross-sections, but in 2-D projection images, is standard electron microscopy, which was used by Clark to establish the current understanding of the structure of the subchondral plate (**Fig. 1.4**). In these studies, SEM of the normal human osteochondral interface after treatment with papain or bleach to reveal the CC or ScBP superficial surface, respectively, was used to establish

and categorize the subchondral pores as vascular channel capillaries and small marrow spaces in 3-D [8, 28].
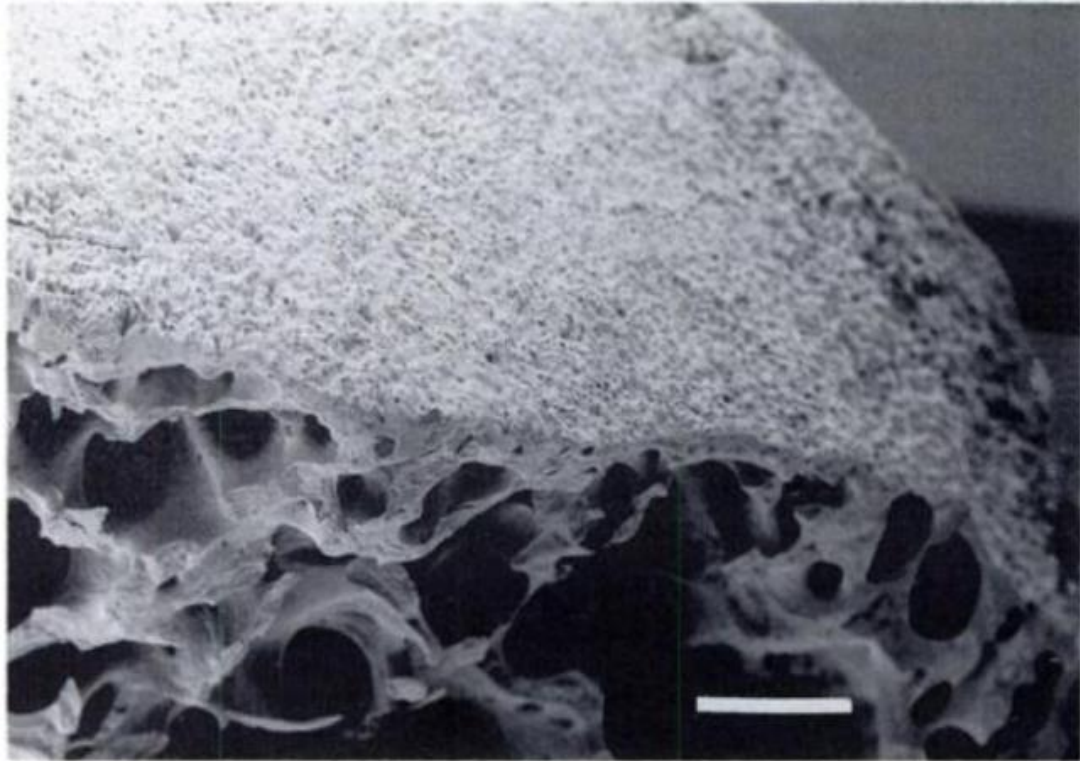
Figure 1.4: Subchondral Plate Visualized by SEM. The 3-D structure of the subchondral plate seen through scanning electron microscopy, with the uncalcified cartilage digested with papain. The subchondral plate contains numerous pores (small holes on surface of calcified tissue in upper half of image) and is situated above the trabecular bone (cancellous bone in lower half of image). White scale bar = 1 mm. From [8].

1.5 Articular Cartilage and Subchondral Plate Changes with Degeneration and Osteoarthritis

1.5.1 Alterations of the Articular Cartilage

In degeneration leading to early osteoarthritis, there is alteration in the cellularity and organization of the chondrocytes, along with fibrillation and deterioration of the cartilage matrix [38-40]. Particularly, there are formation of regions of local hypocellularity in the matrix, caused by loss of individual chondrocytes and chondrons in some locations and proliferation at others, leading to large cell clusters. The clustering is often localized near fissures and clefts that form on the matrix of the cartilage as the surface becomes fibrillated and irregular [13]. Chondrocytes have limited ability to remodel at a distance, leaving the matrix farther from cells susceptible to more damage. In later stages of degeneration, there is loss of the organization of the chondrons into superficial, middle, and deep zones, to go along with more severe cell clustering [12, 41].

1.5.2 Alterations of the Subchondral Plate

1.5.2.1 Early Stage Degeneration

The increased subchondral plate remodeling activity in early stage degeneration has substantial effects on its composition and structure. Mineral apposition rate can increase by as much as threefold to fivefold above normal along with the initiation of new remodeling sites throughout the bone, the subchondral bone plate thins [42-44]. This change is coupled with reduced density of the bone, some degree of thinning of the trabeculae, and increased porosity of the subchondral bone region [20]. Vascular

invasion of the calcified cartilage zone and increased vascularity overall of the subchondral plate occur in this stage [45].

1.5.2.2 Later Stage Changes

The subchondral plate undergoes sclerosis in the late stages of OA. The volume increases, resulting in a thicker subchondral plate [46]. This involved thickening of both the corticalized subchondral bone plate and advancement of the calcified cartilage, evidenced by multiple tidemarks [47, 48]. Although the bone volume density of the subchondral bone increases in sclerosis, the bone material density, or the mineralization of the bone, decreases [49-51]. This results in subchondral bone that is greater in volume but less stiff and mechanically weaker than in the normal state, with inhomogeneities in regions where the cartilage is more heavily eroded.

1.5.3 Alterations of the Subchondral Plate Components, Boundaries, and Barrier Function

With the increased remodeling of the subchondral plate and associated vascular invasion, it is known that the vascular channels also become more active, but there has not been much quantitative data to definitively show this. In normal tissue of individuals 60 years or older, the density of active vascular channels starts to increase in the human femoral head, potentially related to age-related degeneration [52]. In human femoral condyle OA tissue with partial thickness erosion, additional types of vascular channels are seen, which are more likely to contain active vascular channels and penetrate past the tidemark (**Fig. 1.5**) [31]. This invasion of vascular channels past the tidemark was also seen in the femoral head, but more commonly in the non-weight bearing regions of the joint, suggesting that this may be an early stage degeneration [53].

Because of the formation of the additional tidemarks, there has been the theory that the aberrant remodeling that occurs is to a degree a recapitulation of that which occurs during development or endochondral ossification. The tidemark is speculated to be a scar of the subchondral growth plate. Thus, the multiple tidemarks may signify that more bone and calcified cartilage is being formed as part of the remodeling in some aberrant response to the abnormality of the other tissue [37].

The penetration of channels past the tidemark along with the tidemark irregularity, duplication, and discontinuity, can potentially lead to compromise of one of the main functions of the subchondral plate as a low permeability barrier. In human tissue, the hydraulic conductivity of the osteochondral unit as a whole decreases substantially with partial and full thickness erosion of the cartilage [16]. This is partly due to deterioration of the cartilage matrix in its ability to retain fluid, but may also relate to the structural deterioration of the subchondral plate as well. An increase in permeability has also been observed in the subchondral plate of OA-induced mouse models [54].
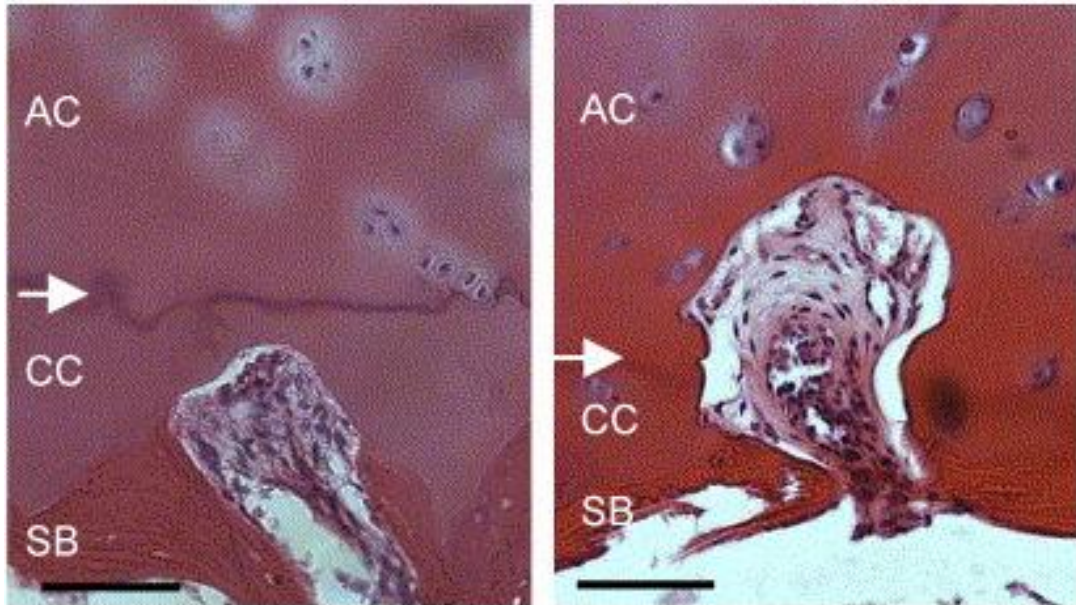
Figure 1.5: Resorption Pits of the Subchondral Plate. Histology (hematoxylin and eosin) sections showing resorption pits in the subchondral plate, which are also termed "active vascular channels" or "basic multicellular units (BMU)". Left: resorption pit under the tidemark. Right: resorption pit protruding past tidemark. Scale bar: 50 µm. From [31].

1.5.4 Transition from Age-Related Degeneration to Osteoarthritis

The observable signs and symptoms with the onset of OA: full thickness cartilage erosion and joint space narrowing, osteophytes, diminished intrinsic fluorescence of the cartilage tissue, joint pain, stiffness and inflammation, represent a key change from age-related degeneration, where there is little or no pain and abnormality and the cartilage may only be fibrillated or partially eroded [55]. However, the mechanism of the transition from age-related degeneration to OA is unclear. Several mechanisms which center on the loss of the barrier function of the subchondral plate are possible.

1.5.4.1 Potential Mechanisms through the Osteochondral Interface

The causes of the bone remodeling imbalances which occur in early OA may involve mechanisms which include cellular signaling for microdamage repair, vascular stimulation through angiogenic factors such as VEGF, and bone-cartilage crosstalk via pores in the subchondral bone or vascular channels, which all likely occur as part of a feedback loop with the deterioration of the overlying articular cartilage. Due to the nature of studying these mechanisms by manipulating the tissue to induce OA, most of these have been obtained through the use of animal models.

Cellular Signaling

In deteriorating cartilage and remodeling bone, elevated levels of cellular signaling factors such as growth factor β, interleukin (IL)-1, IL-6, and prostaglandin E_2 have been detected, which are both products and stimulators of bone remodeling [56]. Osteoblasts from OA joints produce twofold to sixfold more IL-6 and prostaglandin E_2 than normal joints, and the Wnt signaling pathway is upregulated [57, 58]. The OPG-RANKL ratio decreases in osteocytes in OA animal models, indicating a signaling bias

towards bone remodeling and resorption [59]. The change in the regulation of these factors are hypothesized to be a part of the response to the creations of microcracks within the bone, as microcracks potentially are points of origin for new remodeling events [33, 60, 61].

Vascular Invasion

Bone remodeling is linked with increased vascularization of both the subchondral bone and calcified cartilage [32, 45, 62]. This can occur as a consequence of stimulation of angiogenic growth factors such as vascular endothelial growth factor, which has been found to be elevated in synovial fluid of most OA patients [63]. Angiogenic factors have the additional effect of inducing chondrocytes to secrete catabolic proteins such as matrix metalloproteinases which can deteriorate the overlying cartilage [64, 65], altering the load balance of the joint, and subsequently stimulating more bone remodeling and vascularization in a feedback loop.

Bone-Cartilage Crosstalk

The pores in the subchondral bone, which are not limited to vascular channels and can include structures such as marrow spaces, Haversian canals, lacunae, and other miscellaneous perforations, are potential pathways of communication between the subchondral bone and cartilage [8, 24, 66]. The density of these pores can be exacerbated by the bone remodeling that occurs with OA initiation and progression, as osteoclastic resorption in the subchondral bone region can lead to increased plate perforation [67]. The ability of the pores to transmit solutes between the articular cartilage and subchondral bone has been demonstrated using sodium fluoroscein tracing [15, 54]. How this crosstalk between articular cartilage and bone can affect bone

remodeling is unclear, but likely involves altered diffusion rates of the aforementioned signaling factors [16].

1.5.4.2 Cartilage-Bone Deterioration

Bone remodeling is likely part of a feedback loop with the deterioration and compromise of the matrix of the overlying articular cartilage [20]. In this model, the remodeling initially increases because of high and repetitive joint loads [68]. The age-related degeneration and bone remodeling leaves the subchondral plate roughened and discontinuous [67]. Combined with the penetrating vascular channels, the barrier function of the ScP can be compromised, leading to abnormal cartilage-bone communication. The invading vasculature is associated with stimulation of angiogenic factors, which can have the additional effect of inducing chondrocytes to synthesize and stimulate matrix metalloproteinases and catabolic enzymes such as ADAMTS, which gradually degrade the cartilage matrix [63-65]. The coupling of increased communication and introduction of pro-catabolic cytokines can then mediate the loss of proteoglycan and breakdown of the articular cartilage, increasing the loads the subchondral bone is subjected to, leading to more remodeling and perpetuation of the feedback loop.

1.6 References

1. Lawrence RC, Felson DT, Helmick CG, Arnold LM, Choi H, Deyo RA, Gabriel S, Hirsch R, Hochberg MC, Hunder GG, Jordan JM, Katz JN, Kremers HM, Wolfe F. Estimates of the prevalence of arthritis and other rheumatic conditions in the United States. Part II. Arthritis Rheum 2008;58: 26-35.

2. Bitton R. The economic burden of osteoarthritis. The American journal of managed care 2009;15: S230-5.

3. Petersson IF, Boegard T, Saxne T, Silman AJ, Svensson B. Radiographic osteoarthritis of the knee classified by the Ahlback and Kellgren & Lawrence systems for the tibiofemoral joint in people aged 35-54 years with chronic knee pain. Annals of the rheumatic diseases 1997;56: 493-6.

4. Altman R, Asch E, Bloch D, Bole G, Borenstein D, Brandt K, Christy W, Cooke TD, Greenwald R, Hochberg M, et al. Development of criteria for the classification and reporting of osteoarthritis. Classification of osteoarthritis of the knee. Diagnostic and Therapeutic Criteria Committee of the American Rheumatism Association. Arthritis Rheum 1986;29: 1039-49.

5. Little CB, Hunter DJ. Post-traumatic osteoarthritis: from mouse models to clinical trials. Nature reviews. Rheumatology 2013;9: 485-97.

6. Oegema TR, Jr., Carpenter RJ, Hofmeister F, Thompson RC, Jr. The interaction of the zone of calcified cartilage and subchondral bone in osteoarthritis. Microscopy research and technique 1997;37: 324-32.

7. Redler I, Mow VC, Zimny ML, Mansell J. The ultrastructure and biomechanical significance of the tidemark of articular cartilage. Clinical orthopaedics and related research 1975: 357-62.

8. Clark JM, Huber JD. The structure of the human subchondral plate. The Journal of bone and joint surgery. British volume 1990;72: 866-73.

9. Maroudas A. Physical chemistry and the structure of cartilage. The Journal of physiology 1972;223: 21P-22P.

10. Hunziker EB, Michel M, Studer D. Ultrastructure of adult human articular cartilage matrix after cryotechnical processing. Microscopy research and technique 1997;37: 271-84.

11. Youn I, Choi JB, Cao L, Setton LA, Guilak F. Zonal variations in the three-dimensional morphology of the chondron measured in situ using confocal

microscopy. Osteoarthritis and cartilage / OARS, Osteoarthritis Research Society 2006;14: 889-97.

12. Poole AR, Kojima T, Yasuda T, Mwale F, Kobayashi M, Laverty S. Composition and structure of articular cartilage: a template for tissue repair. Clinical orthopaedics and related research 2001: S26-33.

13. Lotz MK, Otsuki S, Grogan SP, Sah R, Terkeltaub R, D'Lima D. Cartilage cell clusters. Arthritis and rheumatism 2010;62: 2206-18.

14. Madry H, van Dijk CN, Mueller-Gerbl M. The basic science of the subchondral bone. Knee surgery, sports traumatology, arthroscopy : official journal of the ESSKA 2010;18: 419-33.

15. Pan J, Zhou X, Li W, Novotny JE, Doty SB, Wang L. In situ measurement of transport between subchondral bone and articular cartilage. Journal of orthopaedic research : official publication of the Orthopaedic Research Society 2009;27: 1347-52.

16. Hwang J, Bae WC, Shieu W, Lewis CW, Bugbee WD, Sah RL. Increased hydraulic conductance of human articular cartilage and subchondral bone plate with progression of osteoarthritis. Arthritis and rheumatism 2008;58: 3831-42.

17. Muller-Gerbl M, Schulte E, Putz R. The thickness of the calcified layer of articular cartilage: a function of the load supported? Journal of Anatomy 1987;154: 103-11.

18. Oettmeier R, Abendroth K, Oettmeier S. Analyses of the tidemark on human femoral heads. I. Histochemical, ultrastructural and microanalytic characterization of the normal structure of the intercartilaginous junction. Acta morphologica Hungarica 1989;37: 155-68.

19. Mente PL, Lewis JL. Elastic modulus of calcified cartilage is an order of magnitude less than that of subchondral bone. Journal of orthopaedic research : official publication of the Orthopaedic Research Society 1994;12: 637-47.

20. Burr DB, Gallant MA. Bone remodelling in osteoarthritis. Nature reviews. Rheumatology 2012;8: 665-73.

21. Milz S, Putz R. Quantitative morphology of the subchondral plate of the tibial plateau. Journal of Anatomy 1994;185 (Pt 1): 103-10.

22. Milz S, Eckstein F, Putz R. The thickness of the subchondral plate and its correlation with the thickness of the uncalcified articular cartilage in the human patella. Anat Embryol (Berl) 1995;192: 437-44.

23. Williams PL, Warwick, R. Gray's Anatomy. 36th ed, B.L. Dyson M1980, Philadelphia, PA: Longman Group, Ltd.

24. Duncan H, Jundt J, Riddle JM, Pitchford W, Christopherson T. The tibial subchondral plate. A scanning electron microscopic study. The Journal of bone and joint surgery. American volume 1987;69: 1212-20.

25. Radin EL, Paul IL, Lowy M. A comparison of the dynamic force transmitting properties of subchondral bone and articular cartilage. The Journal of bone and joint surgery. American volume 1970;52: 444-56.

26. Radin EL, Rose RM. Role of subchondral bone in the initiation and progression of cartilage damage. Clinical orthopaedics and related research 1986: 34-40.

27. Pugh JW, Rose RM, Radin EL. A structural model for the mechanical behavior of trabecular bone. Journal of biomechanics 1973;6: 657-70.

28. Clark JM. The structure of vascular channels in the subchondral plate. Journal of Anatomy 1990;171: 105-15.

29. Yoffey JM. A note on the thick-walled and thin-walled arteries of bone marrow. Journal of Anatomy 1962;96: 425.

30. Jilka RL. Biology of the basic multicellular unit and the pathophysiology of osteoporosis. Medical and pediatric oncology 2003;41: 182-5.

31. Shibakawa A, Yudoh K, Masuko-Hongo K, Kato T, Nishioka K, Nakamura H. The role of subchondral bone resorption pits in osteoarthritis: MMP production by cells derived from bone marrow. Osteoarthritis and cartilage / OARS, Osteoarthritis Research Society 2005;13: 679-87.

32. Findlay DM. Vascular pathology and osteoarthritis. Rheumatology 2007;46: 1763-8.

33. Mori S, Harruff R, Burr DB. Microcracks in articular calcified cartilage of human femoral heads. Archives of pathology & laboratory medicine 1993;117: 196-8.

34. Sokoloff L. Microcracks in the calcified layer of articular cartilage. Arch Pathol Lab Med 1993;117: 191-195.

35. Karsenty G, Wagner EF. Reaching a genetic and molecular understanding of skeletal development. Developmental cell 2002;2: 389-406.

36. Ferguson VL, Ayers RA, Bateman TA, Simske SJ. Bone development and age-related bone loss in male C57BL/6J mice. Bone 2003;33: 387-98.

37. Simkin PA. Consider the tidemark. The Journal of rheumatology 2012;39: 890-2.

38. Collins DH. The Pathology of Articular and Spinal Disease. London: Arnold; 1949.

39. Mankin HJ, Dorfman H, Lipiello L, Zarins A. Biochemical and metabolic abnormalities in articular cartilage from osteoarthritic human hips. II. Correlation of morphology with biochemical and metabolic data. J Bone Joint Surg Am 1971;53-A: 523-37.

40. Lee GM, Paul TA, Slabaugh M, Kelley SS. The incidence of enlarged chondrons in normal and osteoarthritic human cartilage and their relative matrix density. Osteoarthritis Cartilage 2000;8: 44-52.

41. Eggli PS, Hunziker EB, Schenk RK. Quantitation of structural features characterizing weight- and less-weight-bearing regions in articular cartilage: a stereological analysis of medial femoral condyles in young adult rabbits. Anat Rec 1988;222: 217-227.

42. Amir G, Pirie CJ, Rashad S, Revell PA. Remodelling of subchondral bone in osteoarthritis: a histomorphometric study. Journal of clinical pathology 1992;45: 990-2.

43. Benske J, Schunke M, Tillmann B. Subchondral bone formation in arthrosis. Polychrome labeling studies in mice. Acta orthopaedica Scandinavica 1988;59: 536-41.

44. Intema F, Sniekers YH, Weinans H, Vianen ME, Yocum SA, Zuurmond AM, DeGroot J, Lafeber FP, Mastbergen SC. Similarities and discrepancies in subchondral bone structure in two differently induced canine models of osteoarthritis. Journal of bone and mineral research : the official journal of the American Society for Bone and Mineral Research 2010;25: 1650-7.

45. Hulth A. Does osteoarthrosis depend on growth of the mineralized layer of cartilage? Clinical orthopaedics and related research 1993: 19-24.

46. Fazzalari NL, Parkinson IH. Fractal properties of subchondral cancellous bone in severe osteoarthritis of the hip. Journal of bone and mineral research : the official journal of the American Society for Bone and Mineral Research 1997;12: 632-40.

47. Karsdal MA, Leeming DJ, Dam EB, Henriksen K, Alexandersen P, Pastoureau P, Altman RD, Christiansen C. Should subchondral bone turnover be targeted when treating osteoarthritis? Osteoarthritis and cartilage / OARS, Osteoarthritis Research Society 2008;16: 638-46.

48. Bonde HV, Talman ML, Kofoed H. The area of the tidemark in osteoarthritis-- a three-dimensional stereological study in 21 patients. APMIS : acta pathologica, microbiologica, et immunologica Scandinavica 2005;113: 349-52.

49. Arden NK, Griffiths GO, Hart DJ, Doyle DV, Spector TD. The association between osteoarthritis and osteoporotic fracture: the Chingford Study. British journal of rheumatology 1996;35: 1299-304.

50. Grynpas MD, Alpert B, Katz I, Lieberman I, Pritzker KP. Subchondral bone in osteoarthritis. Calcified Tissue International 1991;49: 20-6.

51. Hannan MT, Felson DT, Anderson JJ. Bone mineral density in elderly men and women: results from the Framingham osteoporosis study. Journal of bone and mineral research : the official journal of the American Society for Bone and Mineral Research 1992;7: 547-53.

52. Lane LB, Villacin A, Bullough PG. The vascularity and remodelling of subchondrial bone and calcified cartilage in adult human femoral and humeral heads. An age- and stress- related phenomenon. J Bone Joint Surg Br 1977;59: 272-8.

53. Oettmeier R, Abendroth K, Oettmeier S. Analyses of the tidemark on human femoral heads. II. Tidemark changes in osteoarthrosis--a histological and histomorphometric study in non-decalcified preparations. Acta Morphol Hung 1989;37: 169-80.

54. Pan J, Wang B, Li W, Zhou X, Scherr T, Yang Y, Price C, Wang L. Elevated cross-talk between subchondral bone and cartilage in osteoarthritic joints. Bone 2012;51: 212-7.

55. Temple-Wong MM, Bae WC, Chen MQ, Bugbee WD, Amiel D, Coutts RD, Lotz M, Sah RL. Biomechanical, structural, and biochemical indices of degenerative and osteoarthritic deterioration of adult human articular cartilage of the femoral condyle. Osteoarthritis Cartilage 2009; 17: 1469-76.

56. Mansell JP, Collins C, Bailey AJ. Bone, not cartilage, should be the major focus in osteoarthritis. Nature clinical practice. Rheumatology 2007;3: 306-7.

57. Massicotte F, Lajeunesse D, Benderdour M, Pelletier JP, Hilal G, Duval N, Martel-Pelletier J. Can altered production of interleukin-1beta, interleukin-6, transforming growth factor-beta and prostaglandin E(2) by isolated human subchondral osteoblasts identify two subgroups of osteoarthritic patients. Osteoarthritis and cartilage / OARS, Osteoarthritis Research Society 2002;10: 491-500.

58.   Weng LH, Wang CJ, Ko JY, Sun YC, Wang FS. Control of Dkk-1 ameliorates chondrocyte apoptosis, cartilage destruction, and subchondral bone deterioration in osteoarthritic knees. Arthritis and rheumatism 2010;62: 1393-402.

59.   Bellido M, Lugo L, Roman-Blas JA, Castaneda S, Caeiro JR, Dapia S, Calvo E, Largo R, Herrero-Beaumont G. Subchondral bone microstructural damage by increased remodelling aggravates experimental osteoarthritis preceded by osteoporosis. Arthritis research & therapy 2010;12: R152.

60.   Bentolila V, Boyce TM, Fyhrie DP, Drumb R, Skerry TM, Schaffler MB. Intracortical remodeling in adult rat long bones after fatigue loading. Bone 1998;23: 275-81.

61.   Verborgt O, Gibson GJ, Schaffler MB. Loss of osteocyte integrity in association with microdamage and bone remodeling after fatigue in vivo. Journal of bone and mineral research : the official journal of the American Society for Bone and Mineral Research 2000;15: 60-7.

62.   Conaghan PG, Vanharanta H, Dieppe PA. Is progressive osteoarthritis an atheromatous vascular disease? Annals of the rheumatic diseases 2005;64: 1539-41.

63.   Brown RA, Tomlinson IW, Hill CR, Weiss JB, Phillips P, Kumar S. Relationship of angiogenesis factor in synovial fluid to various joint diseases. Annals of the rheumatic diseases 1983;42: 301-7.

64.   Brown RA, Weiss JB. Neovascularisation and its role in the osteoarthritic process. Annals of the rheumatic diseases 1988;47: 881-5.

65.   Luyten FP, Lories RJ, Verschueren P, de Vlam K, Westhovens R. Contemporary concepts of inflammation, damage and repair in rheumatic diseases. Best practice & research. Clinical rheumatology 2006;20: 829-48.

66.   Lyons TJ, McClure SF, Stoddart RW, McClure J. The normal human chondro-osseous junctional region: evidence for contact of uncalcified cartilage with subchondral bone and marrow spaces. BMC musculoskeletal disorders 2006;7: 52.

67.   Botter SM, van Osch GJ, Waarsing JH, Day JS, Verhaar JA, Pols HA, van Leeuwen JP, Weinans H. Quantification of subchondral bone changes in a murine osteoarthritis model using micro-CT. Biorheology 2006;43: 379-88.

68.   Frost HM. Perspective: genetic and hormonal roles in bone disorders: insights of an updated bone physiology. Journal of musculoskeletal & neuronal interactions 2003;3: 118-35.

CHAPTER 2:

HUMAN SUBCHONDRAL PLATE STRUCTURE FROM MICRO-COMPUTED TOMOGRAPHY: ALTERATIONS WITH OSTEOARTHRITIS

2.1 Abstract

Introduction. The subchondral plate (ScP), consisting of calcified cartilage and the subchondral bone plate, is a biological and biomechanical interface between non-calcified cartilage and trabecular bone. This interface undergoes remodeling and alterations, including those associated with cartilage deterioration and erosion with aging and osteoarthritis (OA). The ScP contains sparse vascular canals which are involved in ScP remodeling and may contribute to OA, but is difficult to segment for analysis due to its relatively thin, sheet-like structure. The aims of this study were to (1) determine and compare (a) tidemark roughness, (b) ScP thickness, (c) ScP porosity in human medial femoral condyle samples exhibiting three grades of cartilage deterioration (normal, degenerated and non-eroded, or degenerated and partial-thickness erosion), and (2) evaluate the correspondence of these metrics with biological structures visualized by registered histology.

Methods. Adult human osteochondral samples (10-12 donors/group) were imaged in a $(2 \text{ mm})^3$ volume by µCT at $(9 \text{ µm})^3$ voxel resolution. Then, morphometric analysis was

performed on the ScP regions, between the interface with uncalcified articular cartilage and the marrow surface, determined from three measures, texture intensity, histograms, and locations of marrow spongiosa peaks. Some samples were processed for histology, imaged and registered for biological and structural correlation. Another sample was scanned additionally by μCT at $(2\ \mu m)^3$ voxel resolution. These images were registered to a slice from the $(9\ \mu m)^3$ μCT data.

Results. With cartilage deterioration, the 3-D morphometric parameter analysis delineated alterations that reflected histological indices of bone remodeling with cartilage deterioration: roughening of the tidemark prior to substantial cartilage erosion, and an increase in ScP thickness and decrease in porosity underlying partially eroded cartilage. Histologically, the surface of the tidemark matched that surface identified in μCT data, and the vascular channels and marrow pockets in the ScP matched pores identified in μCT data.

Discussion. The identification by μCT of ScP roughening in early stage deterioration supports the possible role of structural alterations in OA progression, with one pathway leading to deprivation of vascular support to cartilage by a thickened, less porous ScP.

2.2   Introduction

In the normal adult synovial articulating joint, the articular cartilage is attached to underlying trabecular bone (TB) by a subchondral plate (ScP) composed of two tissue layers, calcified cartilage (CC), ~100 μm thick, and "corticalized" subchondral bone plate (ScBP), ~300 μm thick [1] (**Table 2.1**). The ScBP and CC vary between anatomical sites and individuals, in both the thickness of each structure and the morphology of their boundaries, the cement line (ScBP-CC boundary) and tidemark (articular cartilage-CC boundary) (**Fig. 2.1**) [1-3]. The structure of the ScBP reflects remodeling [4], mediated by biological entities at the microstructural level, which may be involved in OA. This remodeling is evident both by changes within the ScP, as well as at the tidemark, which reflects the position of the original subchondral growth plate during development, and undergoes duplication and reshaping in an ongoing remodeling process [5].

The ScBP and CC contain occasional vascular channels which are important in bone remodeling and OA pathogenesis [3, 6]. Vascular channels are 20-70 μm diameter fingerlike branches that extend from larger marrow spaces, and consist of one or more central capillaries surrounded circumferentially by lamellar bone. This bony cap may be fenestrated, with the endothelial cells lining the capillary in contact with surrounding tissue, such as calcified cartilage [3]. Vascular channels comprise a sizeable portion of the "subchondral pores", defined by Burr and Clark as the many pores or small voids which are present in the ScP [6, 7]. Pores which are not vascular channels may still be involved in remodeling by supporting localized sites of active remodeling bone cells on marrow surfaces [1, 8]. Subchondral pores may include microcracks of the bone and

CC, which can be as long as 120 µm, and are sites for invasion of vascular channels and development of "remodeling bays" [9-11]. The role of the subchondral pores in the subchondral bone remodeling that accompanies cartilage erosion in OA is still being elucidated [7]. The invasion of vascular channels past the tidemark in OA is evidence that some of these pores are communication channels [12], providing a link between cartilage and bone as they change in disease. Subchondral pore density and penetration depth can potentially affect the permeability of both fluid and solutes to the surrounding tissues.

Investigation of the structure of the ScBP and CC at the length scale of 1-100 µm has identified subchondral pores and their interaction with cartilage in OA. The classical approach has been to use 2-D views of cross sections or surfaces of the osteochondral interface. SEM of the normal human osteochondral junction after treatment with papain or bleach, to reveal the CC or ScBP superficial surface, respectively, has established that each structure is variably penetrated by subchondral pores [3, 6]. Histology has identified various types of pores, from capillaries with varying degrees of fenestration, marrow spaces of varying sizes, to microcracks containing bone cells and vascular channels [13]. Although useful in establishing the biological detail, these 2-D views provide limited information on 3-D structure and may be susceptible to sectioning artifacts. Additionally, quantification of the density per area using these methods are affected by stereological and preparation sampling effects [14].

More recently, approaches have been developed to allow visualization of the osteochondral interface in 3-D at various resolutions. These include reconstruction of serial histologic sections, SEM, and micro-computed tomography (µCT). Using serial

histology, the ScP has thickness of 0.10 ± 0.02 (mean ± SD) mm for CC, and 0.36 ± 0.13 mm for ScBP, and interface roughnesses of 1.14 ± 0.04 normalized surface area for the tidemark, and 1.99 ± 0.38 for the cement line [15-17]. From μCT analysis, alterations in ScP thickness indicate imbalances in resorption-formation remodeling of the bone, and disruption of the tidemark indicates aberrant remodeling in OA [12]. The quantitation of ScP thickness depends on the definition of the deep boundary, where the trabecular bone begins. This boundary can be defined [17] based on location of trabecular struts and marrow voids [16-18]. Similarly, the quantitation of the roughness depends on the fit of the reference surface to the ScP; this surface can be planar, or else quadric or spline-fit to account for joint curvature [16, 17].

In addition to roughness and thickness, other quantifiable properties such as the porosity of the ScP can be affected by remodeling. For example. the ScP porosity of the canine tibial osteochondral interface increases with induced OA [19-22]. Such pores may represent vascular channels, marrow pockets, osteoid deposits, or microcracks. ScP thickness and porosity have also been analyzed by μCT of the human vertebral endplate [23]. In the present study, μCT was used to analyze the structure of the human ScP in normal and early OA tissue samples.

We hypothesized that with increasing grade of cartilage deterioration (normal, minimally eroded OA, partially eroded OA), μCT analysis of ScP would reveal structural variations associated with biological features. The specific aims were to (1) determine and compare, for human medial femoral condyle (MFC) samples, the (a) tidemark roughness, (b) ScP thickness, (c) ScP porosity, and to (2) determine the

correspondence of these metrics with biological features in registered histological sections.

2.3   Materials and Methods

2.3.1 Study Design

The study was divided into two parts, **(1) µCT Morphometric Analysis** and **(2) Identification of µCT Features with Registered Histology**. In **(1) µCT Morphometric Analysis**, the variation of the ScP structure between donors exhibiting different cartilage deterioration grades was examined. Samples were harvested from the anterior region of the MFC or normal (NL) donor cadaveric tissue (age mean±SD 65±15 yrs, 6 M, 6 F) and OA tissue discarded during total knee arthroplasty (age mean±SD 69±9 yrs, 10 M, 10 F). The OA samples were selected to be from knees exhibiting the most common pattern of deterioration (most severe in the medial femoral condyle [24]), with 10 from each macroscopic grade, minimally eroded or partially eroded, each with an even distribution of sex and matched in age to the NL group (**Section 2.3.2**). Each of the samples was then scanned at $(9\ \mu m)^3$ resolution and processed to create a $(2\ mm)^3$ 3-D µCT data set (**Section 2.3.3**). Image data was analyzed for metrics of tidemark roughness, ScP thickness, and ScP porosity (**Table 2.2**) (**Section 2.3.4**). For tidemark roughness, three ideal fit surfaces, plane, quadric and spline, were used to calculate a roughness index metric based on the deviation from the surface. *Statistics.* Each metric was presented as mean ± SD. To compare metrics between grades, Levene's test and normality tests were applied to ensure equality of variance and normal distribution between groups, followed by one-way ANOVA with Tukey post-hoc tests, with $p < 0.05$ considered significant. An ANOVA with Tukey post-hoc was also done to verify that there was no effect of sex prior to the grade

comparisons. If either Levene's or normality test failed, then a reciprocal transform was applied and the test repeated, or non-parametric Kruskal-Wallis test was used.

In **(2) Identification of μCT Features with Registered Histology**, three samples from the morphometric analysis, one from each grade, were analyzed for the correspondence between histological and μCT features, and one sample from Grade OA-3 was also scanned at $(2 \ \mu m)^3$ resolution (**Section 2.3.3**) and then analyzed for histological correspondence, particularly at the tidemark and subchondral pores (**Section 2.3.5**). Samples were processed for histology and stained with Safranin O-Fast Green, scanned for images, registered to a 2-D image slice from the μCT dataset, and analyzed to compare the registered images. Starting from the tidemark and progressing in the deep direction, comparisons were made of the tidemark contours, vascular channels, smaller subchondral pores such as small marrow pockets, and larger marrow voids underlying the ScP.

2.3.2 Gross Grading and Sample Selection

Osteochondral tissue was graded macroscopically for gross appearance of articular cartilage (AC) using a modified Collins scale [25], and from the graded samples, donors were subsequently selected as described above so that there was a sample size of 10-12 for each of the three grades (**Table 2.3**). Grades 2-3 were defined as having a deteriorated surface, with the presence of visible unevenness, granularity, or fissuring. Grades 2 and 3 were distinguished by the thickness of the articular cartilage. The local cartilage thickness was assessed from the μCT and verified to be consistent to within 20% throughout the entire region (~50 mm^2 in surface area) for all samples

used. Cartilage thickness was taken as the mean value of the entire osteochondral region that was harvested, normal to the tidemark surface. Samples with mean thickness ≥ 1.5 mm were defined to be Grade 2, and <1.5 mm defined as Grade 3.

2.3.3 µCT Scanning and Dataset Preparation

Microcomputed tomography (µCT) imaging at $(9 \ \mu m)^3$ resolution, and subsequent image processing, were done to generate standardized, $(2 \ mm)^3$, three dimensional (3-D) datasets. The samples were scanned in a Skyscan 1076 MicroCT machine (Skyscan, Belgium) at $(9 \ \mu m)^3$ resolution, 70 kVp voltage, with air as the scanning medium, and reconstructed with NRECON software, with smoothing of the projections using an asymmetrical box filter (Skyscan). After determination of the calcified-uncalcified threshold for all µCT data, (**Section 2.3.4.1**), the sample data was cropped, rotated, and aligned so that the $(2 \ mm)^3$ volume with the ScP interface at the center of the cropped dataset, using the two offset angles of the tidemark determined by an alignment program. The $(2 \ mm)^3$ geometry of the input dataset was chosen to be able to assess local variation but also minimize effects of natural joint curvature in the femoral condyle in the morphometric analysis. One sample (Grade OA-3) was also scanned at $(2 \ \mu m)^3$ resolution in a Shimadzu SMX-160CTS MicroCT (Kyoto, Japan), with 66 kVp voltage and air as the scanning medium, for multi-resolution and histology cross-registration, as described just above.

2.3.4 µCT Dataset Analysis

The 3-D μCT $(2 \text{ mm})^3$ datasets, were image processed to segment the ScP (**Fig. 2.2**) and estimate tidemark roughness, ScP thickness, and porosity (**Fig. 2.3**), with computational analysis of the 3-D dataset as a matrix (**Table 2.4**). The orientation of the cartilage, ScP, and bone of the sample in the cropped and aligned datasets were defined relative to an x-y transverse plane, and a superficial-deep z-axis. The x-y plane was defined as that tangential to the aligned tidemark, and perpendicular to the superficial-deep axis. The z-axis was defined along the superficial-deep direction, with $z = 0$ at the top of the cropped dataset (in the cartilage, 1 mm from the aligned tidemark), with increasing height in this axis being deeper in the dataset. The tidemark was identified by thresholding (**Section 2.3.4.1**), and the ScP end boundary was identified using one of the methods used to determine ScP thickness (strut search or SS method, **Fig. 2,2**), to define the boundaries to segment the 3-D ScP. Two other methods of determining the ScP end boundary, and thus also the ScP thickness, were also computed as alternative means to standardize the measurement based on known depths of the trabecular struts and marrow voids. The sensitivity of each metric to local and global thresholding settings was assessed to ensure that the metric did not vary substantially with changes in threshold. Serial-section movies were generated with annotation of the boundaries and identified ScP pores to visualize the output data.

2.3.4.1 Calcified-Uncalcified Thresholding

The datasets were segmented into calcified tissue (bone, calcified cartilage) and uncalcified tissue (articular cartilage, marrow spongiosa) by global thresholding. The threshold was chosen by averaging the individually calculated thresholds for 2-D

sample images from 10 normal sample datasets. For each of these samples, the pixel brightness histogram had two peaks, comprised of calcified pixels (bright) and uncalcified pixels (dark), with the threshold calculated as the midpoint between the two peaks. This threshold (105 on a scale of 0-255 8-bit monochrome) was used for all samples.

2.3.4.2 Tidemark Roughness

With the segmented dataset, the tidemark was identified in 3-D. TM_{ij}, the height of the tidemark (its z-position), was taken to be the height of the first voxel under the cartilage surface where the brightness exceeded the threshold. The indices i and j represent the voxel position in the transverse or x-y plane of the ScP. Within the initially determined tidemark surface, aberrant voxels were identified as those with a height more than 18 μm different from the nearest neighbor voxels and replaced with the nearest acceptable location to create a continuous surface.

Three metrics of tidemark surface roughness where then calculated (TM.RI.plane, TM.RI.quadric, and TM.RI.spline). The metrics were calculated as the deviations from a best-fit plane, quadric, and second order non-uniform rational basis spline, respectively, as

$$TM.RI = \frac{\sum_{i=1}^{M}\sum_{j=1}^{N}\left|TM_{ij} - BS_{ij}\right|}{M \bullet N} \tag{1}$$

where M and N are the dimensions of the analyzed dataset in the x-y or transverse plane, and BS_{ij} is the position of the best-fit surface (plane, quadric or spline) at i and j.

The normalized surface area (TM.nSA) was also calculated, as the surface area of the tidemark divided by 4 mm^2.

2.3.4.3 ScP Thickness

ScP thickness was calculated as the vertical distance between the tidemark and the deep end of the corticalized bone layer, defined as the ScP end boundary (EB), in three ways: (A) a cutoff threshold of bone volume density (texture segmentation, TS), (B) localization of the marrow spongiosa peaks at 0.4 mm intervals in x and y, and and radial basis function interpolation between these to contour the surface (strut search, SS), (C) an analysis of the location of the marrow spongiosa locations and histogram filtering to use the least extreme locations (depth histogram, DH). The SS method was analogous to a 3-D version of the method previously used to determine ScBP thickness in histology [17]. From these three methods, the position of the ScP end boundary, EB_{ij}, was determined, and the thickness was calculated as

$$ScP.TH = \frac{\sum_{i=1}^{M}\sum_{j=1}^{N}(EM_{ij} - TM_{ij})}{M \bullet N} \quad . \tag{2-2}$$

2.3.4.4 ScP Porosity

ScP porosity metrics were determined by thresholding within the ScP and calculating the depth, density, and thickness of the contiguous voxels. The ScP end boundary, EB_{ij}, from the SS method, and TM_{ij} were used to segment the ScP with the trabecular bone and uncalcified cartilage removed. After local thresholding to segment dark voxels within the ScP, a recursive, 6-connected nearest neighbor search on the

selected voxels found was done to group these neighboring dark voxels together into individual pores. Mean radius in the transverse plane *ScP.PO.r* and depth measured perpendicular to the transverse *ScP.PO.D* were calculated from the average cross sectional area, and total superficial-deep length, respectively, of each pore. The metrics of ScP porosity calculated were the number area density, area fraction, and penetration index. The mean pore depth was normalized to the thickness of the tidemark as

$$ScP.PO.nD = \frac{ScP.PO.D}{ScP.TH^{SS}} \qquad . \qquad (2\text{-}3)$$

Number area density of pores was calculated as

$$ScP.PO.AD = \sum_{k=TM^{min}}^{ScP.TH^{SS,max}} \frac{ScP.PO.Number_k}{A_k} \qquad . \qquad (2\text{-}4)$$

ScP.PO.Number$_k$ was the number of pores within the *en face* 2-D slice *k* of the segmented 3-D ScP dataset, and *A* is the mean area of the 2-D slice. The area fraction was defined as

$$ScP.PO.AF = \sum_{k=TM^{min}}^{ScP.TH^{SS,max}} \frac{\pi(ScP.PO.Number_k)(ScP.PO.r_k)^2}{4A_k} \cdot 100\%. \quad (2\text{-}5)$$

This gave the area percentage of the average field of view, or 2-D slice occupied by a pore. The penetration index was defined as

$$ScP.PO.PI = \frac{(ScP.PO.Number^{Vol})(ScP.PO.D)}{(ScP.TH^{SS}) \sum_{k=TM^{min}}^{ScP.TH^{SS,max}} A_k} \qquad . \qquad (2\text{-}6)$$

ScP.PO.Number^{Vol} here was the total sum of all *ScP.PO.Number$_k$* for all *k* within the ScP. The penetration index was the total depth of pores throughout the ScP, on a basis normalized to the ScP volume.

2.3.5 Histological Analysis

For n=3 of the samples analyzed with the μCT morphometric analysis, one for NL, and one for each of the OA grades, a histology section was prepared for comparison with the μCT datasets, to assess visualization of the biological features in each method. The selected samples were fixed in 4% paraformaldehyde, decalcified in 0.1% EDTA, paraffin embedded, and sectioned vertically at 8 μm thickness. Each section was stained with Safranin O-Fast Green and imaged at 40X magnification.

To directly compare the features visualized, a 2-D image slice from the μCT dataset and the histology section were registered, and the features relevant to the metrics in the μCT analysis were co-localized and annotated. Image registration was done manually by matching larger structures, such as bone surfaces and trabecular struts, visible in each image, using the field of view available from the μCT data (6.0 mm x 3.0 mm), and the corresponding zoomed region of the histology section. The tidemarks were contoured in each image and used to confirm correct alignment in the registration. The ScP features in **Table 2.1** were compared between histology and μCT in the registered images, starting with the most superficial features and progressing deeper towards the trabecular bone, to assess the limitations in visualization of the μCT method and correspondence to the quantitative analysis.

For n=1 sample (Grade OA-3), a section was prepared histologically in the same way and also imaged at both $(2 \ \mu m)^3$ and $(9 \ \mu m)^3$/voxel resolution, to assess limitations of the $(9 \ \mu m)^3$ μCT, and determine the additional biological resolution that $(2 \ \mu m)^3$ μCT provides. A comparison between all three methods was done in the same way, with a matching of specific features from superficial to deep. These features

included the contour of the visible tidemarks, vascular channels of various sizes, and other pores in the calcified cartilage or subchondral bone.

2.4   Results

2.4.1 µCT Morphometric Analysis

The ScP of OA samples exhibited structural differences from the normal samples, associated with the erosion state of the overlying cartilage. Parameters that varied were tidemark roughness, ScP thickness, and ScP porosity. An overall description of the morphological trends with surface deterioration is provided in **Fig. 2.4**, and results are summarized in **Table 2.5**. Movies of representative samples for each grade showing serial sections of the processed µCT images, with yellow labeling for the tidemark, magenta for the ScP boundary, and red for the ScP pores, superimposed on the data were produced. In addition, selected 2-D frames from the movies for Grades 1 to OA-3 are shown in **Fig. 2.5**.

2.4.1.1 Tidemark Roughness

TM.RI (**Table 2.5**) was generally higher in both OA groups than normal. The normal group had average $TM.RI^{plane}$ of 13.7 µm, $TM.RI^{quadric}$ of 10.8 µm, and $TM.RI^{spline}$ of 7.9 µm, and TM.nSA of 1.13. Grade 2 had higher than normal $TM.RI^{quadric}$ (+66%, $p<0.05$), and Grade 3 had higher than normal $TM.RI^{plane}$ (+51%, $p<0.01$). The other TM.RI metrics, in OA Grade 2 and Grade 3, had a similar trend of being higher than normal.

2.4.1.2 ScP Thickness

ScP.TH (**Table 2.5**) was generally higher in OA-Grade 3 than normal. The normal group had average $ScP.TH^{SS}$ of 0.23 mm, $ScP.TH^{DH}$ of 0.31 mm, and

ScP.TH^{TS} of 0.28 mm. Grade 3 had higher than normal ScP.TH^{SS} (+64%, p<0.05) and ScP.TH^{DH} (+53%, p<0.05).

2.4.1.3 ScP Porosity

ScP.PO (**Table 2.5**) was generally lower in OA-Grade 3 group than normal. The normal group had average ScP.PO.AF of 3.87%, ScP.PO.AD of 14.6 mm^{-2}, ScP.PO.nD of 0.24, ScP.PO.PI of 13.7 mm^{-2}, and ScP.PO.r of 28.9 μm. Grade 3 had lower than normal ScP.PO.nD (-33%, p<0.05) and ScP.PO.PI (-34%, p<0.05) and higher than normal ScP.PO.r (+22%, p<0.05).

2.4.2 Identification of μCT Features with Registered Histology

Specific features were identified in the μCT data that corresponded directly to matched biological structures in registered histology images, throughout the ScP, from superficial (tidemark) to deep (ScP end boundary and trabecular bone) (**Fig. 2.6**). In the histology sections, the tidemark was clearly visualized as a metachromatic stain line, corresponding directly to the bright calcification front in the μCT (**Fig. 2.6**). The shape of the tidemark generally matched in shape between histology and μCT and was typically a gently undulating line. In the case of multiple tidemarks in the histology, the μCT tidemark corresponded to the most superficial. Present in the histology, but not resolved in the μCT, was the cement line, a more undulatory interface between calcified cartilage and bone. In histology, vascular channels were circular voids with a ring resembling endothelial lining. These matched to the identified pores in the μCT, which were dark tubes within the calcified tissue. In histology, osteocytes, and corresponding

lacunae, were less than 15 μm in diameter, and were not resolvable by μCT. In histology, the largest marrow spaces, as well as most of the smaller sized spaces down to a diameter of about 100 μm, were circular unstained regions. These matched to the larger uncalcified regions in the μCT.

Between the specific examples chosen of the three grades, differences were observed in the structure of the subchondral bone and calcified cartilage, and the histological features contained within (**Fig. 2.6**). The normal ScP was relatively uniform in thickness at 0.2 – 0.3 mm, with a single and clearly visible tidemark and cement line, and had features indicative of normal subchondral bone. These included a number of small vascular channels, and the presence of a single, gently undulating non-duplicated tidemark, and no cartilaginous deposits within the bone. The Grade 2 sample had a more variable and generally thin ScP, with thickness around 0.1 mm in some regions of the cross-section. The tidemark was duplicated and more tortuous than the normal. There were few vascular channels identifiable in the particular section used, but some of those that were seen penetrated to the deeper tidemark. The Grade 3 sample had a more variable and generally thicker ScP than the normal. Although it contained fewer smaller pores than the normal, there were several vascular channels that protruded to near the depth level of the cement line and tidemark, which distinguished it from the normal, where channels were clearly restricted to the subchondral bone layer.

The comparison of $(2\ \mu m)^3$ voxel resolution μCT, $(9\ \mu m)^3$ voxel resolution μCT, and histology in the Grade 3 sample demonstrated that most tidemark and structural features matched between all three methods (**Fig. 2.7**). The superficial-most

tidemark was visible in all three methods, and the $(9 \ \mu m)^3$ was sufficient in capturing the coarse roughness of the tidemark surface. The duplicate, deeper tidemark was only visualized in the histology and not at either μCT resolution. The $(2 \ \mu m)^3$ provided additional detail in the tidemark, and matched the histological visualization strongly, including visualization of some chondrocytes in the calcified cartilage zone. Vascular channels of diameter as low as ~20 μm were visible in both histology and $(2 \ \mu m)^3$ μCT, but not $(9 \ \mu m)^3$ μCT; the latter resolved vascular channels of ~30-40 μm diameter. Large marrow spaces were clearly visible across all three methods.

2.5   Discussion

In this study, analysis of the human ScP, in μCT data and co-localized histology, revealed characteristic structural and biological variations for samples ranging from normal to partially eroded OA. Novel 3-D structural metrics of the ScP, tidemark roughness, ScP thickness, and ScP porosity, were obtained by image processing μCT data. With surface deterioration of the overlying cartilage but not erosion, tidemark roughness was greater than normal. When surface deterioration was accompanied by cartilage erosion, ScP thickness was higher than normal, and porosity was lower. Co-localization of μCT data with histology indicated that the alterations in μCT structural metrics corresponded to biological changes, including tidemark advancement, replication, and penetration by vascular channels as well as subchondral bone sclerosis. These results indicate that such analysis of ScP from high resolution μCT images can delineate and localize certain microstructural features of the calcified cartilage and subchondral bone plate, some of which reflect bone remodeling.

The study design involved tradeoffs in tissue sampling and the scope of the structural analysis. Tissue samples were categorized based on the macroscopic gross appearance of the cartilage. This OA scoring system was similar to others, in grading the state of the overlying cartilage and also considering cartilage thickness [26, 27]. In addition, the morphometric analysis of 9 μm μCT data was conducted for a volume of $(2 \text{ mm})^3$ to minimize the effects of joint curvature. The voxel resolutions of μCT, at $(9 \text{ μm})^3$ and $(2 \text{ μm})^3$, respectively, were in part a trade-off for 3-D dataset size.

The visualization of the ScP with μCT analysis was consistent with previous descriptions of its morphology using histological sections. Compared with prepared

human sections, the thickness of the ScP and the gentle undulation of the tidemark was very similar in the μCT data [1, 13]. Quantification of roughness (normalized surface area) gave nearly identical values between μCT and histology/SEM [15], providing evidence that the detected calcification surface in the μCT was the classical tidemark observed in histology. Finally, the subchondral pores visualized in μCT matched those classically observed with other techniques, and vascular channels could be identified with μCT alone by selecting out the more tubelike pores, which was also verified with co-localized histology. Therefore, μCT was able to image the same delineated ScP region as with histology in 3-D, and presents complementary structural information to conventional high-resolution 2-D analyses, which can help identify mechanisms of progression of OA. Specifically, μCT has the capability to image and sample a much larger volume than 2-D methods when the section thickness in the latter is taken into consideration, and can quantify the number density of the subchondral pores without the need for stereology.

The 3-D metrics of the ScP were consistent with previous findings for adult human normal knee osteochondral tissue. The thickness of the ScP, which represents the sum of the calcified cartilage thickness and subchondral bone plate thickness, generally agreed with findings of other human studies (0.32 mm and 0.47 mm in the femur [18, 28], 0.10-1.0 mm in the patella and tibial plateau [16, 17]). The porosity of human ScP found in this study (2-4%), was comparable in structure to human cortical bone of the femoral midshaft [29] and the ScP of control canine femur [19, 20]. The analysis here is, to the authors' knowledge, the first 3-D quantification of the porosity of the normal adult human ScP, and of its roughness, thickness or porosity with

deterioration and OA. The general trends in deteriorated tissue are comparable to those found in animal OA models with regards to thickness [30], and to a lesser extent porosity [19-21].

The 3-D structural analysis revealed that in progressing grades of OA, the structure of the bone is altered in specific ways that reflect biological and mechanical changes. These variations included roughening of the tidemark with surface of deterioration, elevation in ScP thickness, and decrease in ScP porosity with partial thickness erosion. Tidemark roughening observed in Grade 2 parallels histological observations that as the cartilage undergoes mild deterioration, the tidemark is disrupted, with irregularity in shape, perforations, and occasional vascular penetration [12, 31, 32]. The distribution of the degree of roughening in Grade 2 was non-normal, and possibly indicative of multiple pathways or stages of bone remodeling. The ScP thickening in Grade 3 agreed with classical descriptions of OA-associated bone sclerosis, which may begin occurring when the cartilage is thinned but not yet fully eroded [33]. The thickened, less porous ScP observed in the Grade 3 samples may indicate there is altered transport to the uncalcified cartilage, consistent with observations of transport through the ScP in animal models [18, 34].

The results of the study demonstrate the utility of μCT analyses of both bone and cartilage at multiple scales in 3-D to assess cartilage deterioration and osteoarthritis. The results represent the first quantification in 3-D of the normal human ScP porosity, and of OA ScP porosity, roughness and thickness, and indicate the utility of morphometric parameter analysis to delineate variations in ScP structure. The smaller 3-D volume analysis can be extended to a more macroscopic scale by analyzing

larger volumes composed of multiple contiguous standardized dataset units that were defined in this analysis. The analysis is also extendable to finer scales, through identification of regions of interest and translation of the morphometric analysis to 2 μm or higher resolution μCT.

The ScP is roughened with deterioration of the overlying cartilage and thickened and less porous when the cartilage is partially eroded. The stage-related alterations suggest remodeling at the interface plays a role in the OA mechanism in different ways depending on the current state of the cartilage and bone. The alterations indicate microstructural and histologic indices of the ScP which may predate formation of a full thickness cartilage lesion. The methods demonstrated here are extendable to larger regions by analysis of multiple adjacent units, and are translatable to 3-D data of higher resolution.

2.6   Acknowledgments

Chapter 2, in full, is being prepared for submission to *Bone*. The dissertation author is the primary investigator and thanks co-authors Akshay Maheshwari, Dr. Andrea Pallante-Kichura, Dr. Elaine Chan, Esther Cory, Dr. Tomonori Yamaguchi, Dr. Maripat Corr, Dr. Michele Temple-Wong, Dr. Nozomu Inoue, Dr. William Bugbee, and Dr. Koichi Masuda for their contributions.
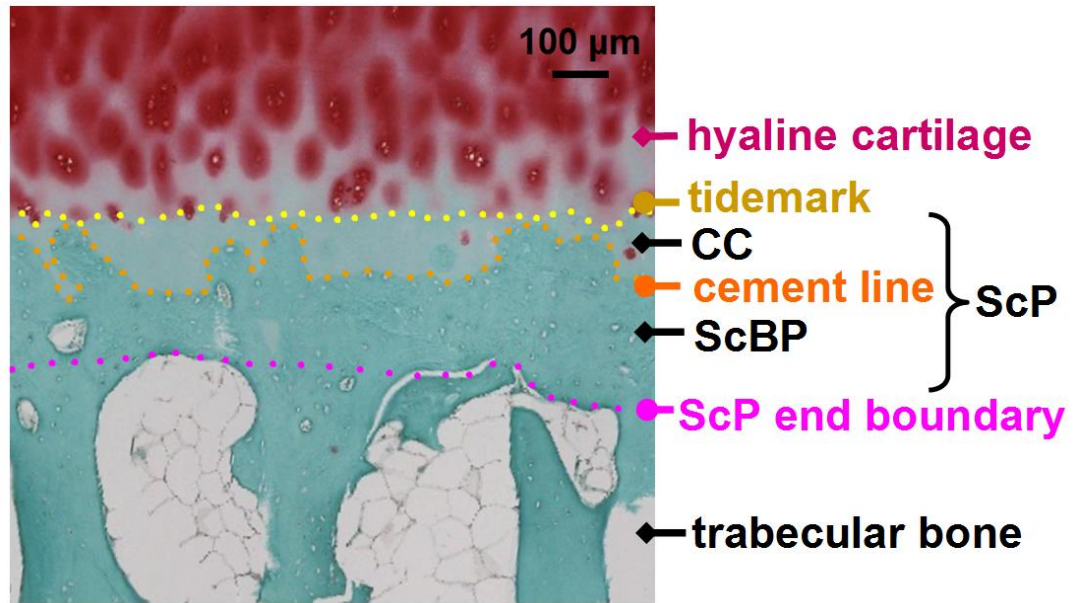
Figure 2.1: The Subchondral plate (ScP) of a Normal Human Osteochondral Unit. A 2-D histology section of the ScP of human medial femoral condyle, stained with Safranin O and Fast Green. The ScP encompasses the calcified cartilage (CC) and the subchondral bone plate (ScBP), and is bordered by the tidemark on the superficial end, and the ScP end boundary on the deep end.
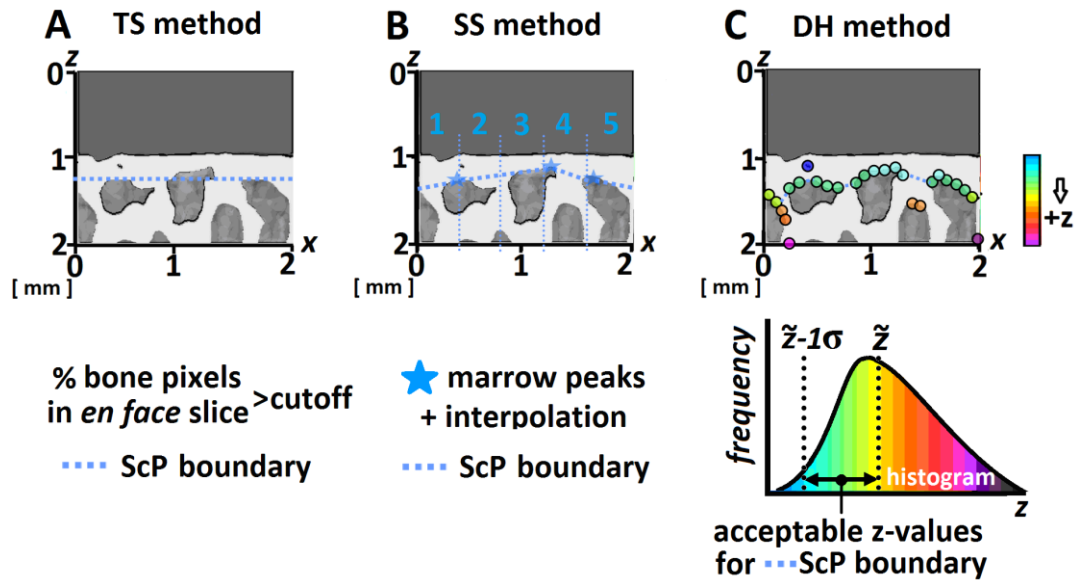
Figure 2.2: Three Methods for Determining the ScP-TB Boundary. (A) Texture Segmentation (TS) method. Bone volume density cutoff value for corticalized bone. (B) Strut Search (SS) method. Localization of marrow spongiosa peaks (local minimum z-values) at 0.4 mm increments of x and y with interpolation between locations (peaks can be shared between increments if the marrow spongiosa volume crosses both). (C) Depth Histogram (DH) method. Localization of marrow spongiosa peaks at each discrete x-y location, with histogram-filtering of z-values, based on standard deviation (σ) from the median ($\tilde{z}$).
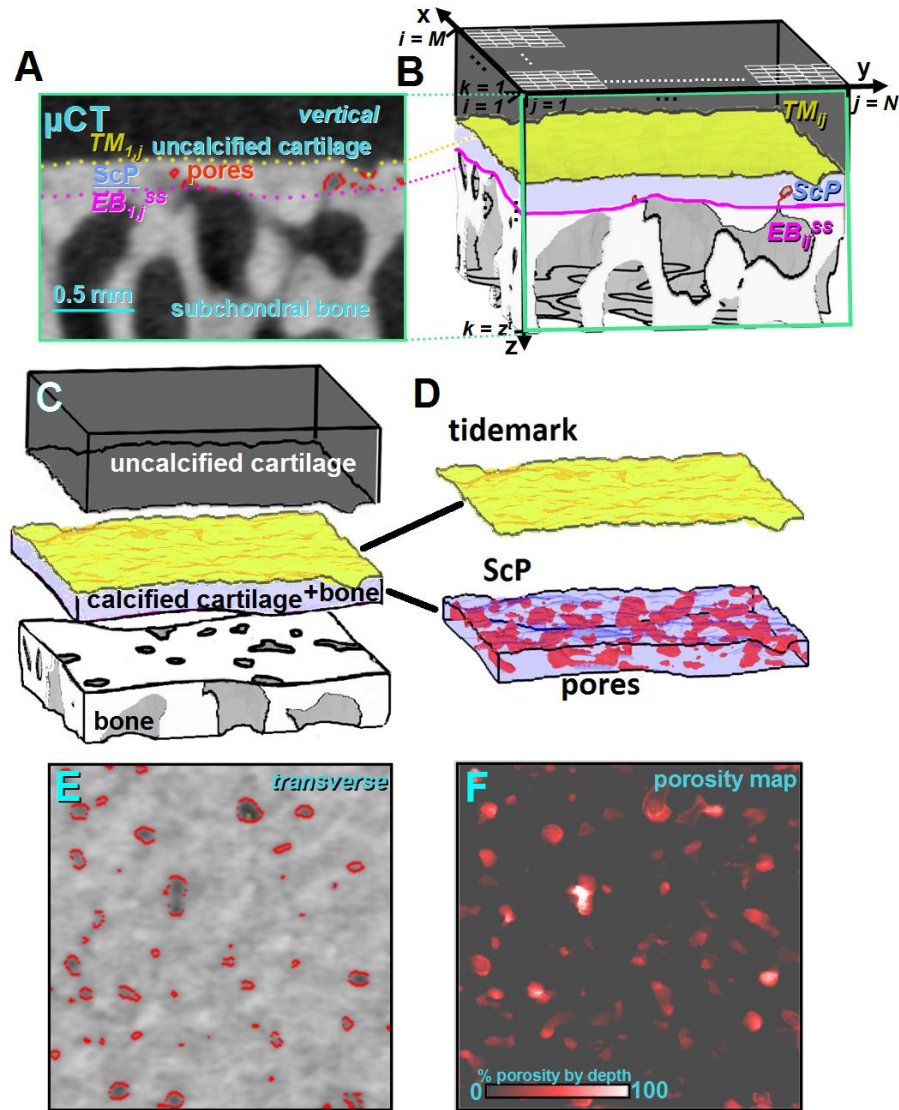
Figure 2.3: Quantitative Analysis of μCT 3-D ScP Data. (A) A vertical 2-D μCT image slice, with overlayed markings of ScP boundaries and pores. (B) With a coordinate system applied to the 3-D boundary, determination of the tidemark (z-positions, TM_{ij}), and end border of bone or ScP end boundary (EB_{ij}) allows (C) segmentation of the ScP. The components of the (D) tidemark, physical thickness of the ScP, and ScP pores are then assessed separately. (E) Transverse μCT view of the ScP, with pores identified by image processing outlined and (F) projection mapped indicating relative depth. Pores are indicated in red. TM and EB are indicated in yellow (A, B, C, D) and purple (A, B), respectively.
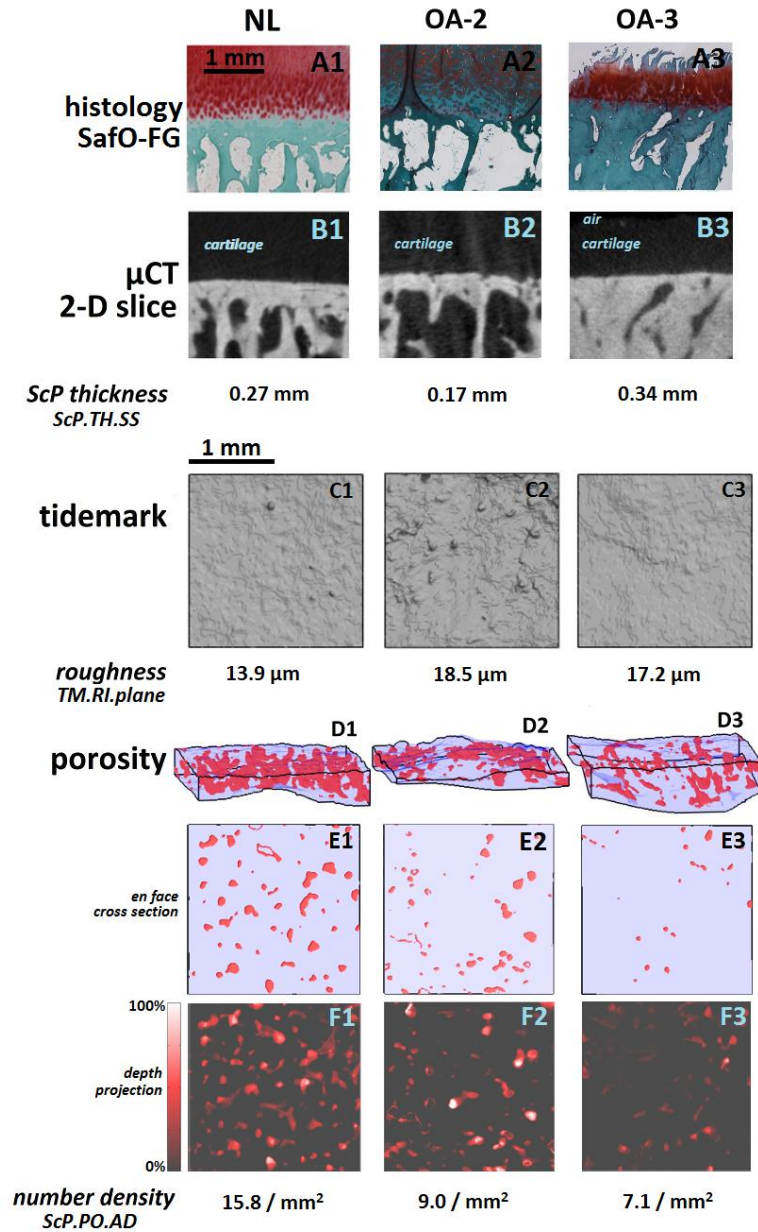
Figure 2.4: Morphological Variations in ScP Associated with Grade. Representative morphologies of ScP, visualized by μCT imaging and analysis with increasing surface deterioration, as evaluated by the grading scale in Table 3. With (A) SafO-FG stained histological sections, (B) μCT 2-D slices, (C) tidemark contours, (D) segmented ScP with pores, (E) cross-section of ScP, (F) heat map of presence of pores throughout entire depth; presented for representative samples of each grade (1-3). The value of the metrics for ScP thickness (SS-method), roughness (RI-plane), and porosity (number density), is reported for each representative sample shown.
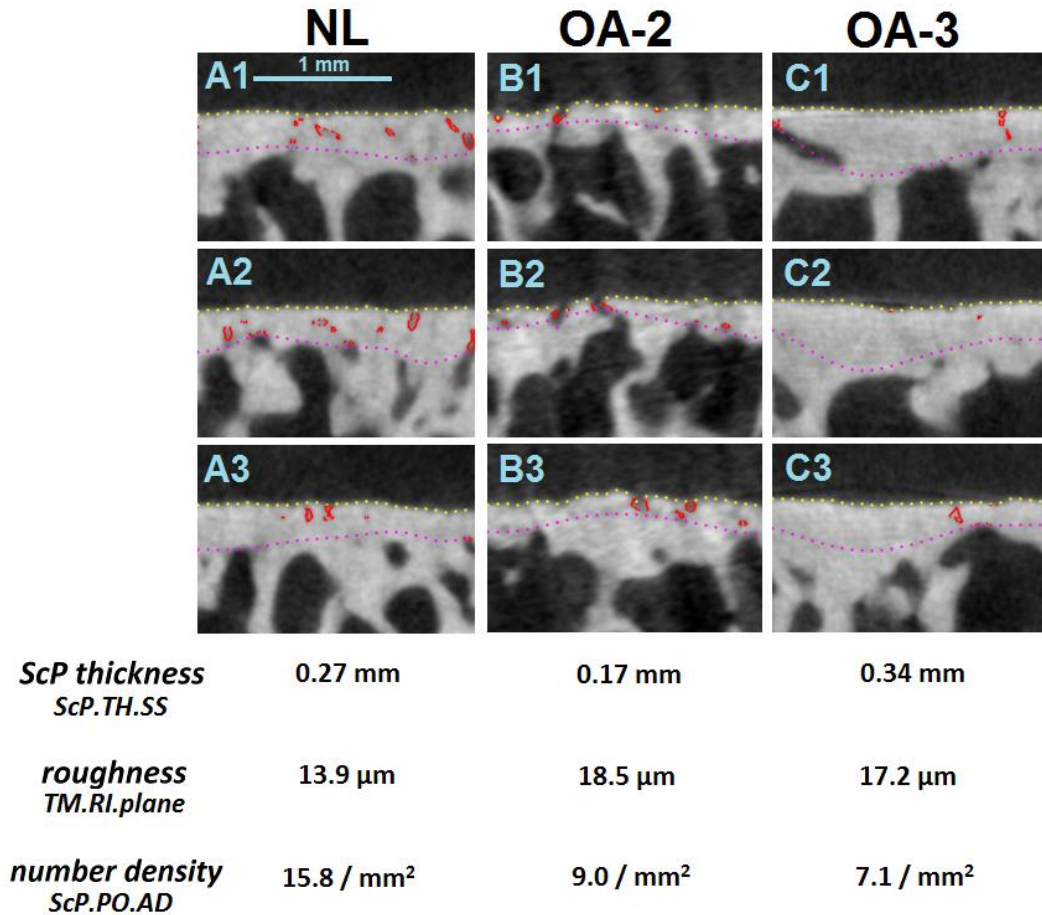
Figure 2.5: Cross-sectional Images of Processed µCT Data. Representative examples of image processed and annotated µCT 2-D slice, for (A) NL, (B) OA-2, (C) OA-3. Yellow dotted line is tidemark, purple dotted line is computed ScP end boundary using strut search method, red outline indicates pores in the ScP. Slices are three frames (1-3), each spaced 0.4 mm apart, from the serial vertical section movies. The values of the metrics for the representative samples is reported below the images.
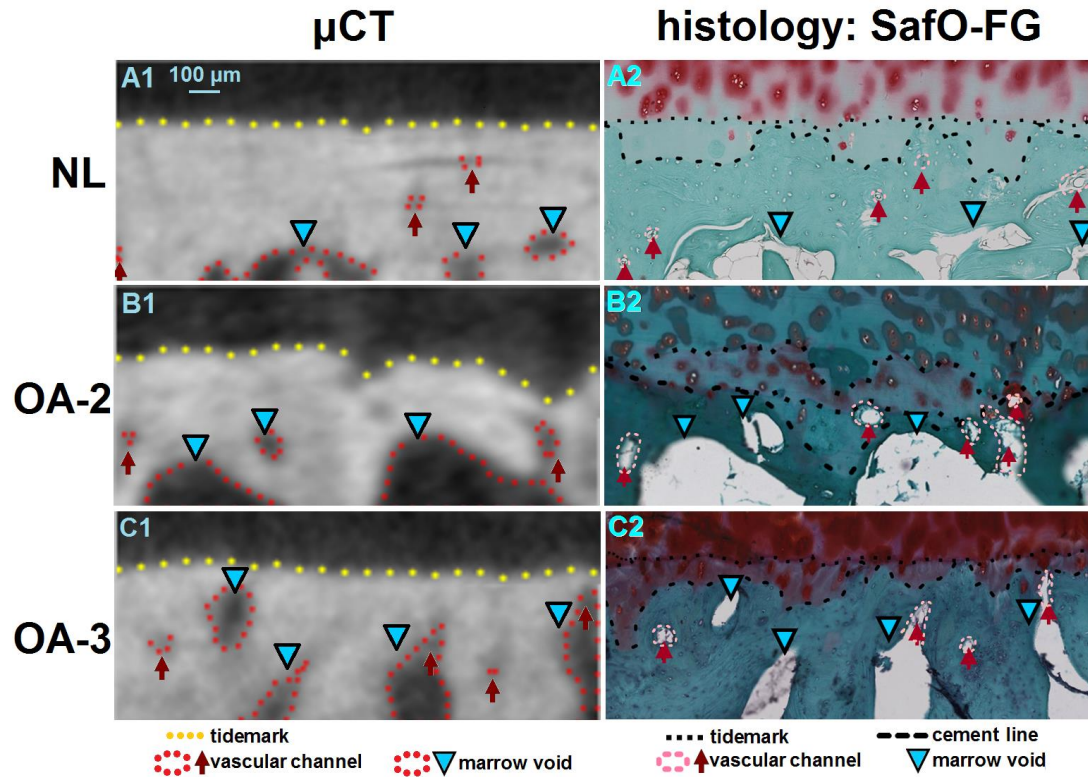
Figure 2.6: Comparison of Registered 2-D µCT and Histology Images. Comparison of the co-localized structural features in representative samples of grades (A) NL, (B) OA-2, (C) OA-3, with (1) µCT slice images registered to (2) SafO-FastGreen sections. Yellow and red dotted lines in µCT are computationally identified tidemark and "pores", respectively. Pores were categorized as either vascular channels or marrow voids based on comparison with the histology.

feature	symbol	2 μm	9 μm	histology
tidemark	• • • • (yellow)	✓	✓	✓
	• • • • (dark red)			✓
chondrocyte	⬇ (green)	✓		✓
vascular channel	⬆1	✓	✓	✓
	⬆2	✓		✓
	⬆3	✓		✓
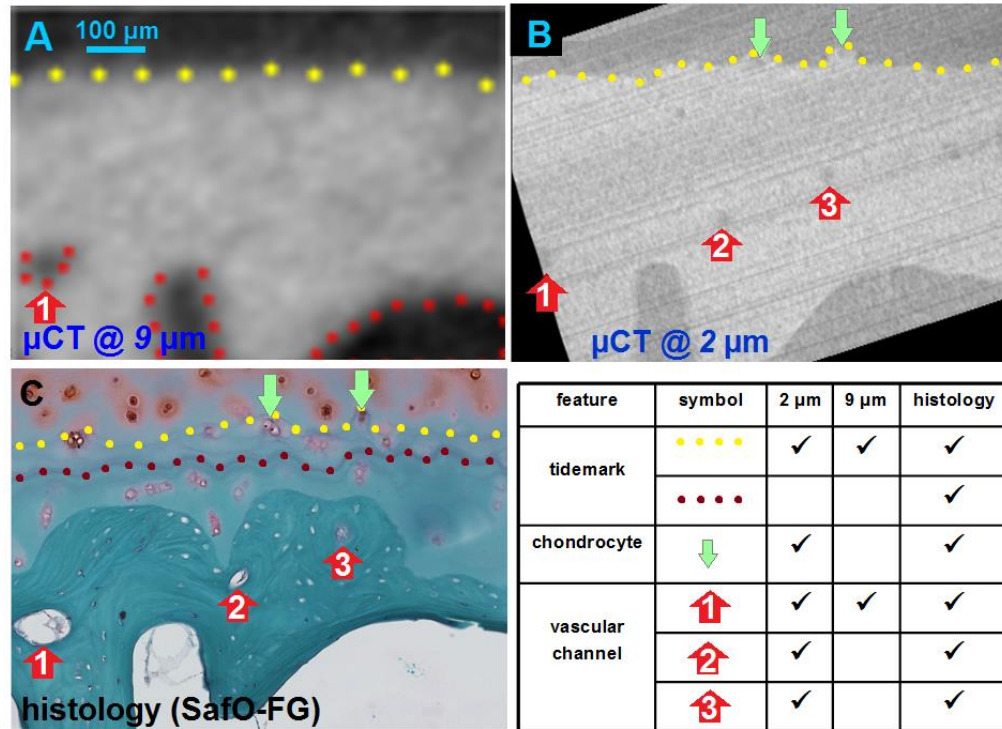
Figure 2.7: Comparison of Registered 2-D μCT, at Multiple Resolutions, and Histology Images, of Grade OA-3 Sample. Comparison of the co-localized features in (A) 9 μm μCT, (B) 2 μm μCT, (C) SafO-Fast Green sections. Inset table: list of features visible with the three methods.

Table 2.1: Glossary of Osteochondral Interface Features, Length Scale and Visualization Methods

Structural Feature	Definition	Length Scale (at distal MFC)	Histology (40X / 0.25 μm)	μCT (9 μm)³ voxel
articular cartilage (AC)	hyaline cartilage covering joint surface	1-3 mm thickness	✓, eosinophilic	✓, low attenuation
calcified cartilage (CC)	mineralized layer of cartilage, beneath hyaline cartilage and superficial to subchondral bone plate [1]	100-200 μm thickness	✓, eosinophilic but less so than AC, area between cement line and tidemark	high attenuation, indistinguishable from ScBP
subchondral bone plate (ScBP)	thin layer of "corticalized" bone, beneath calcified cartilage and superficial to cancellous bone [6, 13]	100-200 μm thickness	✓, eosinophilic, distinguishable from CC by lamellar sheets in matrix	high attenuation, indistinguishable from CC
subchondral plate (ScP)	combined CC and ScBP layers within an osteochondral junction [6, 13]	200-400 μm thickness	✓, CC+ScBP	✓, high attenuation CC+ScBP
tidemark (TM)	interface between uncalcified and calcified cartilage [1, 2]	<10 μm thickness	✓, metachromatically stained line	✓, as boundary between attenuation levels
cement line	interface between subchondral bone and cartilage	<10 μm thickness	✓, dark line	insufficient contrast
osteoclast	bone-resorbing cell	50 - 200 μm diameter XYZ	✓, stained multiple nuclei (multinucleated)	insufficient contrast
osteoblast	bone-forming cell	10 – 20 μm diameter XYZ	✓, stained nuclei (singly nucleated)	~ below resolution, insufficient contrast
osteocyte	bone cells residing within mature bone	10 – 20 μm diameter XYZ	✓, stained nuclei, visible in lacunae in corticalized and trabecular bone	~ below resolution, insufficient contrast
subchondral plate pore (ScP.PO)	any non-calcified void within the ScBP [6, 7]	*may be any of below*		
marrow void	bone marrow pocket within the subchondral bone [6]	50 μm – 1 mm diameter	✓, mostly unstained, contains fat cells	✓, low attenuation
osteoid deposits	undermineralized, immature bone regions	100 – 1 mm diameter	✓, unstained (non-eosinophilic) region, may be accompanied by bone cells	✓, if unmineralized, low attenuation contrast in bone
vascular channel	blood vessel(s) and emveloping bone tissue [3]	30-70 μm diameter 100 μm – 1 mm length	✓, finger-like tube that may be unstained or contain stained endothelial cells	✓, as less attenuated, finger-like tube inside ScP & bone
microcrack	fissure within the calcified cartilage or subchondral bone plate [9, 11]	2-7 μm diameter 25-200 μm length	✓, thin crack in bone matrix or calcified cartilage	below resolution

Table 2.2: Structural Parameters of the Subchondral Plate (ScP). Definitions for metrics of the ScP surface (tidemark) roughness index, thickness, and porosity.

structure	parameter	units	description
tidemark	RI	[μm]	deviation from best fit surface
	nSA	[mm^2 / mm^2]	normalized surface area
ScP	ScP-th	[mm]	subchondral plate thickness
pores	AD	[mm^{-2}]	mean # / *en face* slice area
	AF	[mm^2 / mm^2]	area / ScP area
	nD	[mm / mm]	mean depth / ScP thickness
	PI	[mm / mm^3]	total depth / ScP volume
	r	[μm]	mean radius

Table 2.3: Sample Groups.for ScP Morphometric Analysis

Group	Grade	Surface morphology	Age (mean ± SD)	Sex
NL	1	normal	65 ± 15	6 M, 6 F
OA-2	2	roughened, non-eroded cartilage (>1.5 mm)	70 ± 9	5 M, 5 F
OA-3	3	partially-eroded cartilage (<1.5 mm)	67 ± 9	5 M, 5 F

Table 2.4: Glossary of Variables in ScP Computation Algorithms.

Variable	Definition
i,j,k	integer indices indicating position, in voxel coordinates, in the x and y (transverse) planes, and z (superficial-deep) depth
TM_{ij}	depth value of tidemark at i,j
BS_{ij}	depth value of best-fit surface to tidemark at i,j
EB_{ij}	depth value of ScP end boundary at i,j
M,N	size of the cropped dataset of analysis, in the x,y plane
A	mean area of a 2-D slice of *en face* view of the ScP - if the entire ScP is inside the slice, $A = M \cdot N \cdot R^2$, where R is the resolution of the dataset in μm/voxel - if part of the ScP is outside the given slice, $A = X \cdot M \cdot N \cdot R^2$ where X is the proportion of the ScP that is inside the slice

Table 2.5: Structural Metrics of the ScP. p-value is for *one-way ANOVA, Tukey post-hoc, ‡one-way ANOVA, Tukey post-hoc after reciprocal transform, †Kruskal-Wallis.

Structure	Parameter	Description	ANOVA p-value	NL (n = 12) mean ± SD	OA-2 (n = 10) mean ± SD	p vs. NL	p vs. OA-3	OA-3 (n = 10) mean ± SD	p vs. NL
tidemark (TM)	TM.RI [μm]	roughness index							
	(A) plane	*plane-basis*	<0.05†	13.7 ± 3.3	22.2 ± 12.3	0.17	0.28	20.7 ± 6.3	<0.01
	(B) quadric	*quadric-basis*	<0.05‡	10.8 ± 2.9	17.9 ± 10.2	<0.05	0.99	16.2 ± 7.5	0.07
	(C) spline	*spline-basis*	0.10†	7.9 ± 2.0	12.1 ± 6.4	0.08	0.59	9.5 ± 3.4	0.45
	TM.nSA [mm²/ mm²]	normalized surface area	0.16†	1.13 ± 0.03	1.22 ± 0.12	0.07	0.65	1.16 ± 0.06	0.19
subchondral plate (ScP)	ScP.TH [mm]	thickness							
	(A) TS	*texture segment.*	0.25†	0.26 ± 0.06	0.30 ± 0.14	0.55	0.09	0.32 ± 0.08	0.05
	(B) SS	*strut search*	<0.01†	0.22 ± 0.06	0.20 ± 0.11	0.24	<0.05	0.36 ± 0.15	<0.01
	(C) DH	*depth histogram*	<0.05*	0.30 ± 0.08	0.31 ± 0.14	0.99	<0.05	0.46 ± 0.13	<0.05
subchondral plate pores (ScP.PO)	ScP.PO.AD [mm⁻²]	number area density	<0.05*	14.6 ± 4.8	13.7 ± 5.0	0.88	0.09	9.3 ± 3.5	<0.05
	ScP.PO.AF [%]	area fraction	0.13*	3.87 ± 1.46	2.93 ± 1.17	0.23	0.98	2.83 ± 1.22	0.17
	ScP.PO.nD [mm / mm]	normalized depth	<0.05*	0.24 ± 0.06	0.25 ± 0.09	1.00	<0.05	0.16 ± 0.07	<0.05
	ScP.PO.PI [mm / mm³]	penetration index	<0.05*	13.7 ± 4.1	14.0 ± 4.1	0.97	<0.05	9.1 ± 2.7	<0.05
	ScP.PO.r [μm]	tranverse radius	0.05*	28.9 ± 5.1	25.4 ± 5.1	0.23	<0.05	31.0 ± 4.7	0.60

2.7   References

1.   Oegema T, Jr., Carpenter R, Hofmeister F, Thompson RC, Jr. The interaction of the zone of calcified cartilage and subchondral bone in osteoarthritis. Microsc Res Tech 1997;37: 324-32.

2.   Redler I, Mow VC, Zimny ML, Mansell J. The ultrastructure and biomechanical significance of the tidemark of articular cartilage. Clin Orthop Relat Res 1975;112: 357-362.

3.   Clark JM. The structure of vascular channels in the subchondral plate. J Anat 1990;171: 105-15.

4.   Radin EL, Rose RM. Role of subchondral bone in the initiation and progression of cartilage damage. Clin Orthop Relat Res 1986: 34-40.

5.   Simkin PA. Consider the tidemark. The Journal of rheumatology 2012;39: 890-2.

6.   Clark JM, Huber JD. The structure of the human subchondral plate. J Bone Joint Surg Br 1990;72: 866-73.

7.   Burr DB, Gallant MA. Bone remodelling in osteoarthritis. Nat Rev Rheumatol 2012;8: 665-73.

8.   Findlay DM. Vascular pathology and osteoarthritis. Rheumatology 2007;46: 1763-8.

9.   Mori S, Harruff R, Burr DB. Microcracks in articular calcified cartilage of human femoral heads. Arch Pathol Lab Med 1993;117: 196-198.

10.   Shibakawa A, Yudoh K, Masuko-Hongo K, Kato T, Nishioka K, Nakamura H. The role of subchondral bone resorption pits in osteoarthritis: MMP production by cells derived from bone marrow. Osteoarthritis Cartilage 2005;13: 679-87.

11.   Sokoloff L. Microcracks in the calcified layer of articular cartilage. Arch Pathol Lab Med 1993;117: 191-195.

12.   Oettmeier R, Abendroth K, Oettmeier S. Analyses of the tidemark on human femoral heads. II. Tidemark changes in osteoarthrosis--a histological and histomorphometric study in non-decalcified preparations. Acta Morphol Hung 1989;37: 169-80.

13. Duncan H, Jundt J, Riddle JM, Pitchford W, Christopherson T. The tibial subchondral plate. A scanning electron microscopic study. J Bone Joint Surg Am 1987;69: 1212-20.

14. Thomsen JS, Laib A, Koller B, Prohaska S, Mosekilde L, Gowin W. Stereological measures of trabecular bone structure: comparison of 3D micro computed tomography with 2D histological sections in human proximal tibial bone biopsies. Journal of microscopy 2005;218: 171-9.

15. Wang F, Ying Z, Duan X, Tan H, Yang B, Guo L, Chen G, Dai G, Ma Z, Yang L. Histomorphometric analysis of adult articular calcified cartilage zone. J Struct Biol 2009;168: 359-65.

16. Milz S, Eckstein F, Putz R. The thickness of the subchondral plate and its correlation with the thickness of the uncalcified articular cartilage in the human patella. Anat Embryol (Berl) 1995;192: 437-44.

17. Milz S, Putz R. Quantitative morphology of the subchondral plate of the tibial plateau. J Anat 1994;185 (Pt 1): 103-10.

18. Hwang J, Bae WC, Shieu W, Lewis CW, Bugbee WD, Sah RL. Increased hydraulic conductance of human articular cartilage and subchondral bone plate with progression of osteoarthritis. Arthritis Rheum 2008;58: 3831-42.

19. Intema F, Hazewinkel HA, Gouwens D, Bijlsma JW, Weinans H, Lafeber FP, Mastbergen SC. In early OA, thinning of the subchondral plate is directly related to cartilage damage: results from a canine ACLT-meniscectomy model. Osteoarthritis Cartilage 2010;18: 691-8.

20. Sniekers YH, Intema F, Lafeber FP, van Osch GJ, van Leeuwen JP, Weinans H, Mastbergen SC. A role for subchondral bone changes in the process of osteoarthritis; a micro-CT study of two canine models. BMC musculoskeletal disorders 2008;9: 20.

21. Botter SM, van Osch GJ, Waarsing JH, Day JS, Verhaar JA, Pols HA, van Leeuwen JP, Weinans H. Quantification of subchondral bone changes in a murine osteoarthritis model using micro-CT. Biorheology 2006;43: 379-88.

22. Pan J, Zhou X, Li W, Novotny JE, Doty SB, Wang L. In situ measurement of transport between subchondral bone and articular cartilage. J Orthop Res 2009;27: 1347-52.

23. Rodriguez AG, Rodriguez-Soto AE, Burghardt AJ, Berven S, Majumdar S, Lotz JC. Morphology of the human vertebral endplate. J Orthop Res 2012;30: 280-7.

24. Bae WC, Payanal MM, Chen AC, Hsieh-Bonassera ND, Ballard BL, Lotz MK, Coutts RD, Bugbee WD, Sah RL. Topographic patterns of cartilage lesions in knee osteoarthritis. Cartilage 2010;1: 10-19.

25. Collins DH. The Pathology of Articular and Spinal Disease. London: Arnold; 1949.

26. Yamada K, Healey R, Amiel D, Lotz M, Coutts R. Subchondral bone of the human knee joint in aging and osteoarthritis. Osteoarthritis Cartilage 2002;10: 360-9.

27. Pritzker KP, Gay S, Jimenez SA, Ostergaard K, Pelletier JP, Revell PA, Salter D, van den Berg WB. Osteoarthritis cartilage histopathology: grading and staging. Osteoarthritis Cartilage 2006;14: 13-29.

28. Hunziker EB, Quinn TM, Hauselmann HJ. Quantitative structural organization of normal adult human articular cartilage. Osteoarthritis Cartilage 2002;10: 564-72.

29. Bae WC, Chen PC, Chung CB, Masuda K, D'Lima D, Du J. Quantitative ultrashort echo time (UTE) MRI of human cortical bone: correlation with porosity and biomechanical properties. J Bone Miner Res 2011;27: 848-57.

30. Frisbie DD, Cross MW, McIlwraith CW. A comparative study of articular cartilage thickness in the stifle of animal species used in human pre-clinical studies compared to articular cartilage thickness in the human knee. Vet Comp Orthop Traumatol 2006;19: 142-6.

31. Mastbergen SC, Lafeber FP. Changes in subchondral bone early in the development of osteoarthritis. Arthritis and rheumatism 2011;63: 2561-3.

32. Hargrave-Thomas EJ, Thambyah A, McGlashan SR, Broom ND. The bovine patella as a model of early osteoarthritis. Journal of anatomy 2013;223: 651-64.

33. Hayami T, Pickarski M, Wesolowski GA, McLane J, Bone A, Destefano J, Rodan GA, Duong le T. The role of subchondral bone remodeling in osteoarthritis: reduction of cartilage degeneration and prevention of osteophyte formation by alendronate in the rat anterior cruciate ligament transection model. Arthritis Rheum 2004;50: 1193-206.

34. Pan J, Wang B, Li W, Zhou X, Scherr T, Yang Y, Price C, Wang L. Elevated cross-talk between subchondral bone and cartilage in osteoarthritic joints. Bone 2012;51: 212-7.

CHAPTER 3:

MULTISCALE VARIATION OF THE SUBCHONDRAL PLATE WITH OSTEOARTHRITIC CARTILAGE EROSION

3.1   Abstract

Introduction. In osteoarthritis (OA), localized sites of cartilage erosion are associated with remodeling subchondral bone that is biologically and structurally distinct. The interfacial subchondral plate (ScP) contains entities involved in this remodeling, such as vascular channels, marrow pockets, and microcracks, providing a substrate for bone remodeling cells. Changes in these structures may affect the overall biological functions of hydraulic permeability and diffusivity of cytokines. The aim of the study was to determine the spatial relationship between the structure of the ScP and the fixed charge density of the cartilage, with cartilage erosion, specifically position relative to a lesion.

Methods. Osteochondral fragments were from the anterior medial femoral condyle of remnant tissue from TKA surgery of OA patients with IRB approval. Samples without a full thickness cartilage lesion, "no-lesion" (age 70 ± 7 yrs, mean$\pm$SD, n=6, 3 M/3 F), and with a full thickness lesion, "lesion" (66 ± 9 yrs, n=6, 3 M/3 F) were isolated from $\sim(10 \text{ cm}^2)$ regions. Samples were imaged with and without the contrast agent Hexabrix, at $(9 \text{ μm})^3$/voxel resolution, (Skyscan 1076, Kontich, Belgium). From the scans, (2.6 cm anterior-posterior) x (0.2 cm medial-lateral) regions along the osteochondral surface, covering the proximal boundary of a lesion in the "lesion" group was cropped.

These regions were divided into $(0.2\ \text{cm})^3$ units along the anterior-posterior length, classified into subgroups based on distance from the lesion in the second group, and assessed for parameters of tidemark roughness, ScP thickness, and porosity, and cartilage thickness and FCD. The subgroups were compared for these parameters with repeated measures ANOVA with Bonferroni post-hoc tests.

Results. Tidemark roughness was greatest in locations with overlying cartilage, and more displaced from the lesion, while ScP thickness was highest more proximal to and underneath the lesion. ScP porosity was lowest in the cartilage transition to the lesion and was relatively elevated in the fully eroded regions. Lesion samples had lower cartilage FCD on the areas with cartilage remaining, than no lesion. The transitional region of cartilage, directly proximal to the lesion, had lower FCD than the more distant region, when comparing deep zones only.

Discussion. The ScP varies spatially relative to the location of a full thickness cartilage lesion, with lower tidemark roughness and higher thickness with less displacement from the lesion, and a decrease in porosity only at the transitional zones or lesion boundary. FCD is diminished in cartilage in the same compartment as the lesion. These results are consistent with and extend our previous findings that the hydraulic conductance of human osteochondral tissue is increased with partial and full-thickness osteoarthritic erosion. The diminished fixed charge density in the transitional cartilage regions adjacent to the lesion boundary may mediate load-induced signals that lead to remodeling, and consequently, lower tidemark roughness, higher ScP thickness, and diminished porosity.

3.2   Introduction

In osteoarthritis (OA), the expansion of areas of full-thickness cartilage erosion is associated with symptomatic disease progression. The extent of the erosion of cartilage with this disease has been estimated to be around 3-5% of total volume of cartilage per year based on longitudinal MRI analysis of the knee [1]. This gradual loss, as well as the accompanying narrowing of the joint space, has been associated with joint pain [2, 3] and loss of normal function [2]. Through cohort study analysis of knee osteoarthritis, the risk for the necessity of a total knee arthroplasty surgery has been estimated to increase by 20% for every 1% increase in the rate of cartilage loss [4].

The expansion of OA cartilage lesions may be related to abnormalities in the subchondral plate. The subchondral plate (ScP) is defined here as the composite interface layer of the zone of calcified cartilage (CC), and the subchondral bone plate (ScBP), and contains biological structures which are abnormal and remodel in OA [5-8]. These structures include marrow pockets and vascular channels, which provide the support and surface for the remodeling bone resorption pits [9], and penetrate at greater densities and farther superficially in OA [10]. Microcracks introduced through microdamage of the bone can also develop into the entry points for the resorption pits, and are also more prevalent in OA [11-14]. The locations of these remodeling sites, evidenced by these structures as well as overall structurally distinct subchondral bone, coincide spatially with the erosion of the cartilage [9, 15].

The state of the OA cartilage that is adjacent to areas of full-thickness erosion may contribute to biomechanical abnormalities. The biomechanical support function of

the articular cartilage, with its high fixed charge density in the deep zone allowing interstitial fluid pressurization and low hydraulic conductivity, may be compromised as the cartilage changes. Deterioration of the cartilage-bone unit in partially to fully eroded osteochondral samples greatly increases its hydraulic conductivity [16]. Increased communication or crosstalk between the cartilage and bone may also occur as a result, and this has been demonstrated in murine knees with increased diffusivity of sodium fluorescein past this barrier in experimentally-induced OA [17, 18]. Because of the interdependence of cartilage and bone in osteochondral tissue, alterations in the structure and biology of the ScP may either cause or reflect these changes in the cartilage.

Structural analyses at multiple length scales may help elucidate local changes in cartilage and subchondral bone near full-thickness articular cartilage lesions. Histology can capture large areas and at sub-micron resolutions, but their thin sections result in sampling of only a limited volume of tissue, and requires stereological analysis for deduction of 3-D structures [19]. MicroCT is capable of imaging cartilage and bone at high resolutions, in 3-D, and with a reasonably large field of view [20-23]. This has been demonstrated in the canine hindjoint, with capability of imaging the entire joint in a single scan while resolving the subchondral pores within the joint. [24] The resolution of microCT has been improving incrementally with technological advances, to near or past the micron scale, and towards being capable of imaging the components involved in remodeling, such as the osteoclast fronts, osteoblasts and osteoid deposits, and capillaries that comprise the bone resorption pit, in 3-D. Imaging at this detail level has been demonstrated for quantitative morphometry of the cancellous bone, but not yet

extensively for the subchondral region [25]. Imaging at these resolutions often comes at the sacrifice of a reduced field of view. Therefore, combination of microCT imaging at different resolution and field of view settings can be used to visualize and analyze both the structural changes of the ScP at the macroscale, and the biological components that mediate these changes, in high resolution and in 3-D, at the microscale. In human joints, it has not been described how the ScP changes at the microscale in relation to its macroscale "position" relative to a full thickness lesion. Therefore, the aim of this study was to (1) assess the spatial relationship between a full-thickness cartilage lesion, and ScP structure and articular cartilage (AC) fixed charge density (FCD), and (2) evaluate the use of uCT at 2 μm and 9 μm resolutions, for visualizing biological structures that mediate the remodeling.

3.3   Materials and Methods

3.3.1 Study Design, Sample Preparation

To assess spatial variation in ScP properties, a ~3.0 cm long (anterior-posterior) segment of tissue was taken from the weight bearing region of the center medial femoral condyle of twelve donors. These fragments were taken from remnant tissue of OA patients with IRB approval. These samples were divided into the condyles with no full thickness cartilage lesion in the MFC (the more severe deterioration was in a different compartment of the knee such as the LFC or PFG) (age 70±7 yrs, n=6, 3 M/3 F), or condyles with a full thickness lesion (66±9 yrs, n=6, 3 M/3 F) The latter was chosen so that within the specific 3.0 cm segment, at close to the midpoint going from the anterior to posterior, the full thickness lesion started and continued to the posterior of the segment. That is, the posterior portion of the segment had the full thickness lesion, while the anterior portion was cartilage covered. To extract this segment, a ~$(10 \text{ cm})^2$ surface area region was first isolated from the surgical fragments at the anterior MFC, and then a (3.0 cm) x (0.5 cm) strip was cut out from this region with an osteotome.

3.3.2 μCT Scanning and Data Preparation

Microcomputed tomography (μCT) imaging at $(9 \ \mu m)^3$ resolution, and subsequent image processing, were done to generate standardized 3-D datasets. The samples were scanned in a Skyscan 1076 MicroCT machine (Skyscan, Belgium) at $(9 \ \mu m)^3$ resolution, 70 kVp voltage, with air as the scanning medium, and reconstructed

with NRECON software, with smoothing of the projections using an asymmetrical box filter (Skyscan, Kontich, Belgium). The same calcified-uncalcified grayscale threshold was used as in a prior study with the same scan settings. Sample data was put through an initial crop, rotation, and alignment procedure to produce a (2.6 mm anterior-posterior) x (0.2 cm medial-lateral) x (1.0 cm superficial-deep) dataset prior to the division of the segment into standard units, and the structural analysis.

3.3.3 μCT Image Processing: Standardized $(2 \text{ mm})^3$ Units

The (2.6 mm anterior-posterior) x (0.2 cm medial-lateral) x (~1.0 cm superficial-deep) region was divided into standard $(2 \text{ mm})^3$ units, for which the analysis procedure has been described previously. A computational script input the full volume dataset and used the normal vector to the tidemark, calculated every 2 mm running anterior to posterior across the region, and cropped out a larger (~3 mm) region to compensate for the rotation, rotated the dataset automatically so that the normal vector to the tidemark in that 2 mm segment was redirected to be straight up (aligned the superficial-deep axis), and produced the final crop for the $(2 \text{ mm})^3$ volume centered around the ScP (larger in the superficial-deep axis for the cartilage analysis described in section **3.3.5**).

The standard units assessed were subcategorized within the second sample group ("lesion") for further analysis. These categories were "non-eroded", "transitional cartilage", "transitional bone", and "fully eroded". The transitional categories were defined as within 4 mm of the lesion boundary or point where the lesion started. Thus, there were two each of the "transitional cartilage" and "transitional bone" standard (2

mm)^3 units in each of the lesion samples, with the former being the cartilage covered volume anterior to the lesion boundary and the latter being the exposed bone volume posterior to the lesion boundary. The remaining standard units were assigned to the "non-eroded" (i.e. anterior to the "transitional cartilage" and in the cartilage-covered region) and "fully eroded" (i.e. posterior to the "transitional bone" and in the exposed bone region. This division scheme is represented in **Fig. 3.1**.

3.3.4 Structural Analysis

Each of the standard units described in 2.3 (13 per sample) were analyzed for the parameters listed in **Fig. 3.2**, as previously described, using MATLAB (Mathworks, Natick, MA).

3.3.4.1 Calcified-Uncalcified Thresholding

The program thresholded the sample into calcified tissue (bone, calcified cartilage) and uncalcified tissue (articular cartilage, marrow spongiosa), with global thresholding by using a pixel brightness histogram of a 2-D sample image from each dataset. There were two peaks in this histogram, comprised of calcified pixels (bright) and uncalcified pixels (dark), and the threshold was calculated as the midpoint between the two peaks. The threshold used was chosen to be the same as in Chapter 2 with the same scan settings.

3.3.4.2 Tidemark Roughness

Once the threshold was determined, the program traversed every column of voxels along the z-axis, from the surface of cartilage to the trabecular bone, to locate the first voxel where the brightness exceeded the threshold. From this the tidemark was calculated as an array of 3-D coordinates, with corrections to remove discontinuities in the surface. As a measure of roughness the roughness index (RI) was calculated as deviation from a best fit second order non-rational uniform basis spline.

3.3.4.3 ScP Thickness

Subchondral plate (ScP, or the combined ScBP-CC layer) thickness was calculated as the distance between the tidemark and the deep end of the corticalized bone layer, defined as the end boundary, determined using three methods that were described previously. Results from one of the methods, direct localization of the marrow spongiosa peaks and spline interpolation between these to contour the surface, was reported here. The two surfaces, tidemark and end boundary, were used to segment the ScP, with the trabecular bone and uncalcified cartilage removed for the porosity analysis.

3.3.4.4 ScP Porosity

Pores were located using an adaptive local thresholding method to identify the voxels representing voids, or pore voxels, in the subchondral plate. Connecting pore voxels were identified as individual pores. The measures of ScP porosity calculated were the number area density, or the number of pores per area in a mean en face

(horizontal) slice, and area fraction, or percentage of voxels which were pore voxels in a mean en face slice, as described previously.

3.3.5 Cartilage Hexabrix Analysis

The osteochondral segments were assessed for proteoglycan content of the cartilage using a second Hexabrix-contrasted µCT scan. After the initial µCT scan and analysis of the ScP, the tissue was fixed in 4% paraformaldehyde in phosphate-buffered saline (PBS) for 48h, followed by equilibration for 96h in 20% Hexabrix in PBS. The tissue segments were then scanned again using the exact same settings, and registered to the non-Hex datasets using the same image cropping and rotating procedure, to ensure the assessment was on precisely the same region of tissue. As in the first analysis, the (2.6 cm) x (0.2 cm) x (1.0 cm) region was divided into 13 standard units, which were on the anterior-posterior basis, at identical locations to those in the first analysis. These units were cropped to be longer in the superficial-deep axis, or (2.0 mm) x (2.0 mm) x (thickness of the cartilage + 1.0 mm), to ensure that the entire cartilage thickness was captured in these units. The uncalcified cartilage region of each unit was identified, and the Hexabrix attenuation determined based on the greyscale brightness using a scale of 0-20%, with the grayscale calibrated to 0, 5, 10, 15 and 20% Hexabrix in PBS phantoms which were included in the scan. FCD score was computed as 20 - % Hexabrix attenuation, as Hexabrix equilibrates inversely to the FCD in the tissue. The FCD was calculated on the basis of full cartilage thickness, as well as only the deepest 0.25 mm of the cartilage or only within 0.25 mm from the tidemark, in all of the standard units, except for in those which had no cartilage, or the "transitional

bone" and "fully eroded" units in the lesion group. In the same analysis, the cartilage thickness was also computed as the average distance between the cartilage surface and the tidemark for each of the standard units.

3.3.6 Statistics

ScP and cartilage parameters were analyzed on the basis of the described subgrouping based on distance from the lesion boundary into the "non-eroded", "transitional cartilage", "transitional bone", and "fully eroded", for the n=6 samples in the "lesion" group , as well as with the additional "no lesion" group for the n=6 samples with no full thickness erosion. Because the four subgroupings in the lesion group were all done on the same sample for each of the n=6 samples, this was treated as a repeated measure. Thus, a repeated measures ANOVA was used, pairwise between all the subgroups mentioned, with fixed factor of site and random effect of donor, with Bonferroni post-hoc tests to determine statistical significance at a level of p = 0.05.

3.4   Results

The ScP and cartilage metrics showed distinct differences based on proximity to the full thickness lesions. The metrics for the five subgroups are reported in **Table 3.1**. Results were also compared against metrics for normal tissue that were previously reported.

3.4.1 Tidemark Roughness

The ScP roughness was elevated with more displacement from the full thickness osteochondral lesion. The roughness index was 13.9, 10.0, 9.9. 7.6, 7.3 μm for no lesion, non-eroded, transitional cartilage, transitional bone, and fully eroded groups, respectively. For comparison, roughness index in normal tissue was reported as 7.9 μm in Chapter 2.

3.4.2 ScP Thickness

The ScP thickness was elevated with proximity from the full thickness osteochondral lesion. The thickness was 0.21, 0.23, 0.32, 0.35, 0.48 mm for no lesion, non-eroded, transitional cartilage, transitional bone, and fully eroded groups, respectively. For comparison, ScP thickness in normal tissue was reported as 0.22 mm using the same measurement method on a standard unit.

3.4.3 ScP Porosity

The ScP porosity was found to be diminished in the transitional cartilage near a lesion, and was higher in both the fully eroded areas or regions that were cartilage

covered but father from the lesion. However, all groups had lowered porosity compared to the previously reported normal. By pore number density, the porosity was 13.4, 10.0, 9.4, 10.6, 11.5 # / mm^2 for the no lesion, non-eroded, transitional cartilage, transitional bone, and fully eroded groups, respectively, and 14.6 in previously reported normal. By area fraction, the porosity was 3.19, 2.96, 3.04, 3.28, 3.40 % for the no lesion, non-eroded, transitional cartilage, transitional bone, and fully eroded groups, respectively, and 3.87 % in the previously reported normal.

3.4.4 Cartilage Thickness and FCD

The cartilage thickness and FCD were diminished based on proximity to the lesion. Cartilage thickness was 2.4, 1.4, 0.5 mm for the no lesion, non-eroded, transitional cartilage groups respectively. Lesion samples had a lower FCD than non-lesion samples on average, with the transitional cartilage in lesion samples being the lowest. The full thickness FCD, on a scale of 0-20, was 9.9, 8.4, 7.8 for the three groups respectively. The deep zone FCD, or FCD only computed within 0.25 mm of the tidemark, was 10.0, 9.0, 7.7, respectively.

3.5   Discussion

The subchondral plate varied spatially relative to location of a full thickness cartilage lesion, pointing to its mechanistic role in the spatiotemporal progression of the disease. With increasing proximity to the lesion, counting the "no lesion" group as the farthest (i.e. a full compartment displaced from the lesion), the tidemark roughness decreased, and the ScP plate thickness increased, while the porosity had a more complex relationship to the lesion boundary. The increase in plate thickness was consistent with classical observations of the transition to moderate to more severe OA, with the plate becoming sclerotic and eburnated as the overlying layer of cartilage is gradually eroded away. The highest roughness was found in OA regions more displaced from a lesion, and the no lesion, non-eroded, and transitional cartilage groups all had roughness above normal. This may indicate that features such as penetrating vascular channels, and tidemark disruptions, classically described in early OA, may be more active in cartilage covered regions, and then become less active as the disease progresses and the cartilage is eroded. This was also supported by the small decrease in porosity found in the cartilage covered regions just adjacent to the lesion boundary, as the remodeling activity subsides and the "end-stage" effects of the remodeling, or thick, sclerotic bone, take the most weight in the structure. Along with these changes, fixed charge density and thickness of the overlying cartilage were also diminished by proximity to the lesion. Because the remodeling and its effects seen on the tidemark were strongest in cartilage covered regions more displaced from a full thickness erosion temporally (early OA, or below more normal cartilage) and spatially (4 mm+ from the

lesion boundary), these abnormalities may be implicated as a potential mechanistic cause for the overall progression of cartilage degeneration.

The present study builds upon and addresses limitations of prior studies regarding the scale of the analysis. Previously, the ScP metric trends were demonstrated on samples of different grades in the standard $(2 \text{ mm})^3$ units using the same analysis. However, the main limitation in that study was that only one $(2 \text{ mm})^3$ was used per donor, potentially adding a confounding factor of spatial variation. Here, this was addressed by assessing 13 of the standard units per sample, consecutively in the anterior-posterior direction, where the variation is expected to be greatest due to the gradual transition from more weight-bearing to less weight-bearing regions. In addition to site-specific variation, the variation by status of the overlying cartilage was also studied by using samples which had a full thickness cartilage lesion, but only on the posterior half of the sample. The main limitation in this study was that only two groups were used, "no lesion" and "lesion", with the latter group containing the phenotypic characteristics of fibrillated, partially eroded, and fully eroded all on the same study. As shown in the prior study, the ScP metrics in deteriorated samples have high variability that is sometimes non-normally distributed. However, the main aim of the present study was to establish ScP alterations based on the spatial relationship to a full thickness lesion, to evaluate possible mechanistic reasons for the propagation of the lesion and progression of cartilage erosion. By using the second group described here, this was able to effectively accomplish this with a smaller sample set.

The 3-D metrics of the ScP here by proximity to the lesion were analogous to the previous findings for adult human OA tissue, and confirmed histological

observations from other studies linking mild deterioration of the cartilage to ScP alterations. The metrics reported in the no lesion, non-eroded and transitional cartilage groups here were similar to that for mild degeneration or Grade 2, in Chapter 2, suggesting that the spatiotemporal analysis used was a good analogy to mild to moderate OA, depending on the location sampled relative to the lesion boundary. The tidemark roughening observed here, in the no lesion, non-eroded and transitional cartilage groups relative to the normal samples, parallels the histological observation that as cartilage undergoes mild deterioration prior to being eroded, the tidemark is disrupted, with irregularity in shape, perforations, and vascular penetration. However, the roughening as well as porosity subsides in the transitional cartilage to the transitional bone region, suggesting that this effect that was observed is strongest in mild deterioration and goes away as disease progresses. The thickened and smooth ScP in the fully eroded region agreed with classical descriptions of OA-associated bone sclerosis.

This study is the first to describe how subchondral bone varies spatially relative to the location of a full thickness cartilage lesion, and points of specific mechanisms of subchondral bone remodeling in the development and growth of the lesion. The diminishing FCD in the deteriorated cartilage, especially the deep cartilage in proximity to the FCD, suggests that alterations in the structure of the ScP and the influence of this on crosstalk and cytokines communicating between the tissues, may have an effect on cartilage content and homeostasis. Altered crosstalk and permeability between the cartilage and ScP has been observed in both human [16] and animal [17] models. Alternatively or perhaps in synchrony, the diminished FCD in the transitional cartilage

regions adjacent to the lesion boundary may mediate load-induced signals that lead to remodeling, and consequently, the alterations in the ScP of lower tidemark roughness, higher thickness, and diminished porosity. Determination of which alteration, the decreasing FCD of the cartilage or the abnormality in the structure of the ScP, causes the other, or if both feedback each other in a vicious circle, is a target area for future analyses which will look deeper in the biological alterations of the bone and cartilage at multiple scales.
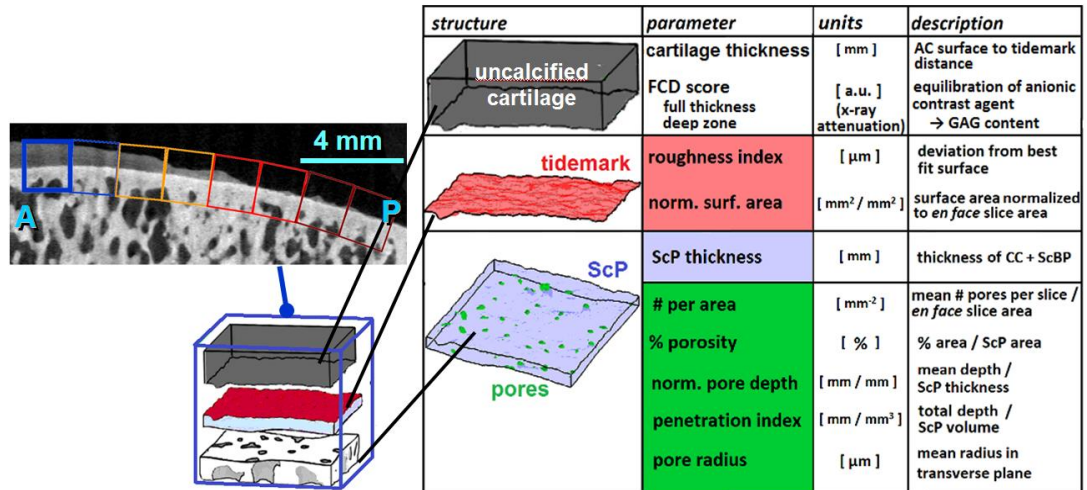
3.6   Acknowledgments

Chapter 3 is being prepared for submission to *Osteoarthritis and Cartilage*. The dissertation author is the primary investigator and thanks co-authors Akshay Maheshwari, Dr. Albert Chen, Esther Cory, and Dr. William Bugbee.

Group	Description	grade	gender	age
1	OA knee, MFC no FT lesion	2	3M / 3F	70 ± 7
2	OA knee, MFC FT lesion	3-4	3M / 3F	71 ± 10
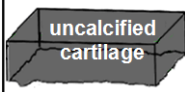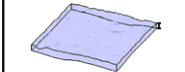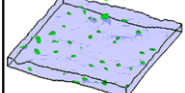
Figure 3.1: Sample Groups and Division Scheme. Medial femoral condyle fragments were from OA patients, with (1) n=6 with no lesion in the condyle (lesion present in lateral femoral condyle or patellofemoral groove), (2) n=6 with a full thickness lesion within the condyle towards the posterior end. The ScP data from each data was divided into $(0.2 \text{ cm})^3$ units and assigned to a subgroup based on distance from the lesion. For Group 1 samples, all were in the same subgroup (A) no lesion. For Group 2 samples, they were divided into (B) distant cartilage, or cartilage covered regions >4 mm from lesion boundary (green line), (C) transitional cartilage, <4 mm from lesion boundary, (D) transitional bone, bone exposed regions <4 mm from lesion boundary, (D) fully eroded, bone exposed regions >4 mm from lesion boundary. Lesion boundary was defined as the border between cartilage covered and bone exposed area.

structure	parameter	units	description
uncalcified cartilage	cartilage thickness	[mm]	AC surface to tidemark distance
	FCD score full thickness deep zone	[a.u.] (x-ray attenuation)	equilibration of anionic contrast agent → GAG content
tidemark	roughness index	[µm]	deviation from best fit surface
	norm. surf. area	[mm² / mm²]	surface area normalized to *en face* slice area
ScP	ScP thickness	[mm]	thickness of CC + ScBP
	# per area	[mm⁻²]	mean # pores per slice / *en face* slice area
	% porosity	[%]	% area / ScP area
	norm. pore depth	[mm / mm]	mean depth / ScP thickness
	penetration index	[mm / mm³]	total depth / ScP volume
	pore radius	[µm]	mean radius in transverse plane

Figure 3.2: ScP Metrics. Each of the units, assigned to a subgroup as defined in Figure 1, was assessed for ScP metrics, computed as described in Chapter 2, as well as cartilage metrics. The uncalcified cartilage was assessed for cartilage thickness as well as FCD score based on attenuation, using the full thickness cartilage and deep zone only (within 250 µm of tidemark. The ScP was assessed for roughness, thickness and oporosity.

Table 3.1: Variation in AC and ScP Biochemistry and Structure by Distance from Full Thickness Lesion. The metrics, reported by mean for subgroup categorization based on distance from lesion are reported. For each sample, the mean for the units that are in each subcategory (A-E) is computed first. The mean between samples is then computed, taking the reported value for each sample for the applicable (A-E) separately. The values are reported as mean±SEM. Letters indicate $p < 0.05$ vs. another group. a: vs. normal from Aim 1 (retrospective t-test), b: vs. no lesion using rmANOVA with Bonferroni tests. c: vs. no lesion using rmANOVA with Bonferroni tests. Normal metrics for AC thickness and FCD are shown for comparison, but were not statistically compared.

lesion boundary   [mm]
-8 ←——— -4 ———— 0 ———— +4 ———→ +8

STRUCTURE	PARAMETER	normal	(A) no lesion	(B) dist. cartilage	(C) trans. cartilage	(D) trans. bone	(E) fully eroded
uncalcified cartilage	AC thickness [mm]	2.5 ±0.7	2.4 ±0.1	1.4[b] ±0.3	0.5[b,c] ±0.1	*no cartilage*	
	AC FCD (full) [a.u.]	12.7 ±1.5	9.9 ±1.0	8.4 ±0.6	7.8[b] ±0.6	*no cartilage*	
	AC FCD (deep) [a.u.]	*no measure*	10.0 ±0.6	9.0 ±0.8	7.7[b] ±0.6	*no cartilage*	
tidemark	roughness index [µm]	7.9 ±0.6	13.9[a] ±2.8	10.0[a] ±1.8	9.9[a] ±2.3	7.6[b] ±1.1	7.3 ±2.9
ScP thickness	ScP thickness [mm]	0.22 ±0.02	0.21 ±0.02	0.23 ±0.04	0.32[a,b] ±0.04	0.35 ±0.12	0.48 ±0.19
pores	ScP Pore Number Density [# / mm²]	14.6 ±1.4	13.4 ±2.1	10.0[a] ±1.2	9.4[a] ±2.1	10.6 ±2.7	11.5 ±3.1
	ScP Pore Area Fraction [%]	3.87 ±0.42	3.19 ±0.35	2.96 ±0.19	3.04[a] ±0.48	3.28 ±0.53	3.40 ±0.43

3.7 References

1.   Wluka AE, Ding C, Jones G, Cicuttini FM. The clinical correlates of articular cartilage defects in symptomatic knee osteoarthritis: a prospective study. Rheumatology (Oxford) 2005;44: 1311-6.

2.   Barker K, Lamb SE, Toye F, Jackson S, Barrington S. Association between radiographic joint space narrowing, function, pain and muscle power in severe osteoarthritis of the knee. Clinical rehabilitation 2004;18: 793-800.

3.   Eckstein F, Wirth W. Quantitative cartilage imaging in knee osteoarthritis. Arthritis 2011;2011: 475684.

4.   Cicuttini FM, Jones G, Forbes A, Wluka AE. Rate of cartilage loss at two years predicts subsequent total knee arthroplasty: a prospective study. Annals of the rheumatic diseases 2004;63: 1124-7.

5.   Burr DB, Gallant MA. Bone remodelling in osteoarthritis. Nat Rev Rheumatol 2012;8: 665-73.

6.   Clark JM. The structure of vascular channels in the subchondral plate. J Anat 1990;171: 105-15.

7.   Clark JM, Huber JD. The structure of the human subchondral plate. J Bone Joint Surg Br 1990;72: 866-73.

8.   Oegema TR, Jr., Carpenter RJ, Hofmeister F, Thompson RC, Jr. The interaction of the zone of calcified cartilage and subchondral bone in osteoarthritis. Microsc Res Tech 1997;37: 324-32.

9.   Shibakawa A, Yudoh K, Masuko-Hongo K, Kato T, Nishioka K, Nakamura H. The role of subchondral bone resorption pits in osteoarthritis: MMP production by cells derived from bone marrow. Osteoarthritis Cartilage 2005;13: 679-87.

10. Oettmeier R, Abendroth K, Oettmeier S. Analyses of the tidemark on human femoral heads. II. Tidemark changes in osteoarthrosis--a histological and histomorphometric study in non-decalcified preparations. Acta Morphol Hung 1989;37: 169-80.

11. Mori S, Harruff R, Burr DB. Microcracks in articular calcified cartilage of human femoral heads. Arch Pathol Lab Med 1993;117: 196-198.

12. Sokoloff L. Microcracks in the calcified layer of articular cartilage. Arch Pathol Lab Med 1993;117: 191-195.

13.   Lane LB, Villacin A, Bullough PG. The vascularity and remodelling of subchondrial bone and calcified cartilage in adult human femoral and humeral heads. An age- and stress- related phenomenon. J Bone Joint Surg Br 1977;59: 272-8.

14.   Smith DW, Gardiner BS, Dunstan C. Bone Balance within a Cortical BMU: Local Controls of Bone Resorption and Formation. PloS one 2012;7.

15.   Neogi T, Felson D, Niu J, Lynch J, Nevitt M, Guermazi A, Roemer F, Lewis CE, Wallace B, Zhang Y. Cartilage loss occurs in the same subregions as subchondral bone attrition: a within-knee subregion-matched approach from the Multicenter Osteoarthritis Study. Arthritis and rheumatism 2009;61: 1539-44.

16.   Hwang J, Bae WC, Shieu W, Lewis CW, Bugbee WD, Sah RL. Increased hydraulic conductance of human articular cartilage and subchondral bone plate with progression of osteoarthritis. Arthritis Rheum 2008;58: 3831-42.

17.   Pan J, Wang B, Li W, Zhou X, Scherr T, Yang Y, Price C, Wang L. Elevated cross-talk between subchondral bone and cartilage in osteoarthritic joints. Bone 2012;51: 212-7.

18.   Weng LH, Ko JY, Wang CJ, Sun YC, Wang FS. Dkk-1 promotes angiogenic responses and cartilage matrix proteinase secretion in synovial fibroblasts from osteoarthritic joints. Arthritis Rheum 2012;64: 3267-77.

19.   Thomsen JS, Laib A, Koller B, Prohaska S, Mosekilde L, Gowin W. Stereological measures of trabecular bone structure: comparison of 3D micro computed tomography with 2D histological sections in human proximal tibial bone biopsies. Journal of microscopy 2005;218: 171-9.

20.   Rodriguez AG, Rodriguez-Soto AE, Burghardt AJ, Berven S, Majumdar S, Lotz JC. Morphology of the human vertebral endplate. J Orthop Res 2012;30: 280-7.

21.   Intema F, Hazewinkel HA, Gouwens D, Bijlsma JW, Weinans H, Lafeber FP, Mastbergen SC. In early OA, thinning of the subchondral plate is directly related to cartilage damage: results from a canine ACLT-meniscectomy model. Osteoarthritis Cartilage 2010;18: 691-8.

22.   Botter SM, van Osch GJ, Waarsing JH, Day JS, Verhaar JA, Pols HA, van Leeuwen JP, Weinans H. Quantification of subchondral bone changes in a murine osteoarthritis model using micro-CT. Biorheology 2006;43: 379-88.

23.   Bobinac D, Spanjol J, Zoricic S, Maric I. Changes in articular cartilage and subchondral bone histomorphometry in osteoarthritic knee joints in humans. Bone 2003;32: 284-90.

24. Sniekers YH, Intema F, Lafeber FP, van Osch GJ, van Leeuwen JP, Weinans H, Mastbergen SC. A role for subchondral bone changes in the process of osteoarthritis; a micro-CT study of two canine models. BMC Musculoskelet Disord 2008;9: 20.

25. Peyrin F, Salome M, Cloetens P, Laval-Jeantet AM, Ritman E, Ruegsegger P. Micro-CT examinations of trabecular bone samples at different resolutions: 14, 7 and 2 micron level. Technology and health care : official journal of the European Society for Engineering and Medicine 1998;6: 391-401

CHAPTER 4:

ALTERED DENSITY AND 3-D MORPHOLOGY OF HUMAN SUBCHONDRAL PLATE VASCULAR CHANNELS WITH CARTILAGE DEGENERATION

4.1 Abstract

Introduction. The subchondral plate (ScP), comprised the calcified cartilage and subchondral bone plate, is a site of active remodeling in osteoarthritis (OA). This remodeling involves the active infiltration of basic multicellular units (BMUs), consisting of an osteoclastic front and a supporting vascular channel. Previous studies have characterized the age-related variations in ScP of the human femoral head. The aim of the present study was to analyze the ScP for relative frequencies of vascular channels and tidemark features, in histology on the scale of ~10 mm length in human MFC samples exhibiting different degrees of cartilage degeneration.

Methods. Thirty sections, each from human medial femoral condyle donors (15 M / 15 F) were obtained from tissue banks with six from each grade of degeneration, (1Y) normal young (20-40 yo), (1O) normal middle-old (40+ yo), (2) mild fibrillation, (3) partial erosion, (4) full thickness erosion. A ~10 mm wedge representative of the grade was fixed, paraffin embedded, sectioned at 5 μm, stained with Safranin O-Fast Green,

and imaged. This image was divided into eight 1.2 mm x 0.9 mm aligned and centered segments running across the tidemark. The segments were annotated for: (1) tidemark number and discontinuities, (2) vascular channels that penetrated the (a) cement line (CL) or (b) tidemark (TM), and were (i) active, based on the presence of a supported BMU, or (ii) inactive. Data is reported as mean±SD and compared by ANOVA with post-hoc Tukey test.

Results. The feature densities are summarized in **Table 1**, and representative segments shown in **Figure 1**. Tidemark number and discontinuities were higher going from Grade 1 to 3, with an average of 1.2 tidemarks in Grade 1 samples to an average of 2.7 and 2.5 tidemarks in Grades 2-3, respectively. The number of active vascular channels was higher in Grades 2-4 (11.1, 12.0, 13.0 # / 10 mm, respectively) than in Grade 1 (# 8.1 / 10 mm). The number of channels penetrating the cement line and tidemark in Grades 2-3 (4.1 CL, 8.5 TM Grade 2), (4.8 CL, 2.8 TM Grade 3) was higher than Grade 1 (5.5 CL, 0.8 TM), # / 10 mm.

Discussion. An increase in the number of tidemarks, discontinuities and penetrating/active vascular channels occurs in early degeneration stages (mild fibrillation, partial erosion) leading up to OA. This suggests that vascular changes and subchondral plate remodeling precedes full erosion of the articular cartilage.

4.2   Introduction

In the normal adult synovial articulating joint, the articular cartilage is attached to underlying trabecular bone (TB) by a tangentially continuous subchondral plate (ScP), which is composed of a layer of calcified cartilage and bone [1]. The calcified cartilage (CC) is a is ~100 μm thick mineralized layer containing chondrocytes, immediately deep to the uncalcified cartilage, and the bone layer, also called the subchondral bone plate (ScBP), is a ~300 μm thick of "corticalized" bone [2]. In most histology stains, these layers, and thus the ScP as a whole, can be distinguished clearly by visualizing metachromatic lines that demarcate each layer: the tidemark, which bounds uncalcified and calcified cartilage, and the cement line, which separates the calcified cartilage and subchondral bone [3]. The components of each layer can also be distinguished through most standard histology stains: the bone and specifically the ScBP can be identified due from its collagen content and lamellar organization with collagen stains like Fast Green. The calcified cartilage is unstained using some conventional methods, such as SafO-FG and H&E, and contrasts with surrounding stained tissues; alternatively, it can be contrasted from the non-mineralized cartilage using stains for calcification such as Alcian Blue or Von Kossa staining [4].

The ScP contains occasional vascular channels, which appear in histology as fingerlike projections or extensions of the marrow from the trabecular bone [1, 5]. The channels are typically between 20-100 μm in diameter, with size uniformity varying from sample to sample. These vascular channels can be indicative of active bone remodeling, especially when they are supporting the osteoclastic, bone resorbing, front

and osteoblastic, born forming, tail in a basic multicellular unit [6]. In this case, the vascular channel is sometimes referred to by a different name: basic multicellular unit (BMU), resorption pit or resorption bay [7]. Vascular channels are part of the subchondral pores, a more generic term for any perforation of the ScP, as described by Burr and Clark [5, 8]. These vascular channels include the vessels inside the Haversian canals inside cortical osteons, as well as the Volkmann's canals traversing between osteons. Vascular channels can be closed off with a bony cap, or more rarely open or without a bony cap, and when the latter is combined with capillary fenestration or pores in the endothelial lining of the channel, can potentially communicate with the surrounding tissue [5]. In normal tissue, the vascular channels extend upwards (superficially), but usually terminating prior to the cement line, or occasionally causing the cement line to shift upward in discrete locations as small "bumps".

In age-related degeneration and osteoarthritis, the vascular channels are altered substantially in their size, structure, and location or distance to which they protrude, relative to the landmarks of the ScP like the tidemark or cement line. In terms of size, the vascular channels of a deteriorated or OA plate are much less uniform, which indicates that some of the channels are more actively remodeling as the bone turnover process is altered [7]. In terms of structure and biology, the activity of the vascular channels is also observed to increase by the presence of more active cells, in the interior of the channel (blood cells) as well as near the edges (osteoclasts and osteoblasts of the BMU) [9]. Channels also are seen which have an open cap or are uncapped, in contrast to the normal case where they are almost exclusively capped [7]. The most marked change is that the channels invade to the tidemark in mild OA and degeneration, as

observed by Oettmeier, who noted that in low to middle grades of OA the tidemark was often disrupted by these channels. [10]. This invasion of channels to the tidemark, which is almost exclusive to the abnormal ScP resulting from cartilage degeneration and OA, may have implications for cartilage-bone crosstalk.

Although these changes to the ScP have been observed and described and are now considered a part of the classical changes which occur with OA, they have not been quantified to a great extent. The reason for this lies mainly in the limitations of visualization methods to sample sufficiently large volume of tissue. Standard histology is capable of showing the vascular channels, but is limited in it that only thin tissue sections are sampled and require stereological assessments to draw conclusions about the volume as a whole [11]. Because most vascular channels are oriented superficial-to-deep (vertically), Lane was able to address this by using en face sections to quantify the vascular channels by activity level in the femoral head [9]. However, this analysis still only produced vascular channel quantification on a per area basis rather than by volume. Microcomputed tomography is a potential method that can be used for this purpose, as it can resolve channels with sufficient resolution, and can also sample relatively large volumes [12-14]. However, it is limited in its ability to contrast vascular channels from other subchondral pores which are not channels, as it primarily can only distinguish calcified from non-calcified tissue, and is likely most effective when used in complement to registered histology. In the present study, large (~10 mm) sections are used to assess the linear density of different vascular channels in ScP of different grades in human tissue. Although this approach does not solve the problem of sufficient volume sampling of tissue to perform a volume based quantification of vascular

channels, the current aim is to establish a baseline of the relative frequencies of abnormal-type channels, such as those protruding the tidemark and being more active, in samples exhibiting different degrees of cartilage degeneration. The findings of the present study can be built upon to better establish the needed volume sampling in future analyses to quantify the alterations in these channels in greater detail. The aim of the present study was to analyze the ScP for relative frequencies of vascular channels and tidemark features, in histology on the scale of ~10 mm length in human MFC samples exhibiting different degrees of cartilage degeneration. The hypothesis that age related degeneration of articular cartilage synchronizes with an increase in activity and superficial invasion of the vascular channels in the ScP.

4.3   Materials and Methods

Histology sections were taken from the center medial femoral condyle (MFC), which were extracted as slabs using an autopsy saw from thirty donor knee blocks. Each center MFC slab was given three grades in the anterior, center, posterior, reflecting the worst deterioration level within that third of a slab, from normal to full thickness erosion. For the slabs as a whole, n=6 each exhibited one of the specific grades as the worst within the whole condyle, with Grade 1 (no fibrillation) young (age 20-40), Grade 1 middle-old (40+), Grade 2 (mild fibrillation), Grade 3 (partial thickness erosion) and Grade 4 (full thickness erosion). The slab was cut into five wedges on an equal angle basis, anterior to posterior, so that the wedges could each fit on a histology slide and be stitched back later.

Histology sections were prepared from these wedges as previously described. Briefly, the wedges were fixed in paraformaldehyde, decalcified in 10% EDTA in phosphate buffered saline, paraffin embedded and sectioned at a thickness of 5 µm. The sections were stained with Safranin O and Fast Green, and digitally imaged. The digital slide images of the five images represented the entire length of the condyle, but only a selected 10.4 mm long region (anterior-posterior), that was entirely within the third of the condyle that had the worst grade, or the grade that the sample was representative of in the group assignments, was used.

The selected 10.4 mm long region from the histology section was stitched and assembled into presentation format to allow for assessment of quantitative features of the ScP. This region was first digitally stitched, using screen captures taken at 10X, so

that the condyle would be level across several Powerpoint slides showing the ScP at this magnification. If the particular 10.4 mm length ran over between multiple wedges, the edges between the separate sections comprising these wedges were stitched together as well. The screen captures were taken at dimensions of (1280 x 960 pixels) or (1.28 x 0.96 mm at 10X), and they were aligned so that the entire ScP was within the captured region and the tidemark was close to level. Eight of these captures were taken per sample, consecutively running anterior to posterior, to give the total 10.4 mm length. Each of the Powerpoint slides containing the captured image was annotated for the tidemark(s) by tracing over it with a dotted line, with different colors for multiple tidemarks, as well as labeled for vascular channels of the different categories described below.

From the stitched presentation dataset, the ScP features of tidemark number and disruption, and vascular channel linear density were assessed. Within the entire 10.4 mm length, the maximum number of tidemarks seen was recorded. The total number of tidemark disruptions, or discontinuities in the tidemark, was recorded for the length and the linear density computed. The vascular channels were categorized based on activity level and penetration depth. For activity level, vascular channels were active based on (1) being part of a basic multicellular unit, or (2) having many erythrocytes visible inside the channel. A paucity of erythrocytes in the channel gave it the categorization of inactive. For the penetration level, the channel was categorized based on where the superficial tip penetrated to or reached within the given section. If it did not reach the cement line, it was categorized as non-penetrating. If it reached the cement line, in that it either had an open region in the bony cap or a missing cap

altogether, it was categorized as penetrating to the cement line. If it reached a tidemark, or any of the tidemarks if there were multiple, so that there was either clear contact between the channel or the tidemark, or the channel clearly ran superficial to the tidemark, it was categorized as penetrating tidemark. The number of channels for the different categories was normalized to the assessed length to also give this metric in terms of linear density. The linear densities of categorized vascular channels and tidemark disruptions and the number of tidemarks, was compared between groups as well as by sex to check for gender effects, using one-way ANOVA, with Tukey post-hoc tests, and significance level set as $p = 0.05$.

4.4   Results

Vascular channel density and tidemark number and disruptions, were distinct between the grades assessed. The alterations were modest in most of the categorizations used, but there were a few larger differences, particularly relating to how the vascular channels penetrated to and disrupted the tidemark in moderate grades of OA. The vascular channel and tidemark disruption linear densities and mean tidemark numbers are summarized in **Table 4.1**. Representative images of each grade assessed, with an example of every feature categorized shown at least once across all the images, is shown in **Fig. 4.1**. There was an effect of sex found for the density of vascular channels. The linear density of all vascular channels, and channels that were inactive, active, not penetrating, and penetrating to at least the cement line was greater in males compared to females ($p < 0.05$).

In both Grade 1Y and 1O, the tidemark was normal or non-duplicated with few disruptions. The average maximum number of tidemarks visible in the 10.4 mm length was 1.2 and 1.3, and the linear density of tidemark disruptions was 3.6 and 1.1 / 10 mm, for Grades 1Y and 1O respectively. The vascular channel density, reported as total (inactive/active), was 36.8 (20.5/16.3), 34.2 (24.7/7.1) / 10 mm for Grades 1Y and 1O. There were some channels that penetrated to at least the cement line, 9.3 and 4.6 / 10 mm, but few that penetrated to the tidemark, 0.5 and 1.6 / 10 mm for Grades 1Y and 1O.

In contrast, the Grade 2 and Grade 3 samples had disrupted and duplicated tidemarks, and more active channels and more channels which penetrated to the tidemark. For Grade 2, the average maximum number of tidemarks visible was 2.7, the

density of discontinuities 13.2, the vascular channel density 25.1 (11.9/13.2) (total, (inactive/active)), the density of channels penetrating to at least the cement line 9.1, and the density of channels penetrating to the tidemark 4.7 / 10 mm. For Grade 3, the average maximum number of tidemarks visible was 2.5, the density of discontinuities 11.7, the vascular channel density 21.0 (8.3/12.7), the density of channels penetrating to at least the cement line 4.7, and the density of channels penetrating to the tidemark 2.8 / 10 mm. Grade 4 deviated less from normal, with the average maximum number of tidemarks visible 1.5, the density of discontinuities 5.2 the vascular channel density 25.4 (11.1/14.3), the density of channels penetrating to at least the cement line 5.2, and the density of channels penetrating to the tidemark 2.9 / 10 mm.

4.5   Discussion

This study shows that increased remodeling activity of the subchondral bone is linked with the mild grades of OA. The increase in number of tidemarks is a well-known hallmark of osteoarthritis, both in the mid to late stages. However, the increasing tidemark discontinuities, especially those caused by penetrating vascular channels, were found here to increase by grade, even in early degeneration stages leading up to osteoarthritis, such as mild fibrillation (Grade 2) to partial erosion (Grade 3) of the cartilage. The greatest alteration in tidemark discontinuity density was in Grade 2, when the cartilage is mildly fibrillated but shows no erosion, possibly showing that gradual tidemark breakdown may be a good predictor of progressing degeneration of the cartilage. This tidemark disruption increase was associated with an increase in the count of vascular channels that penetrated to at least the tidemark, suggesting that vascular remodeling at the level of the tidemark occurs as early as when the cartilage is mildly fibrillated. The sequence of alterations suggested here may indicate a temporal link between remodeling and vascularization of the bone and exacerbation of cartilage deterioration from fibrillated to eroded.

Although study design and analysis dimensions had limitations in the scale and statistical power, the field of view used here was much larger than most previous 2-D histological assessments and provides a good analog for later studies using microCT or 3-D histology. There was a relatively small sampling of vascular channels (~ 1 channel per 0.3 mm), giving a total count on the order of 25 channels per sample analyzed. The small number of channels counted can be attributed to the small *en face* area of the ScP assessed, 10.4 mm by 0.005 mm, or ~0.05 mm^2. This represented a very small

proportion of the total area of the ScP surface on the 1/3 condylar slab targeted, despite the fact that multiple large, high magnification sections were stitched for the analysis. Despite these limitations, the assessment here represent a step forward in that it expands histological analyses of the osteochondral tissue from one dimension (superficial to deep) to two (anterior to posterior, which is usually limited in non-stitched images). The next step, building upon this analysis, would be to assess the third dimension as well (medial-lateral) using 3-D techniques like microCT or automated 3-D histology. Other limitations of the study design included the chosen stain's ability to detect features of interest, as opposed to a more targeted IHC analysis for markers of the vascular channels. Although SafO-FG is inferior in its ability to detect active vascular channels, it can still provide a good estimation of activity through staining and counting of erythrocytes as well as other possibly visible feature such as osteoblasts/osteoclasts, and is among the best stains for visualizing the tidemark and disruptions within. It was chosen to be a good compromise for its ability to stain and detect differences in both the vascular channels and the tidemark.

The present study linked an alteration in vascular channel activity and tidemark disruption, both previously observed, with mild deterioration of the overlying articular cartilage. Oettmeier observed in the femoral head that the tidemark gradually loses its form and becomes less continuous in mild OA, along with the duplication [10]. Here, this is shown in more quantitative detail, as well as more association between total number of vascular channels by activity and penetration level and the breaks in the tidemark, and in a more relevant weight bearing part of the joint, the MFC. Lane had shown that there was an increase in vascular channels with aging in older samples in the
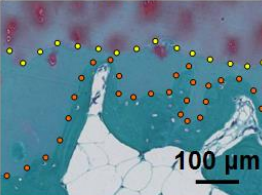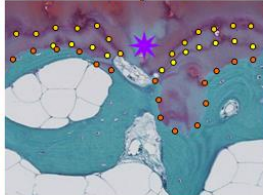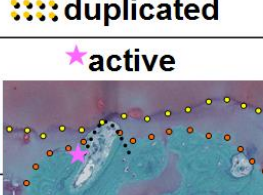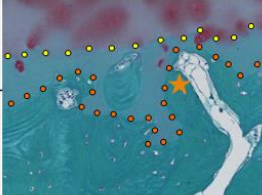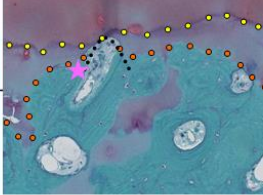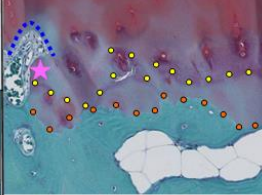
femoral head, especially when only counting active channels [9]. The present study, which used deterioration level rather than age, did not show as analogous an increase in active channels, but only a modestly higher density in Grade 3 and Grade 4. However, the increase here in penetration of channels to the tidemark can be seen as an analogous result, as the Lane analysis used en face sections to quantify the channels, and channels that penetrate further are more likely to be counted, or over-represented, in an en face analysis.

The penetration of vascular channels and interruption of the tidemark can potentially implications for the overlying cartilage. The hydraulic conductivity of the cartilage-bone unit has been shown to increase significantly in samples with partially and fully eroded cartilage [15]. Vascular channels crossing the tidemark may be an important contributor to this observation, which affects the unit's barrier function and lead to overall compromise of the synovial joint. In murine models, the diffusivity of the subchondral plate to macromolecules on the size order of cytokines has been shown to increase, along with an increase in the number of small channels crossing the tidemark [16]. Overall, there is a lack of studies which quantify vascular channels in the subchondral bone directly, which is necessary to further reinforce that compromise in the integrity of the tidemark and barrier function of the ScP can be affected by or have an effect on the health of the overlying cartilage. This was primarily due to lack of or difficulties inherent in 3-D techniques, which is being addressed with improving technology. The present study sets the foundation in terms of number and types of expected channels, for a more thorough 3-D analysis that can target specific hypotheses

about how the vascular channels and tidemark changes of the ScP is linked to cartilage deterioration.

4.6 Acknowledgments

Figure 4.1: Tidemark and Vascular Channel Categorization. Tidemark disruptions were counted and the number of tidemarks was assessed. Vascular channels in the ScP were categorized based on activity level and extension to the cement line or the tidemark. Yellow dotted line: tidemark, orange dotted line: cement line.
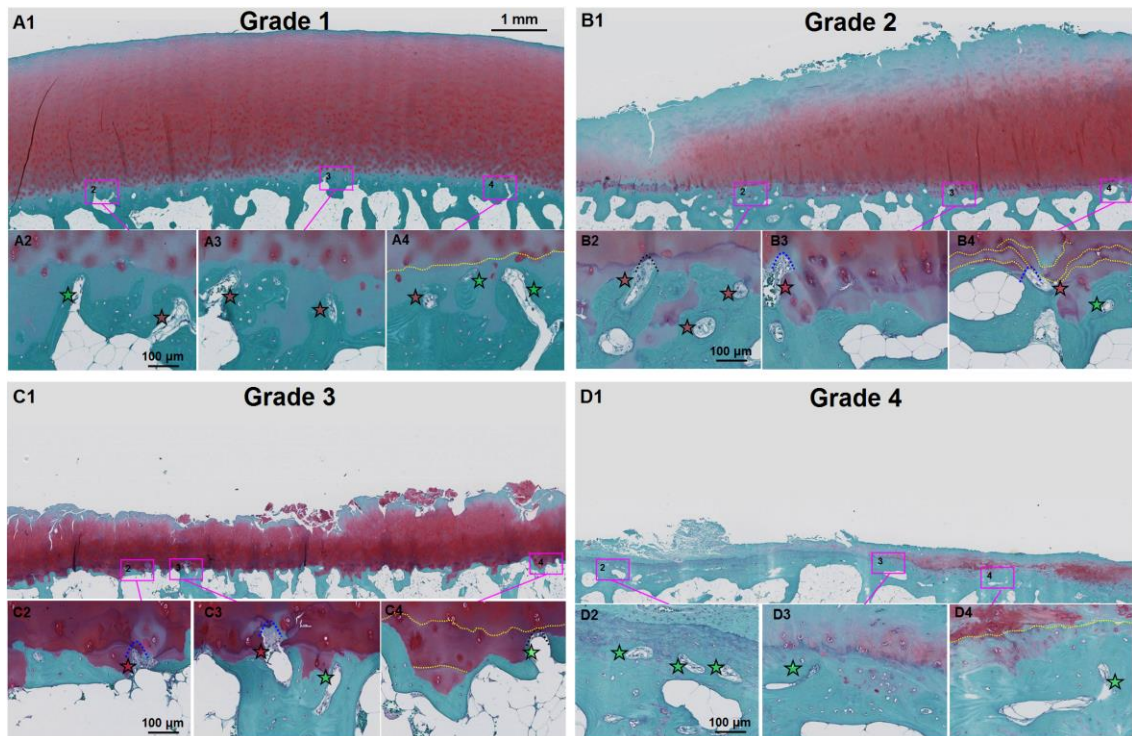
Figure 4.2: Histological Features of Normal and Deteriorated Subchondral Plate. Annotated examples of histological sections of the osteochondral tissue across the 10.4 mm length, for (A) normal, (B) Grade 2, (C) Grade 3, (D) Grade 4 osteochondral tissue, with zoomed sections (2-4) illustrating examples of vascular channel and tidemark features. Green star: inactive vascular channel, red star: active vascular channel, black dotted line: vascular channel breaching cement line, blue dotted line; vascular channel breaching tidemark, yellow dotted line: traced outline of tidemark(s).

Table 4.1: Tidemark Discontinuities and Vascular Channel Linear Density. The number of tidemarks and the density of tidemark discontinuities, vascular channels, reported as mean ± SD. Between all Grade 1Y and Grade 1O metrics, the significance was p>0.05 by the Tukey test (no statistical difference), so they were combined into one group for statistical power.

Grade	1 (Y+O)	2	p, 2 vs 1	3	p, 3 vs 1	4	p, 4 vs 1
age	42 ± 17	68 ± 11		74 ± 16		76 ± 11	
tidemark #	1.3 ± 0.6	2.7 ± 0.8	<0.05	2.5 ± 0.8	0.06	1.5 ± 1.5	0.95
tidemark discontinuities [# / 10 mm slide length]	2.4 ± 5.5	13.2 ± 7.9	<0.05	11.7 ± 7.7	0.05	5.2 ± 7.7	0.84
vascular channels [# / 10 mm slide length]	35.5 ± 11.8	25.1 ± 21.1	0.47	21.0 ± 13.5	0.20	25.4 ± 10.8	0.50
inactive	22.6 ± 7.3	11.9 ± 8.0	<0.05	8.3 ± 7.8	<0.01	11.1 ± 8.3	<0.05
active	12.9 ± 7.6	13.2 ± 16.5	1.00	12.7 ± 9.4	1.00	14.3 ± 12.5	0.93
distal to cement line	6.9 ± 5.2	9.1 ± 6.5	0.85	4.7 ± 4.1	0.85	5.2 ± 6.2	0.92
distal to tidemark	1.1 ± 1.3	4.7 ± 3.1	0.07	2.8 ± 2.9	0.63	2.9 ± 4.5	0.55

4.7   References

1.   Clark JM, Huber JD. The structure of the human subchondral plate. J Bone Joint Surg Br 1990;72: 866-73.

2.   Oegema T, Jr., Carpenter R, Hofmeister F, Thompson RC, Jr. The interaction of the zone of calcified cartilage and subchondral bone in osteoarthritis. Microsc Res Tech 1997;37: 324-32.

3.   Redler I, Mow VC, Zimny ML, Mansell J. The ultrastructure and biomechanical significance of the tidemark of articular cartilage. Clin Orthop Relat Res 1975;112: 357-362.

4.   Wang F, Ying Z, Duan X, Tan H, Yang B, Guo L, Chen G, Dai G, Ma Z, Yang L. Histomorphometric analysis of adult articular calcified cartilage zone. J Struct Biol 2009;168: 359-65.

5.   Clark JM. The structure of vascular channels in the subchondral plate. J Anat 1990;171: 105-15.

6.   Jilka RL. Biology of the basic multicellular unit and the pathophysiology of osteoporosis. Medical and pediatric oncology 2003;41: 182-5.

7.   Shibakawa A, Yudoh K, Masuko-Hongo K, Kato T, Nishioka K, Nakamura H. The role of subchondral bone resorption pits in osteoarthritis: MMP production by cells derived from bone marrow. Osteoarthritis Cartilage 2005;13: 679-87.

8.   Burr DB, Gallant MA. Bone remodelling in osteoarthritis. Nat Rev Rheumatol 2012;8: 665-73.

9.   Lane LB, Villacin A, Bullough PG. The vascularity and remodelling of subchondrial bone and calcified cartilage in adult human femoral and humeral heads. An age- and stress- related phenomenon. J Bone Joint Surg Br 1977;59: 272-8.

10.   Oettmeier R, Abendroth K, Oettmeier S. Analyses of the tidemark on human femoral heads. II. Tidemark changes in osteoarthrosis--a histological and histomorphometric study in non-decalcified preparations. Acta Morphol Hung 1989;37: 169-80.

11.   Thomsen JS, Laib A, Koller B, Prohaska S, Mosekilde L, Gowin W. Stereological measures of trabecular bone structure: comparison of 3D micro computed tomography with 2D histological sections in human proximal tibial bone biopsies. Journal of microscopy 2005;218: 171-9.

12. Bobinac D, Spanjol J, Zoricic S, Maric I. Changes in articular cartilage and subchondral bone histomorphometry in osteoarthritic knee joints in humans. Bone 2003;32: 284-90.

13. Sniekers YH, Intema F, Lafeber FP, van Osch GJ, van Leeuwen JP, Weinans H, Mastbergen SC. A role for subchondral bone changes in the process of osteoarthritis; a micro-CT study of two canine models. BMC Musculoskelet Disord 2008;9: 20.

14. Botter SM, van Osch GJ, Clockaerts S, Waarsing JH, Weinans H, van Leeuwen JP. Osteoarthritis induction leads to early and temporal subchondral plate porosity in the tibial plateau of mice: an in vivo microfocal computed tomography study. Arthritis Rheum 2011;63: 2690-9.

15. Hwang J, Bae WC, Shieu W, Lewis CW, Bugbee WD, Sah RL. Increased hydraulic conductance of human articular cartilage and subchondral bone plate with progression of osteoarthritis. Arthritis Rheum 2008;58: 3831-42.

16. Pan J, Wang B, Li W, Zhou X, Scherr T, Yang Y, Price C, Wang L. Elevated cross-talk between subchondral bone and cartilage in osteoarthritic joints. Bone 2012;51: 212-7.

CHAPTER 5:

3-D VISUALIZATION OF SUBCHONDRAL PLATE VASCULAR CHANNELS BY DIGITAL VOLUMETRIC IMAGING

5.1   Abstract

Introduction. The subchondral plate (ScP), comprised of the calcified cartilage and subchondral bone plate, is an active remodeling site in osteoarthritis (OA). Vascular channels, which include a blood vessel protruding from the marrow and optionally a basic multicellular remodeling unit, are present in the bone at the cartilage interface. These channels have many types, based on structure, location, and orientation, but are difficult to image and visualize in three dimensions. The aim of this study was to establish and characterize the appearance of vascular channel with the Digital Volumetric Imaging method in normal and OA osteochondral tissue. The hypothesis was that the vascular channels of degenerated osteochondral tissue are structurally distinct in a way that implicates the active remodeling of the tissue during this stage.

Methods. From six knees of different human donors, with three having partially eroded cartilage at the MFC, a $\sim(4 \text{ mm})^3$ block of osteochondral tissue was extracted, fixed, decalcified, and imaged with DVI. The output 3-D data was assessed for the vascular channels, which were categorized based on morphological and spatial categories,

including the size, orientation, location, and presence or absence of a bony cap. The general patterns observed in the samples regarding the channels as a whole were also described.

Results. The vascular channels in all samples appeared as small fingerlike protrusions of the marrow, but the size, surrounding cells, and location of the channels revealed differences between the normal and deteriorated. The normal channels were typically small in diameter, inactive with few surrounding cells, oriented vertically, were bony capped and all under the cement line and within the subchondral bone. The channels of deteriorated ScP, were larger, with some were active, oriented more obliquely, and with an open or missing bony cap. The greatest difference was that many of these channels protruded past the cement line or even the tidemark, and contacted the calcified and uncalcified cartilage.

Discussion. The more variegated appearance of the OA vascular channels, and the specific distinct variations of activity, size and penetration depth, indicated that many of these channels participate in active remodeling. Channels protruding past the tidemark in the OA may lead to altered communication between subchondral bone and cartilage. These changes are more typically observed, in mild OA, suggesting that the mechanistic results may have an important role in the pathogenesis. The visualization of these channels in 3-D by DVI provides an important new tool that is complementary to established methods such as CT and histology, for visualizing active bone remodeling effects on cartilage.

5.2   Introduction

In the normal adult synovial articulating joint, the articular cartilage is attached to underlying trabecular bone (TB) by a subchondral plate (ScP) composed of two tissue layers, calcified cartilage (CC), ~100 μm thick, and "corticalized" subchondral bone plate (ScBP), ~300 μm thick [1]. The ScP is bounded at the superficial end by the tidemark, or calcification front of the CC, and at the deep end by the "ScP end boundary", an artificial boundary between the "corticalized" region of continuous bone and the cancellous trabecular bone [2]. The appearance of the ScP has been well described in 2-D and 3-D by several visualization methods [2-5]. In histology, using the clearly identifiable metachromatic tidemark, which is distinctly visible with most contrast stains, and the trabecular bone marrow voids, whose peaks clearly form the ScP end boundary, the ScP can be easily visually isolated [6, 7].

The ScP contains pores, which are substantially comprised of vascular channels or other supporting structures important in bone remodeling and OA pathogenesis [2, 3, 8]. Clark described these pores as being primarily of two types: large channels which are extensions of the marrow voids, and small channels which contain one or more Haversian canals, encasing a blood vessel, sometimes structured around an osteon, the classical basic unit of cortical bone [3]. Many of these vessels protrude near the tidemark, but are closed by a bony cap. However, some of these vessels are open or have no bone at the superficial end of the cap, or have the bony cap missing altogether, and some of the vessels were fenestrated, leading to possibility of communication of the vascular channels with the other tissue layers [3]. Oettmeier observed that the tidemark was more likely to be penetrated by these vascular channels, open or closed, in mild to moderate degrees of OA [9]. Additionally, these vascular channels can be part of a basic multicellular unit, during which they are sometimes referred to as resorption pits or "actively remodeling" vascular channels [10, 11].

Although a deeper investigation into the ScP vascular channels is likely to bring insight into the mechanism of age related cartilage degeneration and OA, there are unique challenges from their 3-D structure and distribution that have limited studies that visualize and quantify them to this point. Such challenges can be addressed by new visualization methods that are capable of resolving them at an acceptable resolution, with biological contrast to see their activity and distinct features, and in three dimensions [12]. Because these channels are three-dimensional "tubes" which may protrude vertically, obliquely, and occasionally horizontally, thin 2-D sections will often not capture their true structure. The 3-D tube may be seen as a hole, a finger, or something in between, depending on the orientation of the cut section relative to the orientation of the channel [3, 4]. Additionally, when trying to quantify these vascular channels, a single section usually represents a very small proportion of the actual volume of the sampled region desired, and trying to count channels through sections is likely to yield an inaccurate result, even with stereological estimation [13]. En face (horizontal) histological sections or projection images from electron microscopy may give improved results in comparison, but may still be inaccurate, due to the complex 3-D orientation and possible branching of the vascular channels.

To address these challenges, there have been recently developed techniques to visualize the 3-D microstructure of the subchondral bone, including microcomputed tomography (microCT) [14-18], nanoCT (same, but with <1 um resolution per voxel) [19], as well as Digital Volumetric Imaging (DVI), which uses systematic serial face sectioning and imaging [20]. Both provide sufficient resolution to see biological features in detail in 3-D [20, 21]. In the present study, DVI is used to characterize and systematically categorize the three dimensional structure and biology of vascular channels visible in the ScP of normal and OA samples [9]/ Once the 3-D details of the structure, types, size, location, orientation of the vascular channels have been

established, study of other details such as their density and the changes they undergo in degeneration and osteoarthritis, with possible pathogenic links, can be pursued. The primary aim of the study was to establish and characterize the appearance of vascular channel with the DVI method in (1) normal and (2) degenerated/OA osteochondral tissue. The hypothesis was that the penetrating vascular channels of degenerated osteochondral tissue have a distinctive appearance in DVI, based on being uncapped and being associated with active remodeling.

5.3   Materials and Methods

5.3.1 Study Design

Osteochondral tissue, containing the ScP, was used from six donors, n = 3 from normal and n = 3 from clinical OA donors. The normal donor knee was retrieved from a cadaveric tissue bank, and the OA donors from remnant tissue extracted during a total knee arthroplasty, both with IRB approval. Each of the six donor knees had a volume selected from the medial femoral condyle (MFC), taken from a weight-bearing region that represented the worst grade in the condyle: (1) normal/non-fibrillated for the normal donor sample, and (3) partial thickness erosion for all four OA donor samples. This selected volume was processed (**section 5.3.2**), imaged by DVI (**section 5.3.3**), and qualitatively assessed for the different types of vascular channels (**section 5.3.4**) (n=3 each, at 10X), or counted based on location (**section 5.3.5**) (n=2 each, at 4X).

5.3.2 Sample Preparation

From each donor knee MFC, the selected target volume ((~4 mm)^3 cube (50% bone, 50% cartilage) centered around the ScP) was extracted using a scalpel and processed to prepare for DVI imaging. Each sample cube was fixed in 4% paraformaldehyde in phosphate-buffered saline for 48 hours, then decalcified in a solution for 10% EDTA in phosphate buffered saline for at least 72 hours. The samples were then stained with Acridine Orange and Eosin Y, sequentially dehydrated with graded alcohol, held in xylene, and embedded in Spurr resin as described previously [20, 22].

5.3.3 Surface Imaging

The cured resin block was sectioned and imaged in a DVI machine (MicroSciences Corp., Corte Madera, CA) as described previously [20, 22]. The DVI acquired the block face images of the tissue with a 10X objective, cutting the block after each image at a set thickness equivalent to the pixel resolution of each image acquired (0.89 μm), for isotropic voxel size. The machine software processed the data into a stack of ~(2000 x 2000) pixel RGB images (~2000 images at (0.89 μm)/pixel resolution, ~10GB per set), or a 3-D dataset encompassing a (1.8 mm)^3 volume.

5.3.4. Image Processing and Data Reduction to Vascular Channels.

The output dataset was aligned using 3-D image rotation software so that the tidemark was level relative to the frame of reference of the sample, and then cropped systematically to remove dark areas (excess imaged area) around the sample. Specific vascular channels were located within each sample data as the dark (mostly unstained) fingerlike projections that extend out from the marrow spaces (also mostly unstained). Vascular channels were categorized for the features listed in **Table 5.1**: presence and type of bony cap, location/penetration depth, orientation, and channel activity, described in **sections 5.3.4.1-4** below. The types of vascular channels present or prevalent in normal and OA samples were described, for the categorization above as well as their general size and morphology. Additionally, other features such as the tidemark, cement line, and marrow voids were also noted where relevant to the categorization or description of each channel.

5.3.4.1 Vascular Channel Bony Cap

Vascular channels were either entirely inside the bone, in which case they were considered by default to have a closed bony cap, or they extended past the surrounding bone. Channels that extended past the bone may have still had a bony cap, or a

surrounding layer of lamellar bone outlining the channel. If the bony cap completely covered the sample, the bone channel was categorized as **(C)**losed. If there was any opening (missing bone) on the superficial end of the cap, the cap was **(O)**pen. Finally, if the bony cap was absent, or no bone in significant parts of the walls of the channel, the vascular channel was given the category missin**(G)** bony cap.

5.3.4.2 Location / Penetration Depth

Vascular channels were categorized based on the depth to which they penetrated (deep-to-superficial), that is, the location of the blunt end of the channel, based on surrounding layer: bone, calcified cartilage or uncalcified cartilage. If the vascular channel was entirely below the calcified cartilage layer, the channel was classified as **(N)**on-penetrating. If the channel reached superficially to the point where the surrounding region in the horizontal direction was calcified cartilage, it was categorized as penetrating cement **(L)**ine. It should be noted that a vascular channel that is capped cannot penetrate the cement line as the surface of the cap is part of the surface of the cement line by definition. Finally, if the vascular channel either reached the uncalcified cartilage, or breached to the tidemark (any tidemark in the case that the tidemark was duplicated), it was categorized as penetrating **(T)**idemark.

5.3.4.3 Orientation

Each channel was measured for the deviation of its primary axis from the superficial-deep axis. If this angle was less than 15°, it was categorized as **(V)**ertical, otherwise it was categorized as **(O)**blique. It was possible for a vascular channel to branch and have parts that were both vertical and oblique, in which case the largest segment of the channel was used to measure and categorize it for this purpose.

5.3.4.4 Activity

Vascular channels contained cells within their volume, staining positively for Acridine Orange. Qualitatively, if the channel stained brightly for many cells, it was categorized as **(A)**ctive. Otherwise, it was categorized as **(I)**nactive.

5.3.5 Vascular Channel Quantification by Type

For each group, normal and OA, vascular channels were counted in a $(1 \text{ mm})^2$ ScP surface area region, based their presence of a bony cap, location, orientation, and activity with these delineations following those outlined in **section 5.3.4.1** to **5.3.4.4**. The number of channels of each category was tabulated, and the average total number of channels was also reported. An unpaired independent samples two-tailed t-test was used to compare the normal and OA groups.

5.4   Results

The general appearance of the vascular channels in the DVI imaging data is described below (**section 5.4.1**), followed by detailed description of the different types or feature categories, sorted by prevalence in grade of sample: normal (**section 5.4.2**) and OA (**section 5.4.3**).

5.4.1 General Appearance of Vascular Channels

Vascular channels were apparent as small fingerlike protrusions, distinct from the surrounding bone or calcified cartilage tissue in that they did not stain at all for Eosin Y (green) and had minimal staining on a volume basis for Acridine Orange (red). These protrusions varied in size from 20 μm to over 100 μm in diameter, and had some variation in shape, such as being thicker and rounder at the end of the channel, or being uniform in thickness throughout. However, all protrusions had the same general morphology of being tubelike with a blunt, round terminus, and connected to the larger marrow spaces below (which were similarly dark and unstained throughout most of their volume). The vascular channels typically also had a thin red halo or outline, possibly representing the endothelial lining or be an artifact of the stain. Many of the vascular channels were filled with cells that stained positively for Acridine Orange, as interspersed red dots or fibers that represented a small volume of the vascular channel.

5.4.2 Vascular Channels of Normal ScP

In the normal ScP, vascular channels (**Fig. 5.2**) typically had uniform thickness throughout their length, and were typically thin (<50 μm diameter). Vascular channels were capped, without penetration the cement line or tidemark. There were few cells inside the vascular channel, and those that did appear did not stain brightly for Acridine Orange, indicative of inactivity. Both straight and oblique vascular channels were

present, although channels with a slight angle in the S-D axis (5-30°) was most common, and channels were rarely perfectly straight, or angled much more than 30°, unless they were connecting marrow space to marrow space rather than terminating in a blunt end.

5.4.3 Vascular Channels of OA ScP

In the OA ScP, vascular channels (**Fig. 5.4**) were variable in thickness: some were very thin, on similar to normal channels (<50 μm diameter), other channels were on the order of 100 μm diameter in thickness. There were channels that were non-penetrating and completely below the cement line, and with a closed bony cap, but they were thicker on average compared to those found in the normal samples. In contrast to the normal sample, there were channels that penetrated the cement line and tidemark, and either had an open end of a bony cap, or missing the bony cap. In terms of morphology, the shape of the vascular channels, especially those that were uncapped or open, were highly variable. Where there were multiple tidemarks, the deeper tidemarks were most commonly penetrated by the channels, while the most superficial tidemark was more rarely breached. Some had a smooth, rounded, edge, similar to channels in the normal sample, while others had irregular, wavy edges. Channels that penetrated past the tidemark were more likely to have a wavy edge. Following from this, these irregularly shaped channels also did not have uniform thickness throughout their length, as sometimes their blunt terminus was larger in diameter than the remainder of the channel by a factor of two or three. In terms of orientation, the angle of the channels relative to the S-D axis was highly variable: some were more horizontal than vertical (>45°), some were very near perfectly straight (<5°), and many were in between. Channels that were uncapped or open were more likely to have horizontally angled vascular channels, but also channels that were very close to the vertical. Channels, both

closed and non-penetrating and open/uncapped and penetrating, had many, brightly fluorescing cells staining for Acridine Orange, indicative of high activity.

5.4.4 Vascular Channel Quantification

The number density of the vascular channels reaching the tidemark, and the ratio of inactive to active vascular channels, were distinctly different in OA partial erosion (**Table 5.1**). Specifically, more than a sixth of the vascular channels counted penetrated past the tidemark in the OA samples, but there were very few channels penetrating in the normal sample. The normal group had 36.0 ± 8.9 vascular channels $(25.3 \pm 5.0$ inactive / 10.7 ± 8.6 active) and the OA group had 34.0 ± 10.8 / mm^2 $(9.3 \pm 7.1$ inactive / 24.7 ± 17.0 active). For channels that penetrated to at least the tidemark, the normal group had 0.7 ± 1.2 and the OA group had 7.7 ± 4.0 / mm^2.

5.5   Discussion

The vascular channels of the ScP were more variegated in OA than in normal samples in ways that indicated more bone remodeling and potential communication between bone and cartilage. The variations distinct in OA ScP were that there were channels that penetrated past the cement line and tidemark, were thicker and more variable in shape and orientation, and had more cells within them. The highly cellular, structurally irregular, and abnormally thick channels are indicative of channels that are member of a basic multicellular unit (BMU), the unit of remodeling and turnover in bone, linking them to active bon remodeling in OA. The channels protruding past the tidemark may contribute to the classical observation that the tidemark is more disrupted and roughened in OA, and directly link this observed alteration to communication between subchondral bone and cartilage.

There were some limitations in this study related to the sample preparation and DVI visualization technique. The cell staining used was Acridine Orange, which stains positively for nuclei but does not differentiate between different types of cells. Staining for more specific markers in cells which can positively identify member cells of BMUs such as osteoclasts and osteoblasts can help confirm the activity of the vascular channel in remodeling, but such stains are currently untested with the DVI imaging system. The DVI protocol used in this study utilized a magnification of 10X, yielding a resolution of $(0.89 \ \mu m)^3$/voxel. This resolution was inferior to that of the stronger magnifications in standard 2-D histology methods (20X, 40X), and was chosen so that there was a reasonable field of view (increased magnification requires a smaller field of view). However, this resolution proved sufficient to see detailed structure of the vascular channels and their member cells. The preparation and storage of the samples may have contributed to cells being cleaned out from the vascular channels. The samples were frozen for substantial time prior to being thawed for DVI imaging, and the fixation,

decalcification and staining required numerous solution changes, prior to the actual sectioning. Thus, the observation that the normal sample has far fewer cells than the OA samples must be qualified with the possibility that the storage and handling of one or the other may have artificially removed cells from the interior of the channels, rather than a difference in activity.

The differences in vascular channels between normal and degenerated osteochondral tissue are consistent with past observations of the subchondral bone with aging and disease. Tidemark disruption was observed to be a "low grade" change, observed with mild degeneration prior to more marked changes of the cartilage and bone [9]. Since protruding vascular channels may be associated with the tidemark disruption, this may be indicative of bone remodeling that alters cartilage-bone communication starts with low-grade changes in the cartilage and thus can contribute mechanistically to further breakdown of the cartilage. The observation that there were more "active" vascular channels with degeneration was analogous to Lane's observation that active vascular channel density increased in the femoral head with aging [10]. The present study is the first, to the author's knowledge, to characterize vascular channels of the ScP in three dimensions.

Visualization of the vascular channels with the DVI method is complementary to the information provided in other methods, and can help elucidate its role in pathogenesis of cartilage degeneration and OA. Characterization and categorization of the vascular channels is the first step to being able to quantify them in a way that isolates the channels that are important to bone remodeling and potential cartilage-bone communication. The categorization method presented here can aid in this quantification, both with this method, and in other 3-D methods where there is not as much biological contrast, such as in μCT. For example, co-localization of the channels between μCT and DVI can help identify which channels are open or uncapped in μCT.

This can help provide a more robust and statistically strong way of counting and comparing channels, since μCT offers a much larger field of view. The visualization of the channels by DVI is the 3-D analog to the well-described 2-D histological assessments of the vascular channels or "resorption pits". The 2-D histology provides larger fields of view at higher resolution in the S-D and one of the orthogonal axes, but can omit details and features of the channel like the completeness of the bony cap and the true orientation. Thus, the present study provides complementary information to the active bone remodeling observed in past studies, especially regarding the surroundings of the channel, their morphology, location and orientation. Further development of this method will help elucidate the degree to which bone remodeling contributes to disease pathogenesis, and provide further evidence to whether treatments such as resorption inhibitors can be effective for treating progressing OA.

5.6   Acknowledgments
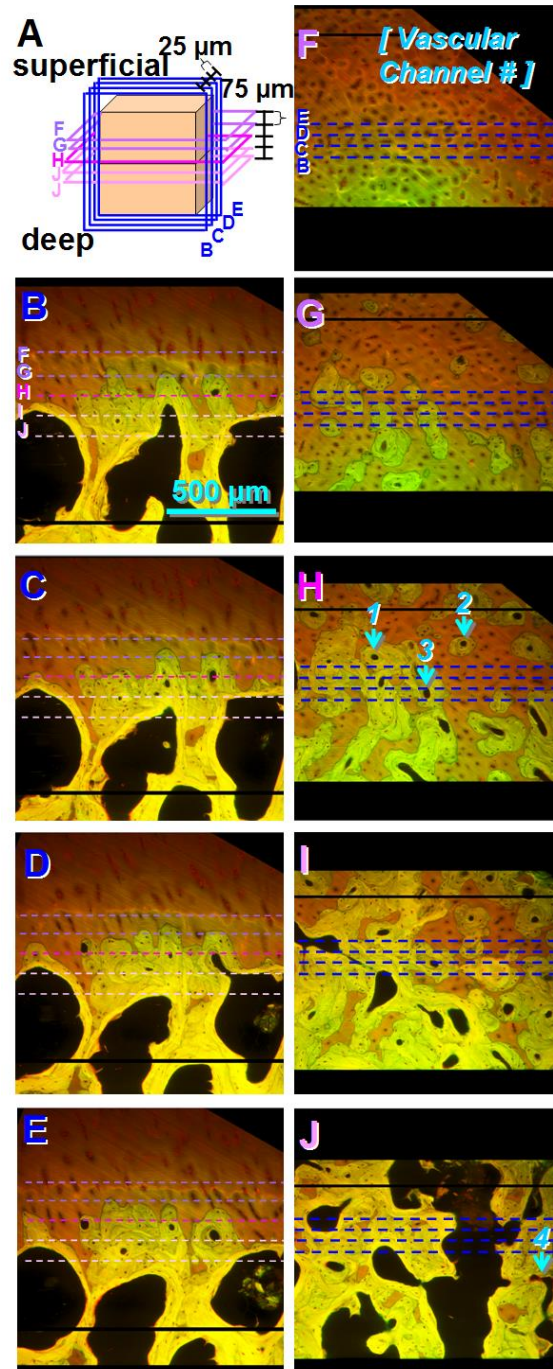
Figure 5.1: Overview of the Normal Subchondral Plate. Cross sections of subchondral plate 3-D DVI image volume, in vertical (B-E) and horizontal (F-J, at different depths) planes. Vascular channels annotated in horizontal plane.
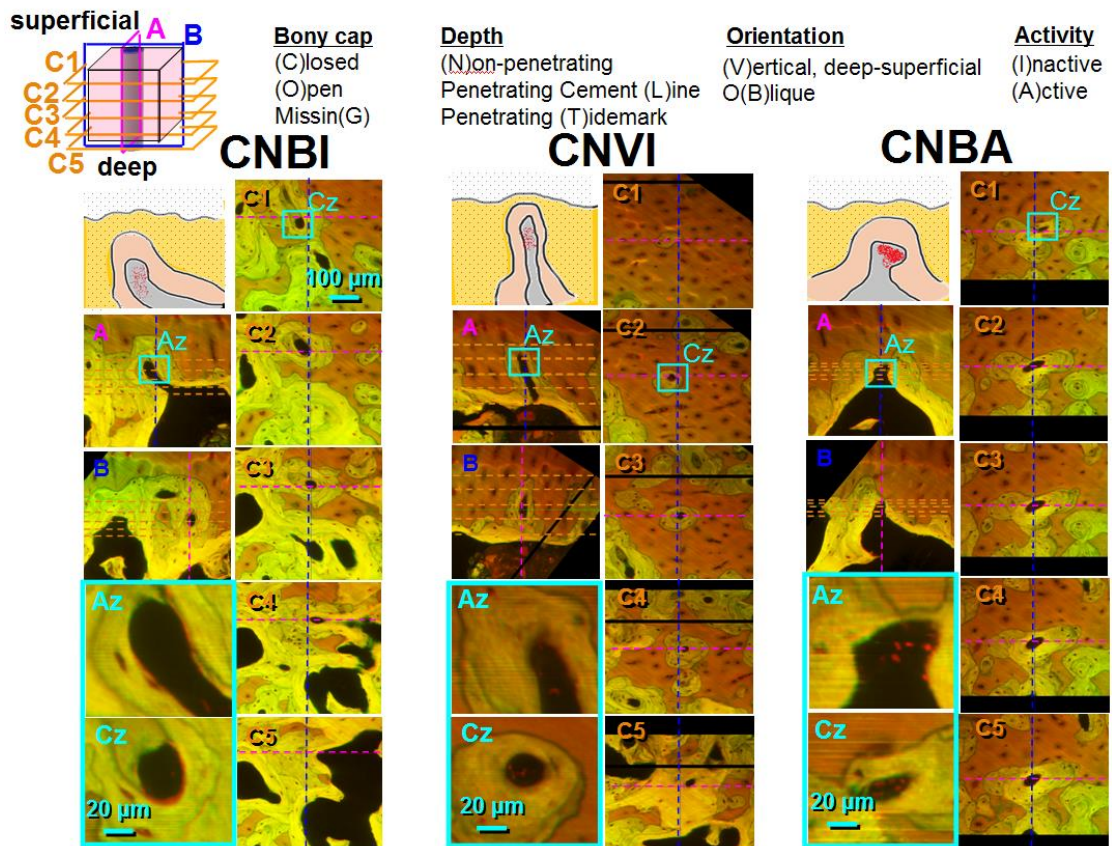
Figure 5.2: Vascular Channels of the Normal Subchondral Plate. Examples of vascular channels of the normal ScP. Shown in three orientations, vertical (A,B) and horizontal (C1-C5).
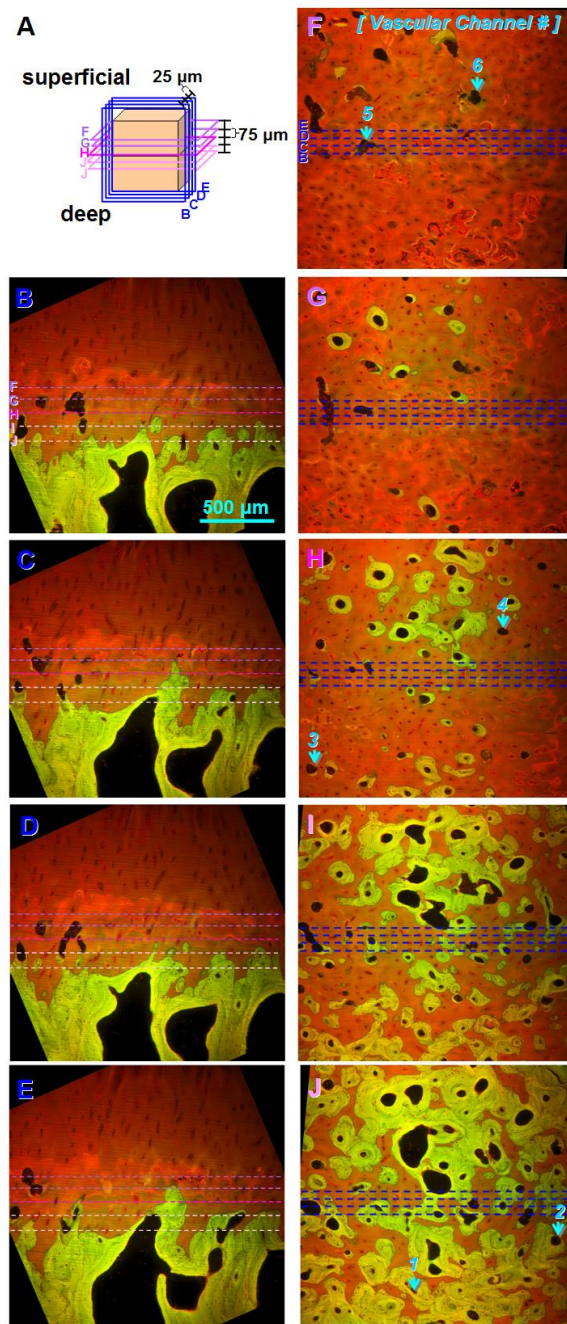
Figure 5.3: Overview of the OA Subchondral Plate. Cross sections of subchondral plate 3-D DVI image volume, in vertical (B-E) and horizontal (F-J, at different depths) planes. Vascular channels annotated in horizontal plane.
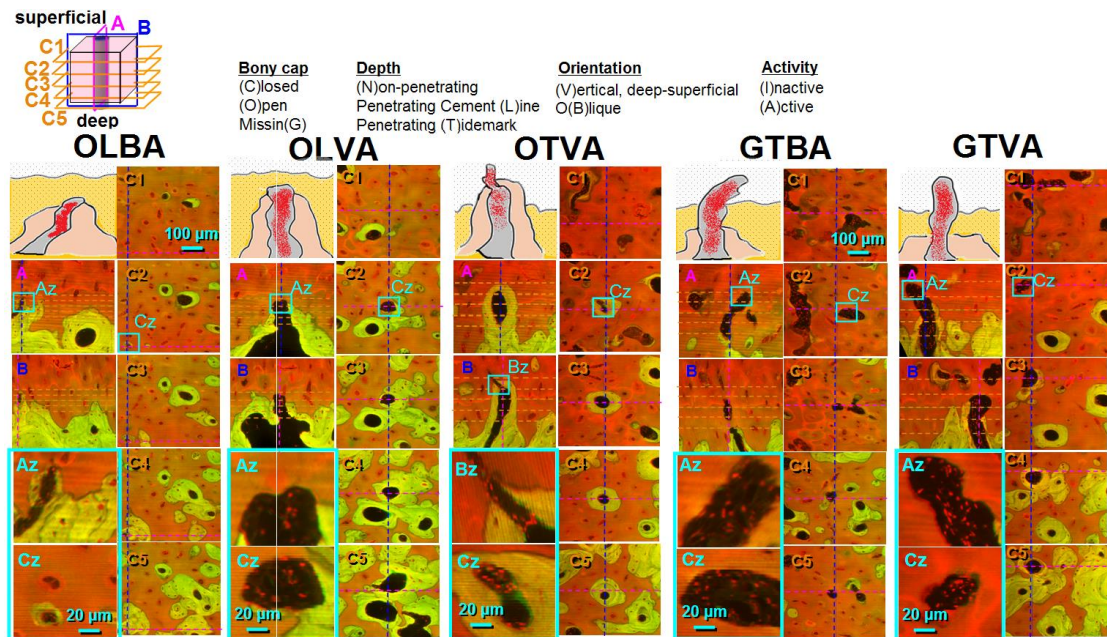
Figure 5.4: Vascular Channels of the OA Subchondral Plate. Examples of vascular channels in the OA ScP. Shown in three orientations, vertical (A,B) and horizontal (C1-C5).

Table 5.1: Quantification of Vascular Channel Types in Normal and OA ScP.
Number of vascular channels of each type category counted in $(1 \text{ mm})^2$ area of n=3 each of normal and OA ScP, reported as mean±SD. *: p<0.05 vs. normal.

area number density [# / mm]^2	NL-1 n=3	OA-3 n=3
(**C**)losed	28.0 ± 1.0	18.0 ± 10.4
(**O**)pen	8.0 ± 8.7	12.0 ± 4.4
missin(**G**)	0	4.0 ± 2.6
(**N**)on-penetrating	27.7 ± 1.2	18.0 ± 10.4
extend to C(**L**)	7.7 ± 8.1	8.3 ± 3.2
extend to (**T**)M	0.7 ± 1.2	7.7 ± 4.0 *
(**V**)ertical	15.3 ± 5.8	15.0 ± 6.9
o(**B**)lique	20.7 ± 3.5	19.0 ± 4.6
(**I**)nactive	25.3 ± 5.0	9.3 ± 7.1 *
(**A**)ctive	10.7 ± 8.6	24.7 ± 17.0
total	36.0 ± 8.9	34.0 ± 10.8

5.7   References

1.   Oegema T, Jr., Carpenter R, Hofmeister F, Thompson RC, Jr. The interaction of the zone of calcified cartilage and subchondral bone in osteoarthritis. Microsc Res Tech 1997;37: 324-32.

2.   Burr DB, Gallant MA. Bone remodelling in osteoarthritis. Nat Rev Rheumatol 2012;8: 665-73.

3.   Clark JM. The structure of vascular channels in the subchondral plate. J Anat 1990;171: 105-15.

4.   Clark JM, Huber JD. The structure of the human subchondral plate. J Bone Joint Surg Br 1990;72: 866-73.

5.   Duncan H, Jundt J, Riddle JM, Pitchford W, Christopherson T. The tibial subchondral plate. A scanning electron microscopic study. J Bone Joint Surg Am 1987;69: 1212-20.

6.   Milz S, Eckstein F, Putz R. The thickness of the subchondral plate and its correlation with the thickness of the uncalcified articular cartilage in the human patella. Anat Embryol (Berl) 1995;192: 437-44.

7.   Milz S, Putz R. Quantitative morphology of the subchondral plate of the tibial plateau. J Anat 1994;185 (Pt 1): 103-10.

8.   Findlay DM. Vascular pathology and osteoarthritis. Rheumatology 2007;46: 1763-8.

9.   Oettmeier R, Abendroth K, Oettmeier S. Analyses of the tidemark on human femoral heads. II. Tidemark changes in osteoarthrosis--a histological and histomorphometric study in non-decalcified preparations. Acta Morphol Hung 1989;37: 169-80.

10.   Lane LB, Villacin A, Bullough PG. The vascularity and remodelling of subchondrial bone and calcified cartilage in adult human femoral and humeral heads. An age- and stress- related phenomenon. J Bone Joint Surg Br 1977;59: 272-8.

11.   Shibakawa A, Yudoh K, Masuko-Hongo K, Kato T, Nishioka K, Nakamura H. The role of subchondral bone resorption pits in osteoarthritis: MMP production by cells derived from bone marrow. Osteoarthritis Cartilage 2005;13: 679-87.

12. Hwang J, Bae WC, Shieu W, Lewis CW, Bugbee WD, Sah RL. Increased hydraulic conductance of human articular cartilage and subchondral bone plate with progression of osteoarthritis. Arthritis Rheum 2008;58: 3831-42.

13. Thomsen JS, Laib A, Koller B, Prohaska S, Mosekilde L, Gowin W. Stereological measures of trabecular bone structure: comparison of 3D micro computed tomography with 2D histological sections in human proximal tibial bone biopsies. Journal of microscopy 2005;218: 171-9.

14. Intema F, Hazewinkel HA, Gouwens D, Bijlsma JW, Weinans H, Lafeber FP, Mastbergen SC. In early OA, thinning of the subchondral plate is directly related to cartilage damage: results from a canine ACLT-meniscectomy model. Osteoarthritis Cartilage 2010;18: 691-8.

15. Sniekers YH, Intema F, Lafeber FP, van Osch GJ, van Leeuwen JP, Weinans H, Mastbergen SC. A role for subchondral bone changes in the process of osteoarthritis; a micro-CT study of two canine models. BMC Musculoskelet Disord 2008;9: 20.

16. Botter SM, van Osch GJ, Waarsing JH, Day JS, Verhaar JA, Pols HA, van Leeuwen JP, Weinans H. Quantification of subchondral bone changes in a murine osteoarthritis model using micro-CT. Biorheology 2006;43: 379-88.

17. Bobinac D, Spanjol J, Zoricic S, Maric I. Changes in articular cartilage and subchondral bone histomorphometry in osteoarthritic knee joints in humans. Bone 2003;32: 284-90.

18. Rodriguez AG, Slichter CK, Acosta FL, Rodriguez-Soto AE, Burghardt AJ, Majumdar S, Lotz JC. Human disc nucleus properties and vertebral endplate permeability. Spine 2011;36: 512-20.

19. Peyrin F, Dong P, Pacureanu A, Langer M. Micro- and nano-CT for the study of bone ultrastructure. Current osteoporosis reports 2014;12: 465-74.

20. Jadin KD, Bae WC, Schumacher BL, Sah RL. Three-dimensional (3-D) imaging of chondrocytes in articular cartilage: growth-associated changes in cell organization. Biomaterials 2007;28: 230-9.

21. Bryant SJ, Cuy JL, Hauch KD, Ratner BD. Photo-patterning of porous hydrogels for tissue engineering. Biomaterials 2007;28: 2978-86.

22. Ewald AJ, McBride H, Reddington M, Fraser SE, Kerschmann R. Surface imaging microscopy, an automated method for visualizing whole embryo samples in three dimensions at high resolution. Dev Dyn 2002;225: 369-75.

CHAPTER 6:

CHONDROCYTE FATE INFERRED FROM 3-D BIOIMAGE INFORMATICS OF CELL ORGANIZATION IN HUMAN ARTICULAR CARTILAGE

6.1   Abstract

Introduction. The cellularity and cell disorganization of chondrocytes within cartilage may contribute to age-related deterioration. Chondrocytes have limited ability to remodel at a distance, so that matrix regions far from cells may be susceptible to damage. With aging, the cellularity of the superficial zone decreases apparently due to cell death, but as osteoarthritis (OA) develops, cellularity may increase due to proliferation, cluster formation, and other organizational alterations. Automated serial block-face imaging or Digital Volumetric Imaging (DVI) can visualize larger tissue volumes in 3-D at the cellular scale. The aims of this study were to (1) introduce 3-D bioimage informatics analysis to assess the organization of cells and cell clusters within human articular cartilage, and (2) to compare results for four grades of age- and OA-related deterioration to test whether matrix is susceptible to damage via local hypocellularity.

Methods. From sixteen knees of different human donors, with four each having a portion of the weight-bearing anterior MFC representing grades: 1) Normal, 2)

Minimal fibrillation, 3) Overt Fibrillation, 3+) Adjacent to Full Thickness Erosion / OA, a ~(3 mm)^3 block of cartilage was imaged with DVI. The output data was reduced to 2-D cross-sections, 3-D models, and movies at standard locations and multiple scales, as well as quantitative bioimage informatic metrics, to assess for matrix disruption and cell organization.

Results. The articular cartilage cell and matrix organization exhibited distinct differences in several of the metrics by grade that indicated loss of zonal segregation in morphology and overall increase in local hypocellularity. Specifically, the proximal angle between nearest neighbor cell with respect to the horizontal was distinct by zone in the normal, but this was lost in the degenerated as cell-to-neighbor orientation tended to become oblique. The increase in clustering in the cells in the degenerated was through increase in number of cells per cluster rather than increase in number of clusters, as the number of clusters decreased in Grades 3/3+.

Discussion. The findings of cell orientation changes with degeneration provide novel structural information and quantification of classically observed histological features. The 3-D analyses delineated that cells grouped into larger and sparsely-spaced clusters with degeneration led to volumes of local hypocellularity, leaving matrix more susceptible to damage. Further analysis using the 3-D bioimage informatics method can reveal more about how cells and matrix synergistically alter with degeneration, and suggest mechanistic links between structure and function, both in cartilage as well as in other tissues and with other imaging techniques.

6.2   Introduction

Normal articular cartilage matrix is organized zonally, with chondrocyte organization reflecting the architecture of the local collagen matrix [1]. The three classically described zones of the articular cartilage are the superficial zone, where cell and matrix are organized tangentially to the articulating surface, the middle zone, where the organization is oblique, and the deep zone, where the organization is perpendicular to the surface. The unique organization of each zone gives them specific mechanical properties: the superficial zone is the smallest by volume, and resists shear through its alignment and the production of lubricating superficial zone protein, the deep zone has a larger and longer collagen fibril network that resists compression, and the middle zone is intermediate between the two [1-6]. The chondrocytes in each zone reflect the matrix organization through the organization of their chondrons, or the basic cellular unit of the cartilage, consisting of one or more cells and the surrounding pericellular matrix [7, 8]. In the deep zone, multi-cell chondrons have the member cells in a columnar arrangement with cells stacked on top of each other superficial to deep. In the superficial zone, the cells in the chondron are arranged tangentially [8].

A hallmark feature of deterioration of the articular cartilage and osteoarthritis (OA), is the alteration in the cellularity and cell disorganization of chondrocytes [9-11]. This loss of organization, particularly formation of regions of local hypocellularity, may contribute to age-related deterioration, as chondrocytes have limited ability to remodel at a distance and can leave matrix farther from cells more susceptible to damage. With aging, the cellularity of the superficial zone decreases apparently due to cell death, but

as osteoarthritis (OA) develops, cellularity may increase due to proliferation and cluster formation [9, 10]. This clustering is localized most frequently near fissures and clefts of the upper cartilage layers. Abnormal cell clusters are distinguished from normal multi-cellular chondrons in their size (>20 cells) and shape (round or ellipsoidal, rather than organized tangentially or into columns) [11, 12]. The member cells of these clusters are also different from those of normal cartilage [13, 14], deviating from the normal flattened (superficial) or rounded (middle-deep) morphology of cells. In addition to the contribution that the reorganization brought by clustering may have to local hypocellularity, alterations of the pericellular matrix territories also may increase susceptibility to deterioration. A change from more type VI collagen in the normal pericellular regions to type X collagen observed in large clusters can result in deterioration of the mechanical properties [15].

The mechanism for formation of the cell clusters, and the complex relationship of the clusters with the breakdown of the articular cartilage matrix, is an ongoing area of study. The initiation of cluster formation prior to the development of OA, and the relative contribution of cell migration and proliferation to this process, is of particular interest to understanding OA pathogenesis [16, 17]. There is evidence that proliferation is a principal mechanism, as clustered cells have been shown to incorporate exogenous H-thymidine [18], and migration may play a role because there are also changes in the chondrocyte cytoskeleton in the clustered cells [14]. To help answer these key questions, the majority of studies to this point have used examination of thin 2-D sections of the cartilage to a limited depth to investigate the chondrons and clusters [10, 19-22]. However, chondrons and clusters are three dimensional structures, and

techniques capable of visualization and measurement in all dimensions, via sampling a large volume rather than area, are needed to see their true morphology and organization.

The lack of 3-D data on cell and matrix organization and cell clustering of articular cartilage in OA is primarily attributable to technological limitations to this point. Most conventional histological techniques use 2-D thin tissue sections are limited by the need for stereological analysis [23]. Spatial 3-D organization of cartilage cells has been quantified using confocal microscopy, with limited ability to see the deep region chondrocytes because of tissue thickness and depth. [24, 25] Recently, new techniques involving the use of hydrogel-linking tissues have been developed which make these tissues visible in 3-D to any depth and at a high resolution, which is promising for the application to articular cartilage [26]. Presently applicable to articular cartilage is Digital Volumetric Imaging (DVI), a method which allows the histological imaging of a 3-D sample automatically and relatively rapidly, has facilitated the procedure of obtaining 3-D quantitative data [27]. Applied to human articular cartilage at various states of degeneration, there is the potential to quantify the morphology, organization, localization of the clusters in 3-D and gather important evidence that links these factors to the matrix changes.

The hypothesis of this study is that an increase in number of cells per cluster is temporally and spatially related to abnormal cell organization and matrix fissuring in early to middle degeneration of human articular cartilage. The aims of this study was to (1) introduce 3-D bioimage informatics analysis to assess the organization of individual cells and cell clusters within human articular cartilage, and (2) to compare results for

four grades of age- and OA-related deterioration to test whether matrix is increasingly susceptible due to local hypocellularity.

6.3   Materials and Methods

6.3.1 Study Design

Samples were harvested from the anterior region of the medial femoral condyle (MFC) from sixteen different human donors, via tissue banks or total knee arthroplasty remnants, with IRB approval (age 58±11 yrs mean±SD, 8 M / 8 F). Samples were selected so that a $(3 \text{ mm})^3$ region of cartilage from the weight-bearing region of the medial femoral condyle, including the articular surface, represented n=4 each of normal, Grade 2 (mild fibrillation), Grade 3 (partial erosion), and Grade 3+ (from OA, but at adjacent cartilage to full erosion) tissue (**Table 6.1**), with an even division of sex within each group. The $(3 \text{ mm})^3$ block of cartilage was extracted from a location on the MFC representing both the worst grade throughout the condyle, and representative of the above macroscopic gross description. Subchondral bone and calcified cartilage was removed from the sample during the extraction.

6.3.2 Sample Preparation

Each sample was fixed with 4% paraformaldehyde. The fixed cartilage blocks were processed for DVI as described previously [7]. Briefly, the samples were stained with Eosin Y for 3 hours and Acridine Orange for 3 days, with citrate buffer washes after each stage, before dehydration with alcohol and treatment with xylenes. After this, they were embedded in Spurr's resin, and the resin block cured at 80°C for 8 hours.

6.3.3 Imaging

The embedded sample block was imaged on a surface imaging machine that serially removed a 0.89 μm section from the sample block and digitally imaged the remaining sample block face through a 10X objective and red and green fluorescence filters, creating a sequence of ~2000 x 2000 x 2000 voxel, RGB (16-bit) images. Only the red and green channels had image data via the digital images taken with the respective fluorescence filters, the blue channel had no data. All together, for each sample, image data encompassing a ~$(1.8 \text{ mm})^3$ volume was obtained at a resolution of 0.89 $(\mu m)^3$/voxel, at a size of ~10 GB for each dataset.

6.3.4 Dataset Preparation

To ensure standardization between all produced datasets, all samples were aligned and cropped to the same dimensions. The sample was aligned so that the surface of the cartilage was level relative to the reference frame of the field of view, and the top of the cartilage surface was at the top of the field of view. In samples that were highly fissured where there were clefts or other pieces of cartilage protruding at the surface, the field of view was placed approximately at the top of the leveled clefts.

6.3.5 Qualitative Description

The datasets were cropped for qualitative visualization with representative slices and 3-D models, to a field of view of 1.2 mm x $(0.6\text{mm})^2$, starting from the ascribed surface. Each 3-D image dataset was visualized at multiple scales in selected 2-D cross-sections, a semi-transparent 3-D render showing matrix fissures and chondrocytes, and movies of serial 2-D sections. Matrix disruption was assessed near

the surface in the 2-D cross sections and 3-D renders by visualizing unstained tissue volumes, representing fissures, as well as absence or presence of cell organization into the three classic zones and the presence of a lamina splendens. Cell organization was assessed by visualizing chondrons and clusters of the zones with the 2-D cross sections, and the semi-transparent 3-D renders. Cells were assessed for the orientation of the chondrons, the maximum chondron/cluster size, the morphology of cells within the chondron/cluster (flat or ellipsoidal), and the proximity of large chondrons or clusters to matrix irregularites such as fissures.

6.3.6 3-D Bioimage Quantitative Analysis

For quantitative analysis, full datasets were cropped down for the quantitative analysis to a volume of (0.9 mm superficial-deep) x $(0.6 \text{ mm})^2$, starting from the ascribed surface. This cropped region was divided by superficial-deep into three (0.3 mm) deep zones, representing superficial (SZ), middle (MZ), and deep (DZ) zones, starting from the surface and each sequentially deeper, and then analyzed with a custom MATLAB script for the metrics listed in **Tables 6.2-3** and **Figure 6.4**. The grades and zones were compared with a two-way ANOVA with Tukey post-hoc tests, and the data was reported, separated by zone, as mean ± SD in **Table 6.4**. A one-way ANOVA comparison by sex was also done to verify that there was no effect of gender on the metrics.

6.3.6.1 Thresholding

The matrix and cell nuclei were thresholded separately from the image data, the former based on the green channel only, and the latter on a combination of local thresholding of the red and the green when local regions of overstaining caused oversaturation of the red. Both thresholds were determined by calibration of the script settings on a sample slice from the cropped dataset, on an individual sample basis.

Matrix was identified using a global threshold of the green channel, where if a voxel in the green channel exceed a certain brightness, it was counted as matrix voxel. Cell nuclei voxels were first counted using local mean-C thresholding of the red channel. In mean-C thresholding, for each slice, a local 2-D neighborhood was sampled around the voxel of interest. If the voxel's brightness exceeded the average of the local neighborhood by a certain percentage, it was counted as a nuclei voxel. As a secondary method for determining the nuclei voxels, if the local neighborhood's average brightness exceeded a certain high threshold, indicating oversaturation, the bright green voxels disconnected from the largest green object, or nuclei separated from matrix by intercellular or pericellular area, were used. For the remainder of the quantitative analysis, the identified cell nuclei are considered equivalent to a single cell, so that the assumption was made that the chondrocytes were singly nucleated.

6.3.6.2 Cell Metrics

The identified nuclei voxels were connected using a flood fill algorithm, to group them into individual nuclei. A size exclusion algorithm was done to filter out this set of nuclei based on size, to remove those that may have been a result of noise (too small) or large overstained regions of the matrix (too large). The final set of nuclei

resulting from this procedure was taken to be the cell set for that sample, so that all identified cells were stored as point locations based on the centroid of the nuclei. Each cell was given a numerical identifier in the script's data structure, the location or centroid was stored, as well as certain properties of the individual nuclei, including its nearest neighbor cell based on 3-D distance, the vector coordinates and angle with respect to its nearest neighbor, as well as the identifier for the cluster of which it was determined to be a member, discussed below. Finally, the asymmetry index of the nuclei was calculated using the below formula:

$$As\_Ce_{[i]} = \sum_{v=1}^{n} \frac{(x_v - x_c)^2 + (y_v - y_c)^2}{2(z_v - z_c)^2} \qquad (6\text{-}1)$$

where v comprises all the voxels in the cell i from 1-n, and z_v is the z-coordinate (superficial-deep) of the voxel, z_c is the z-coordinate of the centroid of cell i, x_c, x_v, y_c, y_v, are the respective coordinates in the non-vertical axes. Thus, this is a metric of how asymmetric the cell is: 1 indicates a perfectly balanced or spherical cell, >1 indicates a cell elongated horizontally, <1 indicates a cell elongated vertically.

6.3.6.3 Cluster Metrics

The identified cells were grouped into cluster based on two criterions: (1) distance between centroids is less than a certain threshold, (2) both cells lie within the same pericellular pocket. The pericellular pockets (each larger pocket usually comprising the individual chondron of several cells) were identified using a global threshold of the green channel (higher than the setting used to identify matrix voxels. The distance threshold wherein cells were considered to be members of the same

cluster was 10 µm, regardless if they were in the same pericellular pocket. If the cells were between 10-20 µm apart, they were considered to be in the same cluster if they were also in the same pericellular pocket. Finally, any cells with a mutual cluster member were considered to be in the same cluster; in other words, if cell A was clustered with cell B and cell B was clustered with cell C by the above criteria, cell A and C were in the same cluster, regardless of the distance or presence in the same pocket between A and C.

Each of the identified clusters was given a numerical identifier, and this identifier was also reported and stored in each individual cluster data structure. By this "cluster" definition, there were some clusters consisting of only one cell, but some of the cluster metrics in this section and below required a cluster to have at least two cells for counting purposes, described in detail below. Each cluster data structure stored the identifiers of all its member cells as well as certain properties of the cluster, including the size or number of cells in that cluster, the centroid of the cluster which was the mean of the centroids of all member cells, and the asymmetry index, which was calculated using the same formula (1) but used the centroids of the member cells rather than the individual voxels as v, and (x_c, y_c, z_c) was the centroid of the cluster. All cell and cluster data structures were passed to the tissue level structure, described below, for description of these metrics on an average tissue depth basis.

6.3.6.4 Tissue Metrics

The matrix per volume, by depth, was calculated by summing all of the number of voxels to a certain depth that is determined to be matrix. To represent this in a by

depth basis, tissue volume was expressed as the function $TV(z)$, where this included to count all voxels from the surface (0) to the depth (z). Thus, calculations of specific regions can be done by subtracting the expression from the deeper border to the superficial border; for example the tissue volume from depth z_1 to z_2 is $TV(z_1)$ - $TV(z_2)$. The fissure volume density, $\%_{fis}$, was calculated from the tissue volume as

$$\%_{fis} = \frac{UV(z)}{TV(z) + UV(z)} \tag{6-2}$$

where $UV(z)$ is unstained volume in the dataset (any voxel not counted as a matrix voxel). To quantify local matrix hypocellularity, the percentage of matrix voxels within a certain distance from a nuclei, 5, 10 and 15 μm, was reported as $\%_{mat\text{-}5\mu m}(z)$, $\%_{mat\text{-}10\mu m}(z)$, $\%_{mat\text{-}15\mu m}(z)$ respectively.

Using the cell and cluster data structures, the number and densities of cells and clusters were calculated on a depth basis. These were the cell number, $Ce_n(z)$, cluster number (only counting "clusters" with 2 or more cells) $Cl_m(z)$, cell number density $N_v\_Ce(z)$ ($Ce_n(z)$ / $TV(z)$), and cluster number density ($Cl_m(z)$ / $TV(z)$). The cell metrics described in **6.3.6.2** were reported as the average of all cells to the certain depth, as a function of depth, as mean cell proximity $\mu_{px}(z)$, mean cell proximal angle $\mu_{px\_ang}(z)$, mean cell asymmetry $\mu_{As\_Ce}(z)$. The cluster metrics in **6.3.6.3** were reported in a similar way. For this, the average metrics for all clusters with centroid up to the depth z and containing two or more cells were reported: mean cluster size $\mu_{Ce\_Cl}(z)$ and mean cluster asymmetry $As\_Cl(z)$.

6.4   Results

6.4.1 Characteristic Patterns of Matrix Fissuring and Cell Organization

The standardized 2-D slices and 3-D renders for the Grades 1-3+ samples are shown in **Fig. 6.1**.

Grade 1 samples had minimal surface irregularity (**Fig. 6.1-A1**). Grade 2 samples also showed minimal surface irregularity (**Fig. 6.1-A2**), with occasional perturbations or undulations. In Grade 1 and 2 samples, the lamina splendens was evident. In contrast, Grade 3 and 3+ samples (**Fig. 6.1-A3, 6.1-A4**), had large fissures throughout the surface visible in the 2-D sections and 3-D renders and no lamina splendens. Near the surface, the fissures (absent area of tissue) covered >50% of the volume in several samples (**Fig. 6.1-C3, 6.1-C4**).

In Grade 1 samples, the classical morphology of individual cells was evident in the superficial, middle and deep zones. Cells transition from being flattened and aligned parallel to the surface, to aligned obliquely (**Fig. 6.1-B1**), to being organized vertically into approximately vertical columns. Grade 2 (**Fig. 6.1-B2**), also had the organization into the three zones with little difference from Grade 1. In contrast, in the Grade 3 and 3+ samples, the cell features typical of classical superficial zones was absent (**Fig. 6.1-B3, 6.1-B4**), and in the middle and deep zones, cell organization was abnormal, in that the organization was interrupted both by abnormal cell clusters throughout the samples or regions that were devoid of cells (**Fig. 6.2-F2**). In some samples, zonal organization of the middle and deep zones were totally lost. Cross sections and 3-D visualizations of cell clusters in the superficial (or "near-fissure" zone in the Grade 3 sample) (**Fig. 1-D(1-4)-S**), middle (**Fig. 1-D(1-4)-M**), and deep

(**Fig. 1-D(1-4)-D**), showed distinct differences between normal and degenerated. The Grade 3 sample had very large clusters in the more superficial region, close to the fissures, and medium sized clusters in the deeper regions. In the Grade 1 sample, cells in the superficial zone were organized tangentially and occasionally grouped into 2-3 cell chondrons. In the middle zone, there was some organization of cell clusters in a direction oblique to the surface, and chondrons were at most 2-3 cells. In the deep zone cells were organized in columns perpendicular to the surface and again cells that were spaced very close together were limited to groups of 2-3. The cells in the Grade 3-3+ samples tended to be about twice as large (hypertrophic) than in the Grade 1-2 samples. Grade 3 and 3+ samples had enlarged chondron structures with increased numbers of cells, typically medium (5-10) to very large (30+), and ellipsoidal in geometry.

6.4.2 Quantitative Analysis

The articular cartilage cell and matrix organization exhibited distinct differences in several of the metrics by grade, that indicated loss of zonal segregation in morphology and overall increase in local hypocellularity. A graphical description of the trends in organization is given in **Figure 6.5**, and the results of the analysis are summarized in **Table 6.4**. Movies of representative samples of each grade showing serial sections of the 3-D data, demonstrating the organizational changes in each of the three zones, were created.

6.4.2.1 Cells

Cells tended to be more asymmetrical (flattened) in the superficial zones. Overall, cells from all zones and metrics had an asymmetry index of less than 0.5, indicating that cells tend to be flattened in the horizontal axis, especially in the superficial zone. From Grade 1 up to Grade 3+, the gradient in asymmetry index between the superficial-deep zones was gradually lost (0.19/0.25/0.32 S/M/D in Grade 1 to 0.23/0.27/0.27 in Grade 3+).

6.4.2.2 Clustering, Cell Proximity and Cell Organization

Mean cell cluster size increased from superficial to deep and from Grade 1 to Grade 3+. In Grade 1, mean cells per cluster was 2.75/2.78/3.10 S/M/D, in Grade 3+ 6.60/6.17/4.62. Thus, the superficial and middle zone cluster sizes were more affected by the factor of grade than the deep zone, as it increased about 2.5-fold in the former and 1.5 fold in the latter. The asymmetry index of the clusters had a clear distinction between zones (0.31/0.67/0.41 S/M/D in Grade 1). The asymmetry index of all zones increased with grade, and roughly doubled from Grade 1 to Grade 3+ (0.71/1.32/2.02 in Grade 3+), indicating clusters become more vertically oriented with increasing grade.

Cell proximity, or average distance to the closest cell, did not show a significant change by grade, and was only subtly higher in superficial zone than in middle or deep. The percentage of paired cells, or percentage of cells that were mutual nearest neighbors, also showed little difference by grade and zone. However, the angle with respect to the horizontal to the nearest neighbor had a clear differentiation by zone in the normal, from horizontal (0) towards oblique (45) (19.3/27.7/37.0 S/M/D) and a loss of this differentiation with increasing grade (33.4/37.8/38.8 S/M/D in Grade 3+).

This mean angle was significantly different between normal, Grade 3 (p<0.05), and Grade 3+ (p<0.01) in the superficial zone, and between normal and Grade 3 (p<0.05) in the middle zone.

6.4.2.3 Cell and Cluster Density

Cell density was similar across all grades, but there were differences in the zonal distinctions with increasing grade. In the superficial zone, Grade 3 was hypocellular compared to normal (20.4 vs. 31.7), but Grade 3+ had a similar cellularity to normal (31.6). The superficial zone had more cellularity than the middle and deep zones in normal (31.7/19.3/17.6 S/M/D) and Grade 2 (38.9/24.3/23.4), but this distinction was lost in Grades 3 (20.4/23.8/28.4) and Grade 3+ (31.6/30.8/24.9). Cluster density was higher in the normal superficial zone (8.36) and Grade 2 (9.44) than Grade 3 (4.18, p<0.05) and Grade 3+ (4.23, p<0.05). The middle and deep zones had similar cluster density throughout all grades.

6.4.2.5 Matrix Local Cellularity and Fissuring

The trend in percentage of matrix voxels that were within set distances from the nearest cell centroid (5, 10, 15 μm) were indicative of increasing local hypocellularity with grade in the superficial zone. The middle and deep zones typically did not show a difference between grades. For the percentage of superficial zone matrix within 5 μm of nearest cell, the Grades 1, 2, 3 and 3+ values were 1.47, 1.12, 0.61 and 0.96%, respectively. For 10 μm, the values were 10.63, 9.40, 4.50 and 6.08%. For 15 μm, the values were 29.51, 28.90, 13.73, and 16.67%. Thus, Grade 3 superficial zone had the

most matrix displaced from the nearest matrix by percentage, with a small increase from this in Grade 3+, but both of these were quite lower than Grade 1/Grade 2 levels, especially when considering distances that were on the scale of the size of an individual cell (15 μm). The percentage of dataset volume that was fissures (unstained) increased from Grade 1 to Grade 3+, with the largest increase being in the superficial zone.

6.5   Discussion

Both qualitatively, and quantitatively through 3-D bioimage informatics, the findings here represent novel structural information about the organization of chondrocytes and matrix in normal adult human cartilage, demonstrate how these alter with degeneration, and suggest potential mechanisms for how organizational changes can lead to loss in function. Qualitatively, the visualization of cartilage DVI established characteristic 3-D features of cartilage in deterioration and OA. The cell clustering features include large clusters, especially at near-surface regions, ellipsoidal shaped clusters, and hypertrophic cells. There was spatial correspondence of large cell with fissures, consistent with previous descriptions of cluster localization. In the 3-D biomage informatics analysis, the findings of cell orientation and clusters being specialized as flattened/horizontal and closely packed in superficial and middle zones to isotropic and more loosely packed in the deep zone, and the loss of this pattern in Grade 3 and Grade 3+, quantifies features that have been classically described in histology. The 3-D analyses delineated that cells grouped into larger and more sparsely spaced but fewer clusters with degeneration. That is, there was a trend away from many chondrons with two or three cells and towards few large clusters with five or more cells. This led to volumes of local hypocellularity leaving matrix susceptible to damage with limited remodeling, and this hypocellularity did correspond with more fissuring.

The study design had some limitations. Samples for Grades 1-3 were divided into grades based on how a surgeon scored them from gross or surface appearance, but this did not always reflect the state of the cartilage underlying. This may have been

reflected in the observance for Grade 2 that the cell organization was mostly normal, but there were small disruptions or fibrillation of the surface. However, the grading scheme used (modified Outerbridge) is a well-established and clinically relevant means of scoring the cartilage from gross appearance and gives a reasonably accurate way of estimating the health of cartilage without having to delve into more invasive means [28, 29]. Additionally, the Grade 2 samples show clear trends towards abnormality in the quantitative analysis, with many of the metrics being intermediate between Grade 1 and the Grade 3/3+ values. Regarding the sampling size, because of the small region visible from DVI, the analysis for each donor sample may have been enhanced by taking multiple samples per donor. However, it is reasonable to believe the tissue is relatively homogenous across a condyle that has been similarly graded throughout, as is evident from 2-D histology sections. Additionally, in the given study design, the grade of the cartilage block was always chosen to reflect the grade of the specific group being investigated. Finally, the number of objects sampled was on the order of 10^4 for cells and 10^3 for clusters per sample per zone, enough to be statistically significant. Another limitation was that the delineation of zones (superficial or near fissures, middle, deep) may not reflect the precise separation as these may vary by sample, and was instead taken as a set depth to standardize analysis across datasets. However, using set depths may be more effective for zone delineation as a whole than using a variable amount or percentage of total thickness for each sample as the superficial zone seems to be relatively constant at this anatomical location. From the overviews given in **Fig. 6.1**, the zonal separation with this standard amount seems to be a good reflection of the organizational differences in the classically described S/M/D zones.

In comparison to other methods of visualizing the cartilage, including both classic 2-D histology and newer methods that can extend deeper into the tissue, DVI provides good depth of view and resolution. Compared with 2-D histology, DVI allows visualization of the cell clusters and chondrons in three dimensions, which is important because they can extend in all dimensions in (superficial-deep, medial-lateral, anterior-distal). Histology of thin 2-D sections can also be expanded to 3-D through conventional serial sectioning; however, this is always limited by accuracy and skill of the histotechnician and can be time consuming. Confocal microscopy allows visualization of the cartilage in simulated 3-D, with a range of depth visible from a single projection, and the depthwise location of cells within the projection inferable from relative intensity. However, this type of visualization, while superior to 2-D histology, does not allow a true view of 3-D structure, and the depth of view is a fraction of DVI. Recently, a technique called CLARITY has been developed that allows visualization of tissue that has been treated to be made translucent, except for certain components which are linked to hydrogels in the tissue. This technique is promising and provides 3-D visualization to a depth and at a resolution equivalent or better than DVI, but an effective method of treating and preparing articular cartilage for this has yet to be developed.

The spatial relationship between cell clustering, local hypocellularity, and matrix fissuring, suggest there may be a causative link. Large clusters in the superficial zones have distinct pericellular regions that do not intersect the surface of the cartilage, but are often encased within the individual clefts of the cartilage. In contrast, cellularity away from the fissures decreases, suggesting that there was a net relocation of cells

towards the fissures. Thus, the formation of large clusters in these fissured regions could be a response to facilitate diffusion from the synovial fluid to the member cells in regions of damage. Another possibility is that the cellularity of the tissue gradually decreases overall, leading to breakdown in the matrix due to local hypocellularity and insufficient cell-matrix interaction, as well as rapid proliferation of cells in certain chondrons to compensate for the overall loss of cells, leading to some "super-clusters". One key finding of this study was that the number of multi-cellular clusters actually decreases in the superficial zone with degeneration, but that is counter-acted by an increase in cells per cluster, leading to relatively similar cellularity overall. The question of whether large clusters arise through proliferation and migration may need more longitudinal data to answer, although the encasement of the groups of cells into large pericellular pockets, including some multi-nucleated cells, is suggestive of the former. Further investigation, such as quantification of cluster size with proximity to matrix lesions, may give more insight into whether cell aggregation and local hypocellularity are contributing factors to formation of sites of cartilage erosion.

The method presented here to reduce the 3-D DVI datasets to metrics, is a foundational tool for a new type of 3-D bioimage informatic analysis. In this analysis, each voxel is classified to either nuclei (cell), matrix, or fissure (unstained) using image processing. The same general procedure can be used to convert other tissue image information into cells, matrix, and other structures, and even differentiate between cell types if the imaging technique can produce enough contrast between them. Once the image data is reduced in this way, a variety of different metrics can be calculated, including all those demonstrated in this study, such as geometric (morphology of

objects), spatial/organization (relative distribution of objects with each other, clustering), density (number of objects per volume, both local and overall). This can be used to examine the organizational differences in tissues of different disease states to pinpoint the specific abnormalities inherent in the cells and tissue, as in the present study, or applied to a longitudinal analysis of either developing or aging tissue, to gain a view of cell and tissue fates. Thus, the analysis presented here can be the foundation for new ways to utilize the resolution provided by recent technological breakthroughs, to assess whole tissues with tracking down to the morphology and positions of individual cells, and is in theory limited only by the restrictions of the imaging technique used, as well as computational power.

The technology and analysis techniques demonstrated here allow the visualization of 3-D morphology of cartilage features such as cell clusters. The qualitative and quantitative descriptions that can be obtained from this visualization, of cell and cluster morphology, organization, and localization, give insight into the role of cell proliferation in the pathogenesis of osteoarthritis with respect to macroscopic changes. The qualitative and semi-quantitative descriptions and visualization here demonstrate that a comprehensive 3-D characterization of the cells, clusters, and matrix in human articular cartilage is feasible, given sufficient computing resources for a specified field of view, with an analysis that ensures no structural data in any dimension is missed. Finally, the metric-based reduction of the 3-D data presented here is translatable to similar imaging systems, and can potentially provide a view of cells and their fates in other tissues, in development, homeostasis, aging and disease.

6.6 Acknowledgments

Chapter 6 is being prepared for submission to *PLoS One*. The dissertation author is the primary investigator and thanks co-authors Van Wong, Esther Cory, and Dr. William Bugbee for their contributions.
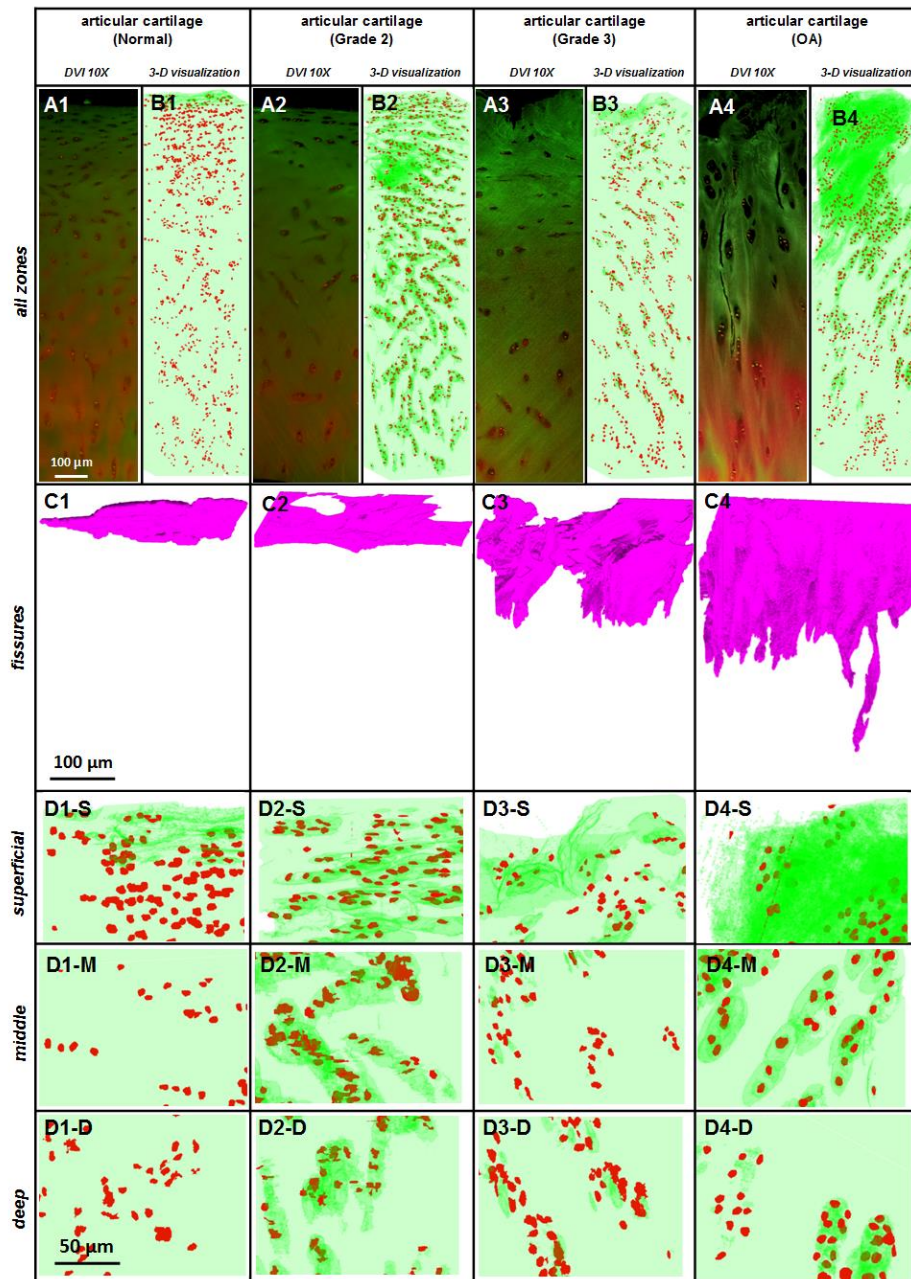
Figure 6.1: DVI and 3-D Model Visualizations of Chondrocyte Organization and Fissures in Cartilage. (A1-A4) DVI tangential sections of representative samples articular cartilage, Grades 1-3+. (B1-B4) Cartilage 3-D visualizations showing the organization of the chondrocytes at both medium power and (D1-D4) focused regions showing the superficial (S), middle (M), and deep (D) zones. (C1-C4) Visualization of the fissures in representative samples, as a colorized 3-D volume.
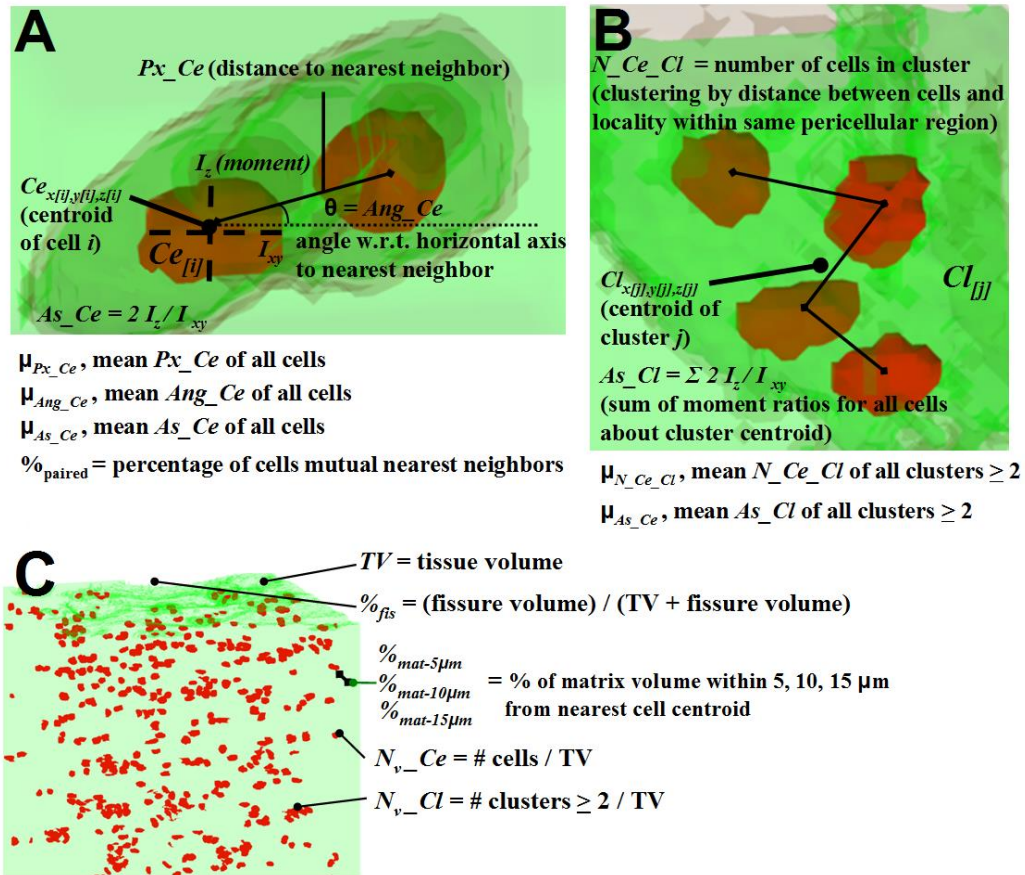
Figure 6.2: Cell, Cluster and Tissue Metric Definitions. Quantification of cell metrics in schematized articular cartilage tissue, with identification of (A) individual cells (Ce[i]) and associated centroids, moments, proximity and angle to nearest cell, (B) cell clusters (Cl[j]), and centroids, moments and cluster sizes, and (C) determination of depth-varying cell density (N_V_Ce), cell cluster density (N_V_Cl), and fissure volume density.

Table 6.1: Sample Groups for Cartilage Bioimage Informatics Analysis.

Grade	Description	n
1	normal: no fibrillation or erosion	2 M / 2 F
2	mild fibrillation	2 M / 2 F
3	partial erosion	2 M / 2 F
4	diagnosed OA, cartilage adjacent to region of full thickness erosion	2 M / 2 F

Table 6.2: Cell and Cell Cluster Metrics. Metrics of cell and cluster densities.

Classification	Metric	Abbreviation	Description
cell	(identifier)	$Ce_{[i]}$	i is subscript indicating the number of the cell (i = 1, 2, … n)
	centroid	$Ce_{x[i]}$, $Ce_{y[i]}$, $Ce_{z[i]}$	position of cell in x-y-z [μm], z-relative to the surface of cartilage, x-y relative to a set point on corner of dataset
	cluster	$Cl\_Ce_{[i]}^{cl}$	cluster that the cell is a member of (equivalent to [j] in $Cl_{[j]}$)
	nearest neighbor	$Ce_{[i]}^{px}$	the nearest cell to the current cell, by distance (value is an identifier, i.e. $Ce_{[i1]}^{px} = Ce_{[i2]}$ means nearest to cell-i1 is cell-i2)
	nearest neighbor vector	$Ce_{[i]}^{px}<x,y,z>$	vector to nearest cell, i.e. $< Ce_{x[i]}^{px} - Ce_{x[i]}, Ce_{y[j]}^{px} - Ce_{y[i]}, Ce_{z[k]}^{px} - Ce_{z[i]}>$
	asymmetry index	$As\_Ce_{[i]}$	moment of all member voxels about centroid in z-axis * 2, divided by moment of all member voxels about centroid in x and y axes
cell cluster	(identifier)	$Cl_{[j]}$	group of cells with sufficient proximity to each other. i is subscript indicating number of the cluster (i = 1, 2, … n)
	centroid	$Cl_{x[j]}$, $Cl_{y[j]}$, $Cl_{z[j]}$	position of cluster centroid in x-y-z [μm], z-relative to the surface of cartilage, x-y relative to a set point on corner
	size	$N\_Ce\_Cl_{[j]}$	number of cells that cluster contains (determined by how many $Ce_{[i[}^{cl}$ are assigned to the cluster)
	asymmetry index	$As\_Cl_{[i]}$	moment of all member cell centroids about cluster centroid in z-axis * 2, divided by moment of all member cell centroids about cluster centroid in x and y axes
	cell	$Ce\_Cl_{[i,j]}$	ith cell of the cluster

Table 6.3: Tissue Organization Metrics. Metrics of mean cell and cluster properties in tissue.

Classification	Metric	Abbreviation	Description
tissue	tissue volume	$TV(z)$	volume of tissue (matrix + cells, i.e. stained material) in [mm^3] as a function of depth z from surface
	cell number	$Ce_n(z)$	total number of cells, as a function of depth
	cell density	$N_v\_Ce\ (z)$	$Ce_n(z) / TV(z)$ as a function of depth
	cluster number	$Cl_m(z)$	total number of clusters to depth, only counting $N\_Ce\_Cl_{[j]} \geq 2$
	cluster density	$N_v\_Cl(z)$	$Cl_m(z) / TV(z)$
	mean cluster size	$\mu_{N\_Ce\_Cl}\ (z)$	$\Sigma N\_Ce\_\ Cl_{[j]} / Cl_m(z)$ (for all clusters with $Cl_{z[j]} <= z$ and $N\_Ce\_Cl_{[j]} \geq 2$)
	mean cell proximity	$\mu_{px}(z)$	$\Sigma \ \|\|Ce_{[i]}^{px}<x,y,z>\|\| / Ce_n(z)$ (for all cells with $Ce_{z[i]} <= z$)
	mean cell proximal angle	$\mu_{px\_angle}(z)$	$\Sigma \ arctan(Ce_{[i]}^{px}<x,y,z>/\|\|Ce_{[i]}^{px}<x,y,z>\|\|) / Ce_n(z)$ (for all cells with $Ce_{z[i]} <= z$), or the mean angle between cells and their nearest neighbors
	percentage paired cells	$\%_{paired}(z)$	percentage of cells where mutually, $Ce_{[i1]}^{px} = Ce_{[i2]}$ and $Ce_{[i2]}^{px} = Ce_{[i1]}$
	mean cell asymmetry	$\mu_{As\_Ce}(z)$	$\Sigma As\_Ce_{[j]} / Ce_m(z)$ (for all cells with $Ce_{z[j]} <= z$)
	mean cluster asymmetry	$\mu_{As\_Cl}(z)$	$\Sigma As\_Cl_{[j]} / Cl_m(z)$ (for all clusters with $Cl_{z[j]} <= z$ and $N\_Ce\_Cl_{[j]} \geq 2$)
	fissure vol density	$\%_{fis}(z)$	percentage of fissure volume with respect to total volume of entire dataset
	matrix proximity 5 μm	$\%_{mat-5\mu m}(z)$	percentage of matrix volume that is within 5 μm in distance to the centroid of the closest nuclei
	matrix proximity 10 μm	$\%_{mat-10\mu m}(z)$	percentage of matrix volume that is within 10 μm in distance to the centroid of the closest nuclei
	matrix proximity 15 μm	$\%_{mat-15\mu m}(z)$	percentage of matrix volume that is within 15 μm in distance to the centroid of the closest nuclei

Table 6.4: 3-D Bioimage Informatics of Human Articular Cartilage. Cell and matrix organization metrics of chondrocytes, metrics of matrix volume density, cell and cluster densities, and mean member cell and cluster properties are reported. Reported as mean $\pm$ SD.

	Normal	Grade 2	Grade 3	Grade 3+
	Superficial, Middle, Deep	Superficial, Middle, Deep	Superficial, Middle, Deep	Superficial, Middle, Deep
Cell Density (N_v_Ce) [1000 / mm^3]	31.7 ± 12.6 19.3 ± 2.7 17.6 ± 0.6	38.9 ± 13.8 24.3 ± 5.6 23.4 ± 5.8	20.4 ± 3.3 23.8 ± 7.7 28.4 ± 9.6	31.6 ± 18.6 30.8 ± 19.3 24.9 ± 11.0
Cluster Density (N_v_Cl) [1000 / mm^3]	8.36 ± 3.13 4.43 ± 1.28 3.62 ± 0.35	9.44 ± 2.88 5.61 ± 1.29 4.71 ± 0.96	4.18 ± 1.91 4.38 ± 1.66 5.00 ± 1.17	4.23 ± 1.60 4.23 ± 1.37 4.03 ± 0.99
Cluster Size $\mu_{N\_Ce\_Cl}$ [#]	2.75 ± 0.18 2.78 ± 0.18 3.10 ± 0.70	3.41 ± 0.73 3.74 ± 0.52 4.40 ± 1.05	4.89 ± 3.15 5.08 ± 2.33 4.42 ± 0.69	6.60 ± 4.16 6.17 ± 2.82 4.62 ± 1.73
Cell Proximity μ_{Px_Ce} [μm]	14.4 ± 1.5 13.4 ± 1.3 12.5 ± 0.6	13.3 ± 1.0 11.9 ± 2.0 10.6 ± 2.5	13.7 ± 1.7 11.2 ± 1.2 10.3 ± 0.6	13.9 ± 2.8 12.2 ± 1.8 12.5 ± 1.0
Nearest Cell Angle μ_{Ang_Ce} [°]	19.3 ± 2.6 27.7 ± 4.8 37.0 ± 4.6	20.8 ± 1.4 31.3 ± 6.5 37.3 ± 7.0	30.8 ± 8.0 40.2 ± 5.3 43.8 ± 6.2	33.4 ± 3.8 37.8 ± 3.4 38.8 ± 3.9
Paired Cells $\%_{paired}$ [%]	69.0 ± 2.3 71.4 ± 3.7 67.1 ± 0.77	69.2 ± 2.7 67.6 ± 2.8 65.7 ± 4.7	66.1 ± 8.1 64.6 ± 7.6 62.7 ± 3.6	63.5 ± 5.1 63.0 ± 5.1 62.4 ± 3.2
Cell Asymmetry Index μ_{As_Ce} [ ]	0.19 ± 0.05 0.25 ± 0.08 0.32 ± 0.08	0.28 ± 0.14 0.29 ± 0.15 0.36 ± 0.18	0.24 ± 0.04 0.26 ± 0.09 0.32 ± 0.16	0.23 ± 0.06 0.27 ± 0.07 0.27 ± 0.13
Cluster Asymmetry Index μ_{As_Cl} [ ]	0.31 ± 0.05 0.67 ± 0.31 1.41 ± 0.63	0.18 ± 0.04 0.65 ± 0.44 1.21 ± 0.41	0.82 ± 0.66 2.06 ± 1.25 2.48 ± 1.77	0.71 ± 0.42 1.32 ± 0.28 2.02 ± 0.42
Fissure Volume Density $\%_{fissure}$ [%]	7.70 ± 8.62 0.00 ± 0.00 0.00 ± 0.00	10.59 ± 8.71 3.87 ± 7.31 2.33 ± 3.97	20.12 ± 17.88 5.83 ± 9.05 4.83 ± 8.98	23.01 ± 17.37 6.35 ± 8.65 3.02 ± 5.68
Matrix Proximity 5 μm % $\%_{mat-5μm}$ [%]	1.47 ± 0.59 0.98 ± 0.11 0.88 ± 0.03	1.12 ± 0.17 0.95 ± 0.44 0.98 ± 0.43	0.61 ± 0.38 0.90 ± 0.32 1.20 ± 0.38	0.96 ± 0.54 1.36 ± 0.77 1.26 ± 0.47
Matrix Proximity 10 μm % $\%_{mat-10μm}$ [%]	10.63 ± 4.31 6.90 ± 0.86 5.94 ± 0.26	9.40 ± 1.48 6.74 ± 2.70 6.39 ± 2.20	4.53 ± 1.98 5.86 ± 1.43 7.33 ± 1.81	6.08 ± 3.10 8.53 ± 4.08 8.10 ± 2.55
Matrix Proximity 15 μm % $\%_{mat-15μm}$ [%]	29.51 ± 11.01 19.05 ± 2.77 15.51 ± 0.81	28.90 ± 5.72 19.39 ± 6.84 17.25 ± 4.53	13.73 ± 5.04 15.50 ± 2.56 17.62 ± 3.18	16.67 ± 7.23 21.33 ± 8.43 20.24 ± 5.76

6.7   References

1.   Poole AR, Kojima T, Yasuda T, Mwale F, Kobayashi M, Laverty S. Composition and structure of articular cartilage: a template for tissue repair. Clin Orthop Relat Res 2001: S26-33.

2.   Mow VC, Gibbs MC, Lai WM, Zhu WB, Athanasiou KA. Biphasic indentation of articular cartilage--II. A numerical algorithm and an experimental study. J Biomech 1989;22: 853-61.

3.   Maroudas A. Physicochemical Properties of Articular Cartilage. In: Freeman MAR, editor. Adult Articular Cartilage. 2nd ed. Tunbridge Wells, England: Pitman Medical; 1979, p. 215-90.

4.   Schinagl RM, Gurskis D, Chen AC, Sah RL. Depth-dependent confined compression modulus of full-thickness bovine articular cartilage. J Orthop Res 1997;15: 499-506.

5.   Eggli PS, Hunziker EB, Schenk RK. Quantitation of structural features characterizing weight- and less-weight-bearing regions in articular cartilage: a stereological analysis of medial femoral condyles in young adult rabbits. Anat Rec 1988;222: 217-227.

6.   Flannery CR, Hughes CE, Schumacher BL, Tudor D, Aydelotte MB, Kuettner KE, Caterson B. Articular cartilage superficial zone protein (SZP) is homologous to megakaryocyte stimulating factor precursor and Is a multifunctional proteoglycan with potential growth-promoting, cytoprotective, and lubricating properties in cartilage metabolism. Biochem Biophys Res Commun 1999;254: 535-41.

7.   Jadin KD, Bae WC, Schumacher BL, Sah RL. Three-dimensional (3-D) imaging of chondrocytes in articular cartilage: growth-associated changes in cell organization. Biomaterials 2007;28: 230-9.

8.   Youn I, Choi JB, Cao L, Setton LA, Guilak F. Zonal variations in the three-dimensional morphology of the chondron measured in situ using confocal microscopy. Osteoarthritis Cartilage 2006;14: 889-97.

9.   Collins DH. The Pathology of Articular and Spinal Disease. London: Arnold; 1949.

10.   Mankin HJ, Dorfman H, Lipiello L, Zarins A. Biochemical and metabolic abnormalities in articular cartilage from osteoarthritic human hips. II. Correlation of morphology with biochemical and metabolic data. J Bone Joint Surg Am 1971;53-A: 523-37.

11.   Lee GM, Paul TA, Slabaugh M, Kelley SS. The incidence of enlarged chondrons in normal and osteoarthritic human cartilage and their relative matrix density. Osteoarthritis Cartilage 2000;8: 44-52.

12.   Goyal N, Gupta M, Joshi K, Nagi ON. Osteoarthritic femoral articular cartilage of knee joint in man. Nepal Med Coll J 2006;8: 88-92.

13.   Rolauffs B, Williams JM, Grodzinsky AJ, Kuettner KE, Cole AA. Distinct horizontal patterns in the spatial organization of superficial zone chondrocytes of human joints. J Struct Biol 2008;162: 335-44.

14.   Kouri JB, Jimenez SA, Quintero M, Chico A. Ultrastructural study of chondrocytes from fibrillated and non-fibrillated human osteoarthritic cartilage. Osteoarthritis Cartilage 1996;4: 111-125.

15.   Hambach L, Neureiter D, Zeiler G, Kirchner T, Aigner T. Severe disturbance of the distribution and expression of type VI collagen chains in osteoarthritic articular cartilage. Arthritis Rheum 1998;41: 986-96.

16.   Morrison EH, Ferguson MW, Bayliss MT, Archer CW. The development of articular cartilage: I. The spatial and temporal patterns of collagen types. J Anat 1996;189: 9-22.

17.   Chi SS, Rattner JB, Matyas JR. Communication between paired chondrocytes in the superficial zone of articular cartilage. J Anat 2004;205: 363-70.

18.   Lee DA, Bentley G, Archer CW. The control of cell division in articular chondrocytes. Osteoarthritis Cartilage 1993;1: 137-46.

19.   Pfander D, Körtje D, Weseloh G, Swoboda B. Cell proliferation in human arthrotic joint cartilage. Z Orthop Ihre Grenzgeb 2001;139: 375-81.

20.   Telhag H. Mitosis of chondrocytes in experimental "osteoarthritis" in rabbits. Clin Orthop Relat Res 1972;86: 224-9.

21.   Rotzer A, Mohr W. 3H-thymidine incorporation into chondrocytes of arthritic cartilage. Z Rheumatol 1992;51: 172-6.

22.   Rothwell AG, Bentley G. Chondrocyte multiplication in osteoarthritic articular cartilage. J Bone Joint Surg Br 1973;55: 588-94.

23.   Saito M, Sasho T, Yamaguchi S, Ikegawa N, Akagi R, Muramatsu Y, Mukoyama S, Ochiai N, Nakamura J, Nakagawa K, Nakajima A, Takahashi K. Angiogenic activity of subchondral bone during the progression of osteoarthritis in a rabbit anterior cruciate ligament transection model. Osteoarthritis Cartilage 2012;20: 1574-82.

24. Amini S, Veilleux D, Villemure I. Three-dimensional in situ zonal morphology of viable growth plate chondrocytes: a confocal microscopy study. J Orthop Res 2011;29: 710-7.

25. Stok KS, Muller R. Morphometric characterization of murine articular cartilage--novel application of confocal laser scanning microscopy. Microsc Res Tech 2009;72: 650-8.

26. Chung K, Deisseroth K. CLARITY for mapping the nervous system. Nature methods 2013;10: 508-13.

27. Bryant SJ, Cuy JL, Hauch KD, Ratner BD. Photo-patterning of porous hydrogels for tissue engineering. Biomaterials 2007;28: 2978-86.

28. Outerbridge RE. The etiology of chondromalacia patellae. J Bone Joint Surg Br 1961;43-B: 752-7.

29. Jungius KP, Schmid MR, Zanetti M, Hodler J, Koch P, Pfirrmann CW. Cartilaginous defects of the femorotibial joint: accuracy of coronal short inversion time inversion-recovery MR sequence. Radiology 2006;240: 482-8.

CHAPTER 7:

CONCLUSIONS

7.1 Summary of Findings

The overall objective of this dissertation was to contribute to the understanding biological and structural changes that occur in the osteochondral interface with age-related degeneration and disease, and the role of these alterations in disease pathogenesis.

To accomplish this, novel image processing and automated analysis methods were used along with high resolution qualitative assessment to acquire a multiscale view of the osteochondral unit. In summary, these methodologies were:

(A)   Development of image processing routines to deconstruct 3-D microCT ScP data into standard subunits, and assess the ScP for morphometric microstructural properties (Chapter 2-3).

(B)   Image stitching of standard SafO-FG histology images to compute the linear density of vascular channel activity and tidemark disruption at the macroscale (Chapter 4).

(C)   Development of standardized, automated methods of reducing 3-D Digital Volumetric Imaging data of the ScP into set cross-sections and movies, to qualitatively assess the morphology of ScP components (Chapter 5).

(D)   Development of novel bioimage informatics analysis of the cell and matrix organization of the articular cartilage, with tracking and information storage of all individual cells, and assessment based on this to determine clustering and local hypocellularity (Chapter 6).

The major findings related to the scientific objectives were:

1. The ScP of degenerated human osteochondral tissue, with surface deterioration and partial thickness erosion of the articular cartilage, has characteristic morphological alterations (Chapter 2).

    a. With surface deterioration of the overlying cartilage but not erosion, tidemark roughness was greater than normal, +66% by one metric.

    b. Surface deterioration is accompanied by cartilage erosion, ScP thickness was higher than normal, by 64%.

    c. When surface deterioration is accompanied by cartilage erosion, ScP porosity slightly decreases (-33%), although the pores that are present are larger (+22%).

2. This structural alteration of the ScP also extends to regions that are less displaced from a full thickness cartilage lesion in tissue areas with a continuum of damage from cartilage covered to eroded. The alteration is spatially related to compromise in the biochemistry of the articular cartilage and potentially to the ability of the osteochondral unit to maintain low hydraulic conductivity. (Chapter 3).

    a. With greater displacement from the full thickness lesion, either in regions farther away from the lesion in the same compartment or in a different

compartment from the lesion, there is greater tidemark roughness and disruption, suggesting this is an early stage alteration.

b. With less displacement, there is greater ScP thickness, suggesting this is a late stage alteration.

c. There is a small decrease in overall porosity only at the transitional region of cartilage where the sampled area is within 4.0 mm of the full thickness lesion.

d. The fixed charge density is substantially lower in the transitional region of cartilage than in more displaced cartilage from the lesion, both assessed by full thickness and deep zone only. This deteriorated cartilage composition may mediate the load-induced signals that cause the subchondral plate to undergo remodeling.

3. The linear density of vascular channels and tidemark disruptions is dependent on the grade of the overlying cartilage. (Chapter 4).

a. The number of inactive channels is lower in more deteriorated samples, although this may be related to deterioration of the structure of the ScP in general. The number of active vascular channels, however, is consistent between normal and deteriorated samples.

b. There are more tidemarks and tidemark disruptions, including those caused by penetrating vascular channels, in early grade deterioration, or samples with a fibrillated cartilage surface, and to a lesser extent in samples with partial thickness erosion. This is not seen in severely eroded samples, suggesting the tidemark irregularities and disruptions to its role as a barrier happen in early stages of degeneration.

4. The 3-D morphology of vascular channels in partially eroded tissue is altered in a way that points to more active remodeling in the ScP (Chapter 5).

   a. In the ScP of cartilage that has partially eroded, more of the vascular channels are larger, contain more cells, have an open or missing bony cap, and penetrate past the tidemark, compared to normal ScP.

   b. The morphology and location of the channels suggest not only that are part of the active remodeling bone resorption pits or BMUs, but they are in close enough proximity to the other layers, the calcified and uncalcified cartilage, that their activity can affect the biology through permeation of solutes.

5. Bioimage informatics of the 3-D organization of the cartilage cells and matrix provide novel structural information or quantification of classically observed histological features of degeneration.

   a. Cell clusters are larger in degenerated cartilage, with the largest clustering adjacent to a full thickness lesion (+240% average cell cluster size compared to normal).

   b. The zonal organization of orientation of cells is lost in increasingly degenerated cartilage, evidenced by the mean cartilage angle in the superficial zone transitioning from horizontally oriented (19.3°) to more isotropic (33.4°) in the most degenerated cartilage.

   c. This increase in clustering, and loss of organization, leads to regions of local hypocellularity in the matrix, with the volume of matrix that is within 15 μm of the nearest nuclei decreasing by as much as 63.5% in degenerated compared to normal.

   d. The greatest cartilage matrix and cell alterations are in the late grades of osteoarthritis (partial thickness erosion adjacent to a full thickness lesion), or

after the tidemark disruption and vascular channel penetration alterations seen in the subchondral bone.

7.2   Discussion

The multiscale analysis of the structural deterioration of the articular cartilage and subchondral plates allows quantification of both the physical changes to the structure of each tissue layer, and the microscale biological components that mediate these changes. The standard imaging techniques used here (histology) are limited in respect to volume sampling, while the high resolution 3-D techniques are limited in their ability to provide biological contrast (microCT) or in field of view (DVI). However, when used together in a complementary way, they link together the microstructural elements of the cells and vasculature and the morphometric properties of the whole tissue layer, in the biological view of the osteochondral interface.

The alterations of the ScP can be divided into two stages: one where the ScP has a rough, disrupted tidemark and active vascular channels protruding into the cartilage, and the second with sclerosis and thickening of the subchondral bone and diminished porosity. In the first stage, the tidemark is rougher, but the thickness and porosity are relatively consistent with normal. Standard histology and DVI analysis revealed that the increased roughness measures in the tidemark were largely due to protruding vascular channels, as well as other features which interfered with the calcification front. The second stage is more in line with the classical changes in bone described with osteoarthritis, in that the bone becomes thickened, and is largely quiescent after the cartilage has fully eroded.

The first stage of ScP alteration has the greatest potential to affect its permeability and hydraulic conductivity, and thus its proper function as a barrier that limits communication between cartilage and the remodeling subchondral bone. Vascular channels that cross the tidemark may be communication pathways for cytokines or other solutes into the uncalcified cartilage. At the same time, because these channels

are actively remodeling, with angiogenic factors promoting further vascular growth and invasion, as well as abnormally high concentrations of osteoclasts and osteoblasts and their associated factors as part of the basic multicellular units, cytokines which are not typically found in normal tissue may be introduced. The hydraulic conductivity increase of the subchondral plate has also been previously shown [1] and potentially goes through these channels and other structural pores in the plate, and affects the ability of the overlying cartilage to maintain fluid pressurization and balance with the exterior synovial fluid.

Along with these ScP changes, the articular cartilage is altered due to reorganization of cells that creates local hypocellularity in the matrix and limited ability to remodel in response to further matrix damage. Some of these changes have been described to a degree, qualitatively, in standard 2-D histological sections, but the DVI method along with 3-D bioimage informatics allows definitive quantification. As the matrix cannot remodel as effectively due to the lack of cells in specific localized regions, these areas may be susceptible to further degradation. Clustering was found to coincide spatially near some fissures, potentially indicating that the rapid proliferation of cells, originally in 2-3 cell chondrons, into 20+ cell aggregates, may be a response to counter matrix breakdown. Because these clusters only cover relatively small regions of the cartilage, this leads to worsening of the local hypocellularity as the chondrocytes are reorganized throughout the tissue into large aggregates interspersed by large regions with few cells. This occurs along with loss of the assigned zonal organization into the superficial, middle and deep zones due to the clustering, which diminishes the specialized biomechanical properties of the cartilage, such as better ability to stand tensile stresses in the superficial zone and compressive stresses in the deep zone. All together, the mechanical abilities and remodeling capability of cartilage is diminished, leading to erosion.

Although deep zone cell and matrix organization alterations were shown to be less severe, it could still be an important region to investigate to link the altered ScP barrier with compromised biochemical content of the articular cartilage. One view of the progression of age-related degeneration and osteoarthritis can be considered a "two-front" battle with wear and loading on the surface leading to altered biochemistry and erosion of the superficial zone, while the altered subchondral plate permeability alters the biochemistry of the deep zone. Whether this should lead to the same or less chondrocyte reorganization in the deep zone is not clear, as the sequence of how the chondrocyte changes lead to matrix deterioration and vice versa here may be different. The deep zone nonetheless may be the important link between the subchondral plate changes and erosion of the cartilage in view of osteoarthritis as a whole joint disease.

In the time sequence of age-related degeneration of osteoarthritis, it appears the first stage of ScP alteration, with compromised barrier function, occurs before substantial changes in the cartilage cell and matrix organization. In Chapters 2 and 3, the tidemark roughening and disruption primarily occurred in Grade 2 regions, where cartilage is fibrillated but there is not yet partial thickness erosion, while in Chapter 4, the tidemark was found to have the most disruptions and invading vascular channels again in Grade 2. In contrast, Grade 3 had less tidemark disruption, and Grade 4 was relatively quiescent in activity and penetration. In Chapter 6, the largest articular cartilage chondrocyte organization changes, matrix local hypocellularity, and matrix fissuring, was found in the most severe grades, Grade 3 and 3+, where there is at least partial thickness erosion, and in the latter where it is adjacent to an area of full thickness erosion. If the bone alterations come first, and these alterations are found at least to a degree to cause the cartilage cell and matrix changes, it would be a significant for addressing OA, shifting the focus for slowing the breakdown of cartilage on the bone rather than treating the cartilage itself.

The findings of the dissertation reinforce the theory that cartilage and subchondral plate deterioration are linked in a feedback loop rather than a one way causal relationship, with the increase in permeability compromising the biochemistry of the cartilage, and the deteriorated cartilage leading to more load and remodeling of the bone. In this model, which has been suggested by Burr and others, there is first either high or repeated joint loading as the individual ages and the joint enters more use. This leads to early deterioration of the cartilage, which leads to translation of more forces onto the subchondral bone. The bone remodels in response to this increased load, and as demonstrated, leads to vascular invasion and more channels for cartilage-bone crosstalk which increases the permeability. The increased permeability and introduction of cytokines not normally present at the osteochondral interface leads to altered biochemistry of the cartilage, possibly through increased production of MMPs as a response. This leads to more breakdown of the cartilage, which leads to more remodeling of the bone, and so forth until the cartilage is completely eroded.

The technical developments that were shown in this dissertation allow the rapid, automated, and unbiased interpretation of 3-D data, along with reduction of the data into a set of metrics. This is useful not only because of the large size of typical high-resolution 3-D data in memory space which makes it difficult to process and assess, but because the principles can help bring standardization to the data presentation and analysis, which is currently lacking in the emerging field of 3-D medical image analysis. The 3-D bioimage informatics metrics used in Chapters 2, 3 and 5 can also be applicable to other tissues in the body, and used to assess the organization and morphology of tissues and cells in development, maturity, aging and disease.

The scientific findings regarding the osteochondral interface have significant implications for identification of pre-osteoarthritis and diagnosis of osteoarthritis, and for future treatment strategies that address the remodeling of the subchondral bone.

Currently, there are few predictors of the eventual development of osteoarthritis other than age and obesity. Once OA has been shown to be a bone disease, diagnosis strategies and identification of pre-OA through the subchondral plate can facilitate finding joints which may be predisposed to cartilage breakdown before the joint space narrowing is detectable. Regarding treatment, there have previously been experimental studies that demonstrate the usefulness of bone resorption inhibitors on inhibiting cartilage breakdown in rats [2], but so far this has had poor translatability to human clinical studies [3-5]. A full understanding of how the bone remodeling and permeability changes play in to the time sequence of OA, may lead to more directed strategies in the specific time when a bone resorption inhibitor regimen should be introduced during treatment, or potentially indicate the use of other pharmaceutical agents which affect other parts of the bone remodeling turnover cycle.
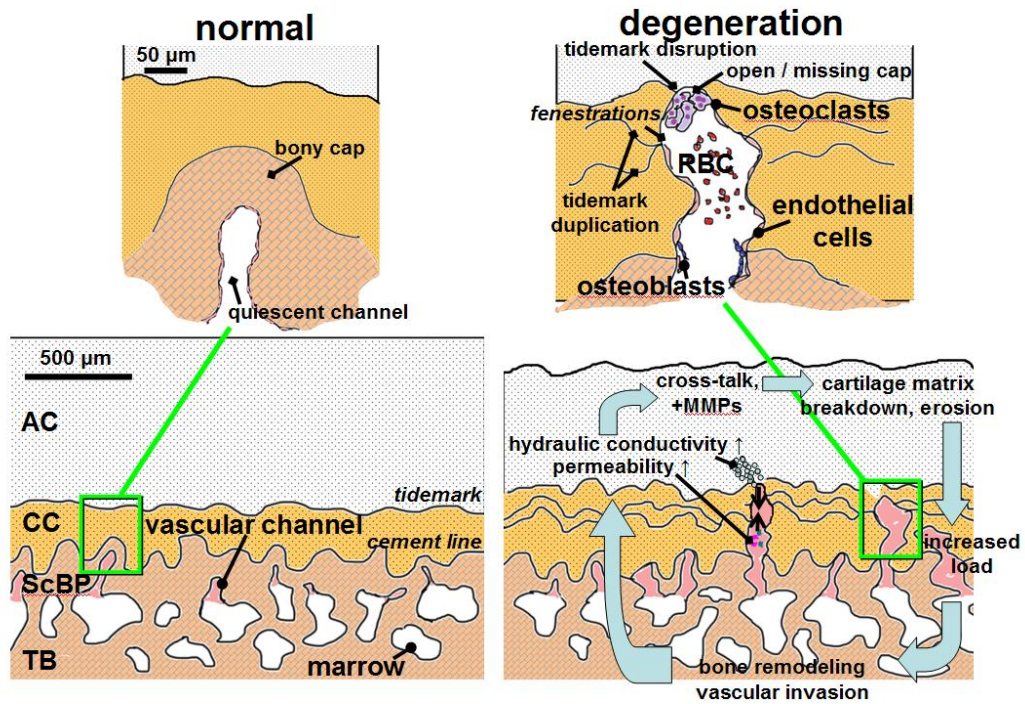
Figure 7.1: Schematic of Subchondral Plate, Vascular Channels and Remodeling, and Effect on Progression of Degeneration.

7.3   Future Work

The findings of this dissertation contribute to the understanding of the role of bone remodeling and increased osteochondral interface permeability in osteoarthritis pathogenesis, and gives insight to how cartilage and bone alterations can be linked in the progression of the disease. This knowledge can be refined and expanded upon in further studies to gain a more accurate picture of how age-related degeneration can transition to osteoarthritis, and develop more accurate predictors for susceptibility to the disease. The 3-D imaging and bioimage informatics assessment techniques can be applied to other biological components which were not covered quantitatively in this study, such as osteocytes, osteoclasts, microcracks, and calcified cartilage chondrocytes, to gain a fuller understanding of the role each feature plays. Additionally, the link between subchondral plate altered structure, to altered subchondral plate permeability, to deterioration of the articular cartilage could be investigated in more detail.

7.3.1. Effect of Subchondral Plate Permeability on Biochemical Composition of Articular Cartilage

As prior studies have demonstrated, cytokines and signaling factors present during remodeling of the subchondral plate can have an effect of homeostasis of the articular cartilage biochemistry. Particularly, some angiogenic factors can promote the production of catabolic matrix metalloproteinases by chondrocytes. The angiogenic factors present during vascular invasion, coupled with the increased communication between channels and cartilage as more of them penetrate past the tidemark, may combine to exacerbate the catabolism of the proteoglycan content of the matrix. This

diminished proteoglycan content was shown in the cartilage using fixed charge density assessment with microCT (Chapter 3), and was especially evident when the deep zone was considered alone. In histology, there are many examples where the protruding vascular channels are adjacent to proteoglycan depletion in the surrounding cartilage matrix (Chapter 4). A full observational study describing such examples and experimental also studies which test the biochemistry of in vivo cartilage when exposed to the neighboring penetrating vascular channels, would be beneficial to the understanding of how big a role subchondral plate remodeling plays in pathogenesis.

7.3.2. Biomechanical Testing of Structurally Compromised Subchondral Plate and Osteochondral Unit

Although the biomechanical barrier function was not directly tested in this dissertation to confirm the potential mechanical effects in higher grade ScP, the studies here have identified the grades of degeneration and characteristic features more likely to have increased plate permeability. For the grade of degeneration, it was shown that Grade 2, or mildly fibrillated cartilage, samples had the most tidemark disruptions and channels crossing the tidemark (Chapter 4). Regarding the characteristic features, the deteriorated samples which present vascular channels with the abnormal morphology of large size, open or missing bony cap, high superficial penetration depth, and high cell activity, are viable targets (Chapter 5). The hydraulic conductivity and permeability can be tested using the entire osteochondral unit as has been previously done [1], or in a novel study involving the isolated ScP alone. For the latter, preparation must be done to both remove the uncalcified cartilage, such as with papain digestion, as well as remove the trabecular bone, possibly with the guide of ScP end boundary delineation techniques that were demonstrated in this dissertation (Chapter 2).

7.4 References

1. Hwang J, Bae WC, Shieu W, Lewis CW, Bugbee WD, Sah RL. Increased hydraulic conductance of human articular cartilage and subchondral bone plate with progression of osteoarthritis. Arthritis Rheum 2008;58: 3831-42.

2. Hayami T, Pickarski M, Wesolowski GA, McLane J, Bone A, Destefano J, Rodan GA, Duong le T. The role of subchondral bone remodeling in osteoarthritis: reduction of cartilage degeneration and prevention of osteophyte formation by alendronate in the rat anterior cruciate ligament transection model. Arthritis Rheum 2004;50: 1193-206.

3. Nishii T, Tamura S, Shiomi T, Yoshikawa H, Sugano N. Alendronate treatment for hip osteoarthritis: prospective randomized 2-year trial. Clinical rheumatology 2013;32: 1759-66.

4. Saag KG. Bisphosphonates for osteoarthritis prevention: "Holy Grail" or not? Annals of the rheumatic diseases 2008;67: 1358-9.

5. Davis AJ, Smith TO, Hing CB, Sofat N. Are bisphosphonates effective in the treatment of osteoarthritis pain? A meta-analysis and systematic review. PLoS One 2013;8: e72714.